



ECOLE DOCTORALE SCIENCES ET INGÉNIERIE
DE L'UNIVERSITÉ DE CERGY-PONTOISE

MATHEMATISCHEN -
NATURWISSENSCHAFTLICHEN FAKULTÄT DER
UNIVERSITÄT DES SAARLANDES

THESIS

defenced to obtain doctor's degree at
"Université en Sciences et Technologies de
l'Information et de la Communication"

DISSERTATION

zur Erlangung des akademischen Grades
des Doktors der Naturwissenschaften

STUDY OF GENERALIZED RADON TRANSFORMS AND APPLICATIONS IN COMPTON SCATTERING TOMOGRAPHY

by

GAËL RIGAUD

Laboratoire Equipes Traitement de l'Information
et Systèmes (ETIS) - UMR 8051
F-95014 Cergy-Pontoise, France

Institut für Angewandte Mathematik,
Universität des Saarlandes
D-66041 Saarbrücken, Deutschland

Before the committee consisted of

Pr. Jalal Fadili	ENSICAEN & IUF	President
Pr. Habib Ammari	Ecole Normale Supérieure	Reviewer
Pr. Pierre Maréchal	Université Paul Sabatier	Reviewer
Pr. Christian Jutten	Université Joseph Fourier	Examiner
Pr. Maï K. Nguyen-Verger	Université de Cergy-Pontoise	Thesis director
Pr. Alfred K. Louis	Universität des Saarlandes	Thesis director

Tag des Kolloquiums:	20 November 2013
Ort des Kolloquiums:	ENSEA 6, avenue du Ponceau, Cergy-Pontoise, France
Präsident der Univ. Cergy-Pontoise:	Univ.-Prof. Dr. F. Germinet
Dekan der Univ. des Saarlandes - NTF I:	Univ.-Prof. Dr. M. Groves
Vorsitzender:	Univ.-Prof. Dr. J. Fadili
Berichterstatter:	Univ.-Prof. Dr. H. Ammari Univ.-Prof. Dr. P. Maréchal
Prüfer:	Univ.-Prof. Dr. Dr. h.c. A.K. Louis Univ.-Prof. Dr. M.K. Nguyen-Verger Univ.-Prof. Dr. C. Jutten

Je souhaite remercier tout d'abord le Professeur Nguyen qui m'a permis de connaître le monde de la Recherche et sans qui, aujourd'hui, je ne serai pas docteur. Je ne remercierai jamais assez le Professeur Louis qui m'a offert son soutien et sa confiance ainsi qu'une fabuleuse place dans son équipe à Sarrebruck. Je tiens également à exprimer toute ma gratitude aux membres du jury avec qui j'espère pouvoir continuer à l'avenir ses discussions stimulantes.

J'ai passé 3 années enrichissantes auprès de gens formidables à Cergy-Pontoise puis à Sarrebruck que je n'oublierai jamais. Je tiens tout particulièrement à remercier Rémi et Aref pour leur amitié ainsi que pour les collaborations que nous avons partagées.

Enfin j'embrasse de tout mon cœur ma famille et mes proches qui m'ont témoigné un soutien indéfectible tout au long de cette étape de ma vie.

A Cergy-Pontoise, le 20 novembre 2013,

Gaël Rigaud

*À feu mon grand-père, René Rigaud,
un homme courageux et érudit.*

*"Imagination is more important than knowledge."
Albert Einstein*

Short Abstract

This thesis is concerned with the study of new modalities of Compton scattering tomography which are a relevant alternative with current imaging techniques. Such a study requires powerful mathematical tools. Then I, first, extended the known properties of the classical Radon transform to larger manifolds of curves. In particular, I established the analytical inversion formulas for solving the associated image reconstruction problem. Due to these inversion properties and a numerical study of involved processes, the theoretical feasibility of the proposed modalities in Compton scattering tomography could be established. In a second time, I established an iterative algorithm to correct the attenuation factor in the studied modalities (GIPC). Finally, I proposed the first bimodality based on the scattered radiation. This new system, akin to the SPECT-CT scan, combines two modalities of Compton scattering tomography. The simulation results show the interest of such a future system.

Kurze Zusammenfassung

Diese Arbeit konzentriert sich auf die Untersuchung neuer Modelle in der Compton - Streutomographie, die eine relevante Alternative oder Ergänzung aktueller bildgebender Verfahren darstellen. Da eine mathematische Untersuchung dafür benötigt ist, habe ich zuerst die Eigenschaften der Radontransformation auf eine größere Familie von Kurven erweitert. Insbesondere habe ich die analytischen Umkehrformeln zur Bildrekonstruktion etabliert. Dank dieser Inversionsigenschaften und der numerischen Untersuchung der beteiligten Prozessen, hat die theoretische Machbarkeit der Compton-Streutomographie Modelle bewiesen. Dann habe ich einen iterativen Algorithmus (GIPC) hergeleitet, um den Dämpfungsfaktor in den Modalitäten zu korrigieren. Schließlich habe ich die erste Bimodalität auf der Grundlage der Streustrahlung aufgestellt. Dieses neue System kombiniert zwei Methoden der Compton-Streutomographie ähnlich des SPECT-CT Bilder. Die Simulationsergebnisse zeigen dass in Zukunft großes Interesse an einen solchen System existiert.

Depuis l'avènement des premiers appareils imageurs par rayonnement ionisant initié par les prix Nobel Godfrey Newbold Hounsfield et Allan MacLeod Cormack en 1979, le besoin en de nouvelles techniques d'imagerie non invasives n'a cessé de croître. Ces techniques s'appuient sur les propriétés de pénétration dans la matière des rayonnements X et gamma pour détecter une structure cachée sans avoir à détruire le milieu exposé. Elles sont employées dans de nombreux domaines allant de l'imagerie médicale au contrôle non destructif en passant par le contrôle environnemental.

Cependant les techniques utilisées jusqu'à maintenant subissent de fortes dégradations dans la qualité des mesures et des images reconstruites. Généralement approchées par un bruit, ces dégradations exigent d'être compensées ou corrigées par des dispositifs de collimation et de filtrage souvent coûteux. Ces dégradations sont principalement dues aux phénomènes de diffusion qui peuvent constituer jusqu'à 80 % du rayonnement émis en imagerie biomédicale. Dès les années 80 un nouveau concept a vu le jour pour contourner cette difficulté : la tomographie Compton. Cette nouvelle approche propose de mesurer le rayonnement dit diffusé en se plaçant dans des gammes d'énergie (140 – 511 keV) où l'effet Compton est le phénomène de diffusion prépondérant.

L'exploitation de tels dispositifs d'imagerie nécessite une compréhension profonde des interactions rayonnement/matière afin de proposer un modèle, cohérent avec les données mesurées, indispensable à la reconstruction d'images. Dans les systèmes d'imagerie conventionnels (qui mesurent le rayonnement primaire), la transformée de Radon définie sur les lignes droites est apparue comme le modèle naturel. Mais en tomographie Compton, l'information mesurée est liée à l'énergie de diffusion et ainsi à l'angle de diffusion. Ainsi la géométrie circulaire induite par le phénomène de diffusion rend la transformée de Radon classique inadaptée. Dans ce contexte, il devient nécessaire de proposer des transformées de type Radon sur des variétés géométriques plus larges.

L'étude de la transformée de Radon sur de nouvelles diversités de courbes devient alors nécessaire pour répondre aux besoins d'outils analytiques de nouvelles techniques d'imagerie. Cormack, lui-même, fut le premier à étendre les propriétés de la transformée de Radon classique à une famille de courbes du plan. Par la suite plusieurs travaux ont été menés dans le but d'étudier la transformée de Radon définie sur différentes variétés de cercles, des sphères, des lignes brisées pour ne citer qu'eux. En 1994 S.J. Norton proposa la première modalité de tomographie Compton modélisable par une transformée de Radon sur les arcs de cercle, la $CART_1$. En 2010 Nguyen et Truong établirent l'inversion de la transformée de Radon sur les arcs de cercle, $CART_2$, permettant de modéliser la formation d'image dans une nouvelle modalité de tomographie Compton. La géométrie des supports d'intégration impliqués dans de nouvelles modalités de tomographie Compton les conduisent à démontrer l'invertibilité de la transformée de Radon définie sur une famille de courbes de type Cormack, appelée C_α . Ils illustrèrent la procédure d'inversion dans le cadre d'une nouvelle transformée, la $CART_3$ modélisant une nouvelle modalité de tomographie Compton. En nous basant sur les travaux de Cormack et de Truong et Nguyen, nous proposons d'établir plusieurs propriétés de la transformée de Radon définie sur la famille C_α et plus particulièrement sur C_1 . Nous avons ainsi démontré deux formules d'inversion qui reconstruisent l'image d'origine via sa décomposition harmonique circulaire et celle de sa transformée et qui s'apparentent à celles établies par Truong and Nguyen. Nous avons enfin établi la bien connue rétroprojection filtrée ainsi que la décomposition en valeurs singulières dans le cas $\alpha = 1$. L'ensemble des résultats établis dans le cadre de cette étude apporte des réponses concrètes aux problèmes de reconstruction d'image associés à ces nouvelles transformées.

En particulier nous avons pu établir de nouvelles méthodes d'inversion pour les transformées $CART_{1,2,3}$ et ainsi que les approches numériques nécessaires pour l'implémentation de ces transformées. Tous ces résultats ont ainsi permis de résoudre les problèmes de formation et de reconstruction d'image liés à trois modalités de tomographie Compton.

En outre nous proposons d'améliorer les modèles et algorithmes proposés afin de tenir compte des phénomènes d'atténuation. En effet le rayonnement diffusé est soumis au phénomène d'atténuation induit par la traversée du flux de photons dans la matière. La prise en compte d'un tel facteur dans nos modèles rend alors nos méthodes d'inversion inadaptées. Dès lors nous avons proposé une méthode de correction itérative généralisée adaptée à l'imagerie utilisant nos méthodes d'inversion pour corriger le facteur d'atténuation. Cette méthode constitue une généralisation de l'algorithme IPC (Iterative Pre-Correction) qui fut proposé en 1992 par Mazé.

Nous avons ensuite associé deux modalités de tomographie Compton avec des architectures compatibles : une des modalités étudiées fonctionnant par transmission à une modalité, établie par Nguyen et Truong, fonctionnant, elle, par émission. Cette combinaison constitue le tout premier système d'imagerie bimodal utilisant le rayonnement diffusé comme agent imageur et permet l'obtention de la densité d'électrons et de l'activité proposant ainsi une alternative innovante et pertinente au SPECT-CT scan classique.

Zusammenfassung

Seit dem Aufkommen der ersten Geräte für bildgebende Verfahren mit ionisierender Strahlung initiiert von Godfrey Newbold Hounsfield und Allan MacLeod Cormack, sind die Anforderungen an neue nicht-invasive bildgebende Verfahren gewachsen. Diese Methoden basieren auf den Penetrationseigenschaften von Röntgen und Gammastrahlung zum Erfassen einer verborgenen Struktur ohne Zerstörung der beleuchteten Umgebung. Sie werden in vielen Bereichen eingesetzt, angefangen von der medizinischen Bildgebung bis hin zum zerstörungsfreien Prüfen.

Allerdings leiden die bisher verwendeten Techniken unter der schlechten Qualität der Daten und der rekonstruierten Bilder. Diese muss mit Kollimatoren und meist teuren Filtern kompensiert oder korrigiert werden. Sie ist insbesondere auf Streuphänomene zurückzuführen, die bis zu 80 % der emittierten Strahlung in biologischem Gewebe ausmachen können. In den 80er Jahren entstand ein neues Konzept, um diese Schwierigkeit umzugehen: die Compton-Streutomographie (CST). Dieser neue Ansatz schlägt vor, die Streustrahlung unter Berücksichtigung der Energiebereiche (140 bis 511 keV zu messen), wobei der Compton-Effekt dominiert.

Die Verwendung entsprechender bildgebender Geräte erfordert ein tiefes Verständnis von den Wechselwirkungen zwischen Strahlung und Materie, um eine für die Bildrekonstruktion notwendige Modellierung zu wählen, welche mit den Messdaten konsistent ist. Bei herkömmlichen bildgebenden Systemen, welche die Primärstrahlung messen erwies sich, die klassische Radon-Transformation als natürliche Modellierung. In der Compton-Streutomographie hingegen hängt die gemessene Information von der Streuenergie und damit vom Streuwinkel ab. Aufgrund dieser Kreisgeometrie ist die klassische Radon Transformation in diesem Fall unzureichend, da diese nur über Geraden integriert. In diesem Zusammenhang ist es notwendig, die Radon Transformationen auf weiteren geometrischen Mannigfaltigkeiten zu betrachten.

Die Untersuchung der Radon-Transformation auf neue Kurvenmannigfaltigkeiten ist notwendig, um die theoretischen Grundlagen für neue Bildgebungsverfahren bereitzustellen. Cormack war der Erste, der die Eigenschaften der herkömmlichen Radon Transformation auf eine Familie von Kurven in der Ebene erweiterte. Danach haben mehrere Studien, die Radon Transformation für verschiedene Varianten von Kreisen, Kugeln, gebrochenen Strahlen, etc. untersucht. Im Jahr 1994 schlug S. J. Norton das erste Modell in der Compton-Streutomographie vor basierend auf einer Radon Transformation auf Kreisbögen, die $CART_1$ hier. Im Jahr 2010 leiteten Nguyen und Truong die Inversionsformal einer Radon-Transformation auf Kreisbögen her, $CART_2$, um die Datengewinnung mit einem neuen Modell der Compton-Streuung Tomographie zu modellieren. Die zugrunde liegende Geometrie führte sie auf die Inversion der Radon Transformation für eine Familie von Cormack-Typ- Kurven, genannt C_α . Sie veranschaulicht die Inversion an einer neuen Transformation, $CART_3$, welche eine weitere Modellierung der Compton-Streutomographie darstellt. Basierend auf der Arbeit von Cormack sowie Truong und Nguyen leiten wir Eigenschaften der Radon Transformation auf der Kurvenfamilie C_α , insbesondere C_1 , Damit haben wir zwei Inversionformeln, die das ursprüngliche Bild mit Hilfe der Kreis harmonischen Zerlegung rekonstruieren. Diese Formeln ähneln denen von Nguyen und Truong. Abschliessend leiten wir die bekannte gefilterten Rückprojektion und die Singulärwertzerlegung im Fall $\alpha = 1$ her. Alle Ergebnisse in dieser Arbeit führen auf praktische Probleme der Bildrekonstruktion bei den genannten Modellen.

Insbesondere konnten wir neue Inversionsverfahren für die Transformationen $CART_{1,2,3}$ sowie numerische Ansätze für die Implementierung dieser Transformationen herleiten. Diese Ergebnisse ermöglichen die Datengewinnung und die Rekonstruktion bei den drei Modellen der Compton-Streutomographie.

Darüber hinaus schlagen wir vor, bestehende Modelle und Algorithmen zu verbessern, um das Phänomen der Abschwächung zu berücksichtigen. Aufgrund des Durchdringens des Photonenflusses in der Materie unterliegt die gestreute Strahlung dem Phänomen der Dämpfung. Durch die Berücksichtigung eines solchen Faktors in unserem Modell wird unser Inversionsverfahren unzureichend. Daher schlagen wir ein verallgemeinertes iteratives Korrekturverfahren vor, um in unserem Inversionsverfahren den Dämpfungsfaktor zu korrigieren. Dieses Verfahren ist eine Verallgemeinerung des IPC-Algorithmus (Iterative Pre-Correction), der 1992 von Maze vorgeschlagen wurde.

Anschliessen haben wir zwei Modalitäten der Compton-Streutomographie mit kompatiblen Strukturen Architekturen kombiniert: eine basierend auf Transmission, die andere auf Emission, welche von Nguyen und Truong untersucht wurde. Diese Kombination ist das erste bimodale Bildgebungssystem mittels Streustrahlung als Bildgebungsmittel und ermöglicht es, die Elektronendichte und Aktivität zu erhalten somit bietet es eine innovative und effektive Alternative zum konventionellen SPECT-CT-Scan.

Abstract

Since the advent of the first ionizing radiation imaging devices initiated by Godfrey Newbold Hounsfield and Allan MacLeod Cormack, Nobel Prizes in 1979, the requirement for new non-invasive imaging techniques has grown. These techniques rely upon the properties of penetration in the matter of X and gamma radiation for detecting a hidden structure without destroying the illuminated environment. They are used in many fields ranging from medical imaging to non-destructive testing through.

However, the techniques used so far suffer severe degradation in the quality of measurement and reconstructed images. Usually approximated by a noise, these degradations require to be compensated or corrected by collimating devices and often expensive filtering. These degradation is mainly due to scattering phenomena which may constitute up to 80% of the emitted radiation in biological tissue. In the 80's a new concept has emerged to circumvent this difficulty : the Compton scattering tomography (CST). This new approach proposes to measure the scattered radiation considering energy ranges (140-511 keV) where the Compton effect is the phenomenon of leading broadcast.

The use of such imaging devices requires a deep understanding of the interactions between radiation and matter to propose a modeling, consistent with the measured data, which is essential to image reconstruction. In conventional imaging systems (which measure the primary radiation) the Radon transform defined on the straight lines emerged as the natural modeling. But in Compton scattering tomography, the measured information is related to the scattering energy and thus the scattering angle. Thus the circular geometry induced by scattering phenomenon makes the classical Radon transform inadequate. In this context, it becomes necessary to provide such Radon transforms on broader geometric manifolds.

The study of the Radon transform on new manifolds of curves becomes necessary to provide theoretical needs for new imaging techniques. Cormack, himself, was the first to extend the properties of the conventional Radon transform of a family of curves of the plane. Thereafter several studies have been done in order to study the Radon transform defined on different varieties of circles, spheres, broken lines In 1994 S.J. Norton proposed the first modality in Compton scattering tomography modeled by a Radon transform on circular arcs, the $CART_1$ here. In 2010, Nguyen and Truong established the inversion formula of a Radon transform on circular arcs, $CART_2$, to model the image formation in a new modality in Compton scattering tomography. The geometry involved in the integration support of new modalities in Compton scattering tomography lead them to demonstrate the invertibility of the Radon transform defined on a family of Cormack-type curves, called C_α . They illustrated the inversion procedure in the case of a new transform, the $CART_3$, modeling a new modeling of Compton scattering tomography. Based on the work of Cormack and Truong and Nguyen, we propose to establish several properties of the Radon transform on the family C_α especially on C_1 . We have thus demonstrated two inversion formulae that reconstruct the original image via its circular harmonic decomposition and its corresponding transform. These formulae are similar to those established by Truong and Nguyen. We finally established the well-known filtered back projection and singular value decomposition in the case $\alpha = 1$. All results established in this study provide practical solutions to problems of image reconstruction associated with these new transforms.

In particular we were able to establish new inversion methods for transforms $CART_{1,2,3}$ as well as numerical approaches necessary for the implementation of these transforms. All these results enable to solve problems of image formation and reconstruction related to three Compton scattering tomography modalities.

In addition we propose to improve models and algorithms established to take into account the attenuation phenomena. Indeed, the scattered radiation is subject to the phenomenon of attenuation induced by the penetration and crossing of the photon flux in the matter. The consideration of such a factor in our model then makes our inversion methods inadequate. Therefore we proposed a generalized iterative correction method suitable for imaging systems using our inversion methods to correct the attenuation factor. This method is a generalization of the IPC algorithm (Iterative Pre-Correction) that was proposed in 1992 by Maze.

We then combined two modalities of Compton scattering tomography with compatible architectures : one working by transmission and the other one working by emission and studied by Nguyen and Truong. This combination is the first system of bimodal imaging using scattered radiation as imaging agent and enables to obtain the electron density and activity offering therefore an innovative and effective alternative to conventional SPECT-CT scan.

Table of Contents

List of Figures	xvi
Introduction	1
I Radon transform over generalized Cormack curves	9
I.1 Review of Radon transform	10
I.1.1 Standard Radon transform	10
I.1.2 Cormack's class of curves and Radon transform	14
I.1.3 Extension to others kind of curves in the plane	16
I.2 Inverse Radon transform over generalized Cormack curves	20
I.2.1 Definition and forward problem	20
I.2.2 Inversion formulae	21
I.3 SVD and FBP for \mathcal{A} defined over C_1	23
I.4 Some examples of curves	27
I.5 Conclusion	29
II Applications in Compton scattering tomography	31
II.1 Basis of conventional and Compton scattering tomographies	32
II.1.1 Ionising radiation : interactions with matter	32
II.1.2 Conventional tomography	39
II.1.3 Motivations behind Compton scattering tomography (CST)	42
II.2 CST modality based on $CART_1$	46
II.2.1 Working principle	46
II.2.2 Norton's inversion method	47
II.2.3 Definition of the $CART_1$ and of its adjoint	48
II.2.4 Modeling of the image formation process	50
II.2.5 Associated inversion formulae	51
II.3 Novel CST modality based on $CART_2$	56
II.3.1 Working principle	56
II.3.2 Definition of the $CART_2$ and of its adjoint	57
II.3.3 Modeling of image formation process	60
II.3.4 Associated inversion formulae	61
II.4 Novel CST modality based on $CART_3$	63
II.4.1 Working principle	63
II.4.2 Defintion of the $CART_3$ and of its adjoint	63
II.4.3 Suited sampling for $CART_3$	65
II.4.4 Associated inversion formulae	66
II.5 Implementation methods for different equations	68
II.5.1 Image formation	68
II.5.2 Noisy data	69
II.5.3 Image reconstruction	69
II.6 Simulation Results	72
II.7 Conclusion	73

III A new concept of bimodality in Compton scattering tomography	81
III.1 Attenuation correction algorithms	82
III.1.1 Detection of the contours of the attenuating medium	82
III.1.2 Constant attenuation factor correction	82
III.1.3 Attenuation correction with a given heterogeneous attenuation map	83
III.2 Generalized Iterative Pre-Correction algorithm (GIPC)	85
III.2.1 Presentation of the algorithm	85
III.2.2 Application for inverting the attenuated $CART_2$	88
III.3 A novel bimodal system based on scattered radiation	92
III.3.1 A new concept	92
III.3.2 Theory	93
III.3.3 Correction algorithm description	97
III.3.4 Simulation studies	98
III.3.5 Results	99
III.4 Conclusion	103
Conclusion and Perspectives	105
Bibliography	107

List of Figures

1	Image reconstruction in CT scan	2
2	Principle of Compton scattering	2
I.1	Geometric setup of the integration along a straight line	11
I.2	Geometric setup and scanning of the medium for Redding's curve	17
I.3	Geometric setup of integration along the circle $C(\rho, \phi)$	18
I.4	Parameters of the V-line Radon transform with a mirror	19
I.5	Representations of particular $\alpha = 1$ solutions	28
II.1	Electromagnetic spectrum and non-invasive imaging methods	33
II.2	Energy of a photon scattered by Compton effect with respect to the scattering angle with $E_0 = 140$ keV.	34
II.3	Geometry of Compton scattering: the incident photon energy E_0 yields a part of its energy to an electron and is scattered with an angle ω	35
II.4	Photoelectric effect: the incident photon is absorbed by the atom.	35
II.5	Pair production: the incident photon is absorbed by the atom, the positron recombines with an electron in creating two annihilation photons of 511keV and opposite directions.	36
II.6	Attenuation of the incident flux by all cross sections σ surrounding scattering particles in the section S of the flow.	37
II.7	Geometry of the differential cross section	39
II.8	Working principle of X-ray tomography	41
II.9	Wrong detections in CT-scan due to Compton scattering.	43
II.10	Working principle of modalities on Compton scattering tomography	45
II.11	Representation of the Norton's modality	46
II.12	Scanning of the medium in CST_1	47
II.13	Representation of the curve $\mathcal{C}_1(p, \varphi)$	48
II.14	Shape of the PSF for $r_0 = 10$ and $\theta_0 = 0$	50
II.15	Working principle	56
II.16	Scanning of the studied object in CST_2	57
II.17	Representation of the curve $\mathcal{C}_2(\omega, \varphi)$	58
II.18	Shape of the point spread function for $R = 10$, $r_0 = 5$ and $\theta_0 = 0$	59
II.19	Principle of $CART_2$ in cartesian coordinates	60
II.20	Representation of the curve $\mathcal{C}_3(\gamma_0, \varphi)$	63
II.21	Shape of the point spread function for $R = 10$, $r_0 = 5$ and $\theta_0 = 0$	65
II.22	Representation of the ramp filter $ \nu $ with apodization $H(\nu) \cdot \nu $	70
II.23	Simulation Results for $CART_1$ with a gaussian noise of 20 dB	74
II.24	Simulation Results for $CART_1$ with a Poisson noise of 13 dB	75
II.25	Simulation Results for $CART_2$ with a gaussian noise of 20 dB	76
II.26	Simulation Results for $CART_2$ with a Poisson noise of 13 dB	77
II.27	Simulation Results for $CART_3$ with a gaussian noise of 20 dB	78
II.28	Simulation Results for $CART_3$ with a Poisson noise of 13 dB	79
III.1	Algorithm GIPC	87
III.2	Flight of detected photons in the $CART_2$	88

III.3	Normalized mean square error in three cases vs iterations.	90
III.4	Reconstruction of the Zubal phantom from $CART_2$ data	91
III.5	Representation of both modalities on CST for a same slice.	92
III.6	Concept of a novel bimodal system	93
III.7	Principle of Norton's modality of Compton scattering tomography	94
III.8	Principle of compounded \mathcal{V} -line Radon transform and parameters setup	95
III.9	Slice of the Zubal phantom	99
III.10	$CART_1$ (a) and CVRT (b) of the phantom shown in figure III.9. Reconstruction of the electron density (c) and activity distribution (d) using equations (III.35) and eq (III.36), respectively, without noise and correction	100
III.11	$CART_1$ (a) and CVRT (b) of the phantom shown in figure III.9 without attenuation. Reconstruction of the electron density (c) and activity distribution (d) with the analytical inversion formulae.	101
III.12	NMSE (in %) in terms of iterations for the correction of the electron density (a) and of the activity map (b) for different SNR.	101
III.13	Different reconstructions of the electron density map, attenuation map for different SNR. Reconstructions are obtained using the proposed correction algorithm and a Poisson noise process. We start these algorithms with data in Figs. III.10(a) and III.10(b).	102

Acronyms

CART ₁	First studied Circular-arc Radon transform
CART ₂	Second studied Circular-arc Radon transform
CART ₃	Third studied Circular-arc Radon transform
CHD	Circular harmonic domain
CST	Compton scattering tomography
CST ₁	CST modality by transmission based on CART ₁
CST ₂	CST modality by transmission based on CART ₂
CST ₃	CST modality by transmission based on CART ₃
CST _T	CST modality by transmission based on attenuated CART ₁
CST _E	CST modality by emission based on attenuated CVRT
CT	Computed tomography
CVRT	Compounded V-line Radon transform
GCC	Generalized Chang Correction algorithm
GIPC	Generalized Iterative Pre-Correction algorithm
IPC	Iterative Pre-Correction algorithm
FFT	Fast Fourier transform
FBP	Filtered Back-projection
NMSE	Normalized mean-squared error
PET	Positron emission tomography
SNR	Signal-to-noise ratio
SPECT	Single photon emission computed tomography

Notations

Spaces

$\mathbb{R}, \bar{\mathbb{R}}$ and \mathbb{C}	Real, extended real and complex numbers
\mathbb{D}	Unit disk
$\mathcal{L}^p(\Omega)$	Space with norm $\left(\int_{\Omega} f ^p dx\right)^{1/p}$
$\mathcal{L}^p(\Omega, W)$	Same as $\mathcal{L}^p(\Omega)$ but with weight W
S^{n-1}	Unit sphere in \mathbb{R}^n

Operators

\mathcal{R}	Radon transform
\mathcal{R}_a	Attenuated Radon transform
\mathcal{A}	Radon transform on curves C_α
\mathcal{C}^i	Forward CART_i
\mathcal{C}^{i*}	Adjoint operator of CART_i
$\mathcal{C}^{i\Phi}$	Attenuated CART_i
\mathcal{H}	Hilbert transform
\mathcal{I}^α	Riesz potential
\mathcal{F}^1	1D-Fourier transform on the radial parameter
\mathcal{F}^2	2D-Fourier transform
\mathcal{V}	Forward CVRT
\mathcal{V}^Φ	Attenuated CVRT
div	Divergence operator
Re	Real part
$p.v.$	Cauchy principal value
$p.f.$	Pseudo-function

Functions

$\delta(\cdot)$	1D Dirac function
$\text{sgn}(\cdot)$	sign function
E_ω	photon energy of a Compton scattering of angle ω
$n_e(r, \theta)$	object electron density in polar coordinates
$\mu_\omega(x, y)$	object attenuation map in cartesian coordinates at energy E_ω
$a(x, y)$	source activity in cartesian coordinates
$f_l(r)$	circular harmonic components of a function $f(r, \theta)$
$Y(\cdot)$	Heaviside function
$P(\cdot)$	Klein-Nishina probability
$T_l(\cdot)$	Chebyshev polynomial of the first kind
$U_l(\cdot)$	Chebyshev polynomial of the second kind
$R_n^m(\cdot)$	Radial Zernike polynomials

We shall find it convenient to consider arbitrary complex-valued functions f on \mathbb{H} satisfying the square-integrability condition,

$$\|f\|_{\mathbb{H}}^2 = \iint_{\mathbb{H}} |f(r, \theta)|^2 r dr d\theta < \infty, \quad (1)$$

and we adopt the standard notation, $L^2(\mathbb{H})$, for the Hilbert space associated with these functions, with inner product,

$$\langle f_1, f_2 \rangle_{\mathbb{D}} = \iint_{\mathbb{H}} f_1(r, \theta) \overline{f_2(r, \theta)} r dr d\theta, \quad (2)$$

in which the bar denotes complex conjugation. We shall also refer to the Hilbert space, $L^2(\mathbb{H}, W)$, of functions on \mathbb{H} , square-integrable with respect to a specified weight function, $W(p, \varphi)$, which may be any nonnegative real-valued function integrable on \mathbb{H} . The corresponding inner product is given by

$$\langle g_1, g_2 \rangle_{\mathbb{H}, W} = \int_{-1}^1 dp \int_0^{2\pi} d\varphi W(p, \varphi) g_1(p, \varphi) \overline{g_2(p, \varphi)}. \quad (3)$$

We take the same definition than Cormack for Zernike polynomials, that is to say

$$R_n^m(r) = \sum_{s=0}^m \frac{(-1)^s (n+2m-s)!}{s!(n+m-s)!(m-s)!} r^{n+2m-2s}, \quad (4)$$

and we denote by $T_i(q)$ (resp. $U_i(q)$) the Chebyshev polynomial of first (resp. second) kind. We define the circular harmonic components of a function $f : \mathbb{D} \rightarrow \mathbb{C}$ by

$$f_n(r) = \frac{1}{2\pi} \int_0^{2\pi} e^{-in\theta} f(r, \theta) d\theta, \quad \text{with} \quad f(r, \theta) = \sum_{n \in \mathbb{Z}} f_n(r) e^{in\theta}. \quad (5)$$

We define the Hilbert transform of a function $g(t)$ by

$$(\mathcal{H}g)(s) = \frac{1}{\pi} \int_{\mathbb{R}} \frac{g(t)}{s-t} dt. \quad (6)$$

To assess the quality of the reconstructions, we define the Normalized Mean Squared Error (NMSE) as:

$$NMSE = \frac{1}{N^2} \frac{\sum_{(i,j) \in [1,N]^2} |\mathcal{I}_r(i, j) - \mathcal{I}_o(i, j)|^2}{\max_{(i,j) \in [1,N]^2} \{\mathcal{I}_o(i, j)\}^2}$$

where \mathcal{I}_r is the reconstructed image and \mathcal{I}_o the original image and the signal-to-noise ratio (SNR) of a function g with the reference function $\mathcal{T}f$ by

$$SNR = 10 \log \left(\frac{\int_{\mathbf{t} \in \mathcal{T}} \mathcal{T}f(\mathbf{t})^2 d\mathbf{t}}{\int_{\mathbf{t} \in \mathcal{T}} |g(\mathbf{t}) - \mathcal{T}f(\mathbf{t})|^2 d\mathbf{t}} \right).$$

Introduction

Context and Issues

Nowadays imaging techniques using penetrating radiation are essential for medical diagnosis to image a brain tumor or for non destructive testing by detecting a flaw within an industrial piece for example. Using penetrating properties of X or gamma rays, these techniques enable to probe the interior of an object without damaging it. X-rays or gamma rays correspond to high-energy photons (enough to ionize an atom or molecule), which are poorly absorbed and not deflected by the material through which they pass. The first imaging system of this kind was developed by G. Hounsfield in 1972 and is called : X-ray computed tomography scan (CT scan). It produces tomographic images or "slices" of an area of an object thanks to an emitting X-ray source and detectors placed on the other side of the studied object. Its working principle is then the following : the source illuminates the object, primary radiation crosses it over and then is collected by detectors. The interaction between radiation and matter is characterized by the attenuation of the radiation and depends on the energy of the radiation and the nature of the studied material. In the case of primary radiation, the variation of the flux intensity is given by the Beer-Lambert law

$$I = I_0 e^{-\int_{x \in D} \mu(x) dl}$$

where I_0 (resp. I) is the entering (resp. outgoing) flux intensity, $\mu(x)$ is the lineic attenuation map and D is the line path of the flux. Hence measurement in CT-scan is naturally modeled by the well-known Radon transform which represents the integral of a given function over straight lines in the plane, see Fig. 1.

Since the seminal work of Johann Radon in 1917, many extensions of this integral transform have been widely discussed, in particular in the literature of imaging science. This is the case when results of measurements appear under the form of integrals of a physical quantity over lower dimensional manifolds. The relevant problem to solve is the recovery of the physical quantity of interest as a function in \mathbb{R}^2 .

In 1981, A. M. Cormack studied Radon transforms on two remarkable families of curves in the plane defined by parameters (p, φ) as follows :

- α -curves ($\alpha > 0$):

$$r^\alpha \cos(\alpha(\theta - \varphi)) = p^\alpha, \quad \text{with} \quad |\theta - \varphi| \leq \frac{\pi}{2\alpha},$$

- β -curves ($\beta > 0$):

$$p^\beta \cos(\beta(\theta - \varphi)) = r^\beta, \quad \text{with} \quad |\theta - \varphi| \leq \frac{\pi}{2\beta}.$$

Cormack showed several properties of the circular harmonic components of the Radon transforms on these two classes of curves and established inversion formulae in terms of the circular harmonic components of the unknown function as well as the consistency condition for the data.

In the past decades, the inversion of Radon transforms on circles centered on a smooth curve has been established in the context of Synthetic Aperture Radar or in thermo-acoustic tomography. In 1993 Kurusa generalized invertibility for Radon transform on curves having strictly convex distance function in two-point homogeneous spaces of constant curvature but no example was given.

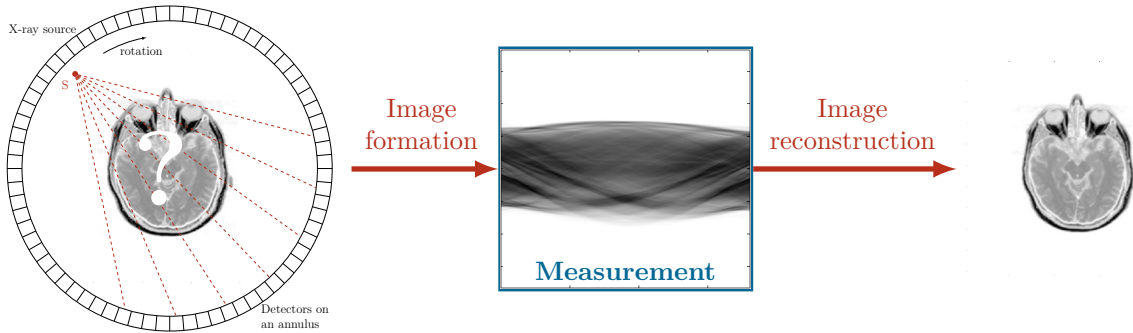


Figure 1: Image reconstruction in CT scan

More recently Truong and Nguyen have proposed the study of Radon transform defined on a generalized Cormack-type class of curves. We call here this class C_α and define it as

$$h_2(r^\alpha) \cos(\alpha(\theta - \varphi)) = h_1(p^\alpha),$$

where function h_2 fulfills a certain differential equation. They illustrated the inversion procedure in the case of special curve of C_1 . Because of the necessity of more results about the Radon transform over various manifolds of the plane, we propose, in this work, to derive more general results about the Radon transform defined over this family of curves and so to answer the following question :

Question 1. How to extend properties of the Radon transform over C_α -curves ?

In conventionnal CT-scan the attenuation factor is used as imaging agent. Attenuation represents the sum of each interaction involving the travelling photon and the considered matter and so informs about the loss of photons suffered by primary radiation. The main part of these interactions is due to scattering and mostly due to Compton effect when the energy range is larger than 140 keV. This phenomenon stands for the inelastic scattering of a photon by a free charged particle, usually an electron, see Fig. 2. Compton scattering is the most probable interaction of gamma-rays and high energy X-rays with atoms in living beings and so the scattered radiation can represent 80% of the emitting flux. Thus the scattered radiation can deteriorate the quality of the images.

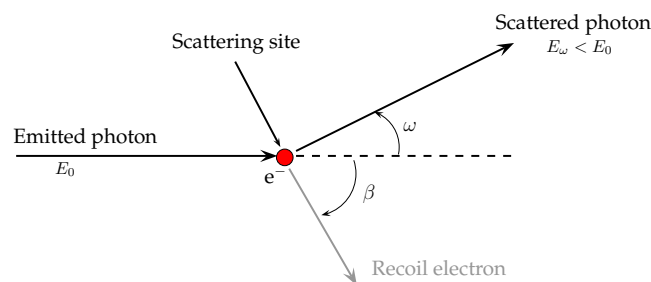


Figure 2: Principle of Compton scattering

Generally as the data quality is lowered, Compton scattering effects is treated as noise and must be eliminated. So far, in most image processing methods, the aim is to deal away with it, for example by filtering or by collimation. But eliminating all the scattered radiation may not be a smart move since this also means a loss of sensitivity and certainly a loss of valuable information.

Compton scattering tomography (CST) proposes to use the scattered radiation as imaging agent and no more to consider it as a noise. Several imaging concepts using the Compton scattering occurred with the evolution of technology, especially in the detection electronics.

In 1994, S. J. Norton proposed a Compton scattering tomographic device in which the primary radiation point-source is fixed and the point-like detector moves along a straight line passing through the point-source. Norton showed that integral data collected on isogonal arcs of circle can be useful for image reconstruction if they are identified with a Radon transform on arcs of circle passing through a fixed point (here the point source). We shall call it $CART_1$. Norton gave an inversion formula for the $CART_1$ via the so-called "Filtered Back-Projection" algorithm.

More recently Truong and Nguyen have proposed two novel modalities in Compton scattering tomography. In both cases image formation is modeled by a circular-arc Radon transform that we call here $CART_2$ and $CART_3$. Hence they established an unregularized inversion formula in circular harmonic domain for these two Radon transforms. Further, they derived the well-known filtered back-projection algorithm in both cases. However the singular value decomposition was not treated and no simulation results were proposed.

Actually the curves involved in these Radon transforms, $CART_{1,2,3}$, belong to the family C_1 . These potential applications in CST encourage to analyse the Radon transform over C_α and so to provide very powerful tools necessary to study corresponding Radon transforms and to solve the associated image reconstruction problem.

Question 2. How to take advantage of properties of the Radon transform defined on C_α to solve image formation and reconstruction problems in new modalities in CST ?

Although attenuation is considered as the imaging agent in CT-scan, it acts like a non-linear factor which hinders the modeling in others imaging techniques. Compton scattering tomography is no exception to the rule.

Indeed scattered flux suffers the attenuation effect and so associated modelings have to take it into account. Even though, if Novikov gave an inversion formula for the attenuated Radon transform, it remains an open issue for others modalities. Before the derivation of the analytical inversion formula, many correction methods were proposed : Generalized Chang correction (GCC), Iterative pre-correction (IPC), These methods are suited to deal with the attenuation factor hindering image formation in conventional tomography (SPECT-scan). Both GCC and IPC are iterative algorithms correcting step-by-step the attenuation factor in the image space for the GCC algorithm and in the data space for the IPC algorithm. The study of various modalities in Compton scattering tomography leads to consider new geometries even for the corresponding attenuation factor. So the establishment of a more generalized method to correct these new "attenuated problems" could represent a very powerful tool for the future.

Question 3. How to generalize the IPC algorithm in order to correct the attenuation effect with efficiency and stability ?

The requirement for fast and reliable diagnostics or therapy planning in modern healthcare systems has led to a wealthy development of hybrid imaging technologies. While traditional imaging techniques such as x-ray Computed Tomography (CT) and magnetic resonance imaging (MRI) provide information on patient's anatomy or on the location and extent of the disease, Positron Emission Tomography (PET) and Single-Photon Emission Computed Tomography (SPECT) are able to detect biomolecular changes (even prior to anatomic change) and the biochemical status or the physiological function of a human organ. The idea of combining imaging techniques has become a very powerful clinical tool. The introduction of combined PET/CT scanners revolutionized clinical practice and received widespread clinical acceptance. PET/MRI hybrid systems combining PET and MRI devices to obtain anatomical and molecular information simultaneously appeared later.

Nowadays, we observe that three major medical imaging modalities (CT, SPECT, PET) make use only of primary radiation whereas scattered radiation is considered as noise and then is routinely

eliminated or at least compensated for. Thus, the idea is to explore whether a bimodal imaging system can be built up based exclusively on the exploitation of scattered radiation. The concept of scattered radiation imaging was further promoted by pioneering work performed by Norton in 1994. At the beginning of the 21st century, a further advance was made in the use of scattered radiation for imaging, to be feasible for emission imaging. For a radiating (or made radiating) object, a SPECT gamma camera can be set to register, without having to rotate around this object, a set of images at different scattered energies. To use an optical analogy, it is as if the gamma camera records images at different wavelengths or using different color filters. The crux of the matter is that one can show that from this data set, a three-dimensional object reconstruction is possible. Moreover, a two-dimensional version of this scattered radiation has been shown to be feasible in the last few years, referred to as V-line emission imaging (VEI). Thus, it is tempting to ask the following question :

Question 4. How to combine novel modalities of CST as a new alternative multimodal imaging system ?

Contributions and outline

The manuscript is organized in three chapters which propose answers to issues discussed above.

Chapter I - Radon transform over generalized Cormack curves

During the last fifty years, progress in imaging systems using penetrating radiation has brought about new topics in mathematics and fueled intense research activities. Since its discovery by J. Radon, the Radon transform became a very powerful tool in many imaging modalities such as computerized tomography or SPECT. In the first place Radon transform represented the integral of a function over straight lines, but progresses in technology and advanced uses of physical phenomenon lead to new modelings and so to study new generalized Radon transforms. In 1981 Cormack showed the inversion of the Radon transform on a new family of curves (including straight lines) using harmonic expansion of functions and some interesting connections to orthogonal polynomials. In 2011 Truong and Nguyen have shown the invertibility of the Radon transform defined over C_α , however only one practical case was treated.

In this context we propose to establish the inversion formulae of Radon transforms defined on C_α using Cormack's procedure. This family is defined by a non-linear-first-order differential equation and respects symmetries and smoothness properties. Then we are interested in the particular case C_1 for which we establish the filtered back-projection algorithm, the singular value decomposition and the Chebyshev/Zernike expansion. Applications are numerous since this subclass leads to characterize a set of curves for which each associated Radon transform models a particular modality in Compton scattering tomography.

We can notice that in the Cormack's family, the case $\alpha = 1/2$ corresponds to a class of paraboloid. This support could be used in seismic exploration for instance. However the variable velocity stands for a major difficulty in the integral modeling of Radon-kind for such applications.

In section 1, we recall the properties of the standard Radon transform which are necessary for what follows. Thus main analytical inversion technique are presented in the case two-dimensional case and the study of Cormack about a family of curves, from which he could derive inversion formulae in the circular harmonic domain.

Then in section 2 we derive two inversion formulae of Radon transforms defined on C_α in circular harmonic domain :

- one numerically unstable which can be interpreted as the extension of the formula derived by Cormack given by

$$f_n(r) = -\frac{1}{\pi} \int_r^\infty \frac{T_n(p/r)}{\sqrt{p^2 - r^2}} \frac{dg_n(p)}{dp} dp ,$$

with g_n (resp. f_n) the circular harmonic components of the data $g(p, \varphi)$ (resp. of the image $f(r, \theta)$) and $T_n(\cdot)$ is the Chebyshev polynomial of first kind of order n ,

- and the regularised form of the previous one using a suited consistency condition .

These two inversion formulae are very similar to the ones shown by Truong and Nguyen and stands for their expression in original spaces. In addition the derivation makes appear the consistency conditions of curves C_α .

The filtered back-projection and the singular value decomposition are established in the particular case C_1 . In addition a more stable inverse transform is given in circular harmonic domain and is based on the Hilbert transform. Finally we give four examples of curves belonging to C_1 among which three of them will be studied in more details in Chapter II as the foundation for image formation in three modalities in Compton scattering tomography.

Results presented in this chapter were established in [J1].

Chapter II - Applications in Compton scattering tomography

Scattered radiation imaging is a promising modality in gamma-ray imaging with potential applications in many fields such as bio-medical imaging, gamma-ray astronomy, non-destructive testing, environmental survey and control, etc. S.J. Norton was the first one to propose a modality in CST of which measurement is approximated by an integral transform. In this manuscript, we call the associated Radon transform $CART_1$. He derived then an inversion formula which can be interpreted as a filtered back-projection. In 2010 and 2012 Truong and Nguyen have proposed two novels modalities in CST by transmission which are based on two new circular-arc Radon transform, called here $CART_2$ and $CART_3$. They derived for these two transforms the inversion formula in circular harmonic domain as well as the filtered back-projection. The curves implied in these three circular-arc Radon transform, $CART_{1,2,3}$, belongs to the special class C_1 for which we have derived in Chapter I the singular value decomposition and one more inversion formula in circular harmonic domain. Hence we propose to derive various inversion formulae for these three transforms associated to three modalities in CST and to implement these reconstruction method on noisy data. This survey permits to compare different proposed methods and to testify of the robustness of each methods. Furthermore numerical approaches are required for such transforms to solve image formation and reconstruction and so to prove the feasibility of such techniques. Thus different numerical methods are presented especially to implement the regularized inversion formulae in circular harmonic domain being inspired of the method of Chapman and Cary who dealt with the classical case.

Chapter II is organised as follows.

First we recall in section 1 the different interactions between matter and ionising radiation as well as generalities about conventional tomography (CT scan, SPECT scan and PET scan) and the motivations behind Compton scattering tomography.

Then we present in section 2,3,4 three different modalities of Compton scattering tomography ($CST_{1,2,3}$). Due to their relation with the family studied in Chapter I, it is logical to use these previous results to deduce the inversion formulae and the singular value decomposition for these modalities in Compton scattering tomography. According to the treated case, image formation and image reconstruction are discussed to be more suited numerically and so more easily implementable.

In section 5, simulation results in presence of noise (Poisson and gaussian noise) are given to show the feasibility of these modalities and proposed image reconstruction methods are compared.

The most part of results presented in this chapter were established in [J3,J4].

Chapter III - A new concept of bimodality in Compton scattering tomography

This Chapter can be separated in two parts : first we derive a new generalised correction algorithm, the generalised iterative pre-correction algorithm (GIPC), which enables to correct all attenuated Radon transforms as studied. Then we propose a new concept of bimodality in CST. Results derived in this Chapter were established in [J2].

Previously, we have presented the requirement for fast algorithm which permit to deal with the attenuation factor issue in imaging systems. Two main ways can be highlighted to correct iteratively the attenuation factor : to compensate its effect on the reconstructed image (see GCC) or on the attenuated data (see IPC proposed by Mazé in 1992). In this work we propose to generalize the concept of the IPC algorithm to a larger manifolds of transforms in order to solve iteratively the problem of attenuation correction in a general context. In particular this algorithm proposes a suited solution for "attenuated" modalities in CST studied in Chapter II.

Section 1 introduces the standard attenuation correction techniques used in CT/PET scan and CT/SPECT scan. The case of homogenous attenuation factor is presented as well as the heterogenous case.

In section 2, we prove that the following recurrence relation converges towards the original image f (GIPC algorithm)

$$f^{n+1} = f^n + T^{-1} \circ T^\Phi (f - f^n) \quad \text{with} \quad f^0 = 0 ,$$

with T an injective given operator and T^Φ its distorted version. We apply then this algorithm in the case of the attenuated CART_2 to prove its efficiency and feasibility in imaging sciences.

On the other hand we propose in section 3 a new concept of bimodality imaging based on Compton scattering tomography modalities similar to the PET/CT system in the sense that it combines transmission and emission modalities. In our novel imaging system, we consider two CST modalities. The first one was proposed by Norton and its modeling of image formation is based on a circular-arc Radon transform (CART_1). The second one was proposed by Truong and Nguyen. It works in emission and is based on a compounded V-line Radon transform (CVRT). We know that image quality in functional imaging is still a major issue in the medical research domain. In this context, the proposed system aims to increase image quality in emission tomography through the use of the single scattered radiation (which represents 80% of the emitted radiation). Another interest of this combination is that both modalities allow a two-dimensional image reconstruction from any scattered radiation collected by a one-dimensional collimated non-moving camera. This involves a new concept of detector with high energy resolution able to collect the scattered radiation.

Finally, we present new numerical results of the emerging CST system on a slice of the Zubal phantom using the proposed GIPC algorithm to correction attenuation problem in both modalities.

Publications

[C1] was done during this thesis but is not presented in this manuscript.

Journal Papers

- [J1] **G. Rigaud**. "On the inversion of the Radon transform on a generalized Cormack-type class of curves". *Inverse Problems*, Vol. 29 (2013) 115010.
- [J2] **G. Rigaud**, R. Régnier, M.K. Nguyen and H. Zaidi. "Combined modalities of Compton scattering tomography". *IEEE Transactions on Nuclear science*, Vol. 60, No. 3, june 2013.
- [J3] **G. Rigaud**, M.K. Nguyen, and A.K. Louis. "Novel Numerical Inversions of two Circular-Arc Radon Transforms in Compton scattering tomography". *Inverse Problems in Science and Engineering*, Vol. 20, No. 6, September 2012, 809-839.

- [J4] **G. Rigaud**, M.K. Nguyen, and A.K. Louis. "Modelling and Simulation Results on a new Compton scattering tomography modality". *Simulation Modelling Practice and Theory*, 33 (2013) 28-44.

International Conferences

- [C1] R. Régnier, **G. Rigaud** and M. K. Nguyen. "New approximated inversion of spherical Radon transform in SAR imaging". In *Proc. IEEE-International Conference Image Processing (ICIP)*. Melbourne, September 2013.
- [C2] O. Olvera Guerrero, **G. Rigaud**, R. Régnier and M. K. Nguyen. "Attenuation correction in a new modality of Compton scattering tomography". In *Interdisciplinary Symposium on Signal and Systems for Medical Applications (ISSMA)*. Paris, June 2013.
- [C3] **G. Rigaud**, R. Régnier, and M. K. Nguyen. "New bimodal scattered radiation tomographic imaging with attenuation and electron density correction algorithm". In *38th International Conference on Acoustics, Speech, and Signal Processing (ICASSP)*. Vancouver, Canada, May 2013.
- [C4] M. K. Nguyen, C. Faye, **G. Rigaud** and T. T. Truong. "A novel technological imaging process using ionizing radiation properties". In *9th IEEE - RVIF International Conference on Computing and Communications Technologies*. Ho Chi Minh City, Vietnam, February 2012.
- [C5] **G. Rigaud**, M. K. Nguyen and A. K. Louis. "Circular Harmonic Decomposition Approach for Numerical Inversion of Circular Radon Transforms". In *NCMIP (New Computational Methods for Inverse Problems)*. Cachan, France, May 2011.
- [C6] M.K. Nguyen and **G. Rigaud**. "A new circular-arc radon transform and the numerical method for its inverse resolution". In *8th International Conference of Numerical Analysis and Applied Mathematics (ICNAAM)*. AIP Conference Proceedings, 2010.
- [C7] **G. Rigaud**, M.K. Nguyen, and T.T. Truong. "Modeling and simulation results on a new compton scattering tomography". In *7th European Simulation and Modeling (EU-ROSIM)*, 2010.

National Journal Papers

- [P1] **G. Rigaud** et M.K. Nguyen. "Algorithmes de reconstruction d'images pour deux modalités de tomographie Compton par transmission". *Instrumentation, Mesures et Métrologie (I2M)*, Vol. 12, pp 199-223 (2012).

National Conferences

- [N1] **G. Rigaud** and M.K. Nguyen. "A new circular-arc radon transform and the numerical method for its inverse resolution". In *the proc. of GRETSI'2011*. Bordeaux, France, September 2011.
- [N2] **G. Rigaud** and M.K. Nguyen. "Une Nouvelle Modalité de Tomographie Compton". In *the proc. of Cofrend'2011*, Dunkerque, France, May 2011.

Radon transform over generalized Cormack curves

Since its introduction by J. Radon [55], the Radon transform became a very powerful tool in many imaging modalities such as computerized tomography or SPECT. First Radon transform represented the integral of a function over straight lines, but progresses in technology and advanced uses of physical phenomenon lead to new modelings and so to generalize the Radon transform on various manifolds other than straight lines. In 1981 Cormack showed the inversion of the Radon transform on a family of curves (including straight lines) using harmonic expansion of functions [12].

In this chapter, we focus on the work of Cormack and so the Radon transforms on a remarkable family of curves in the plane defined by

$$r^\alpha \cos(\alpha(\theta - \varphi)) = p^\alpha, \quad \text{with } |\theta - \varphi| \leq \frac{\pi}{2\alpha} .$$

Cormack showed several properties of the circular harmonic components of the Radon transforms on these two classes of curves and established an inversion formula in terms of the circular harmonic components of the unknown function. The purpose of this chapter is to extend these inversion formulae on an extended Cormack-type family of curves.

First we recall generalities about Radon transform and required tools for our study. A short review, however non-exhaustive, is also given about Radon transforms extended on different curves of the plane. Then we introduce in section 2 the family of curves we study and establish inversion formulae and determine the singular value decomposition for one particular subclass.

I.1 Review of Radon transform

I.1.1 Standard Radon transform

I.1.1.a Definition

The Radon transform of a function $f \in \mathcal{L}^2(\mathbb{R}^n)$ can be defined by

$$(\mathcal{R}f)(s, \Theta) = \int_{x \cdot \Theta = s} f(x) dx = \int_{\Theta^\perp} f(s\Theta + y) dy. \quad (\text{I.1})$$

This integral operator represents the projection of a given function over hyperplanes parametrized by the pair $(s, \Theta) \in \mathbb{R} \times S^{n-1}$. J. Radon introduced this transform in 1917 for pure mathematical reason [55]. Apparently, Lorentz had previously developed the transform in \mathbb{R}^3 , but he never published it. It was not until Allan Cormack reinvented it in 1963 [11] that it was used in tomography (see Chapter II for a more detailed application).

The adjoint Radon transform of a function $g \in \mathcal{L}^2(\mathbb{R} \times S^{n-1})$ is then deduced to

$$(\mathcal{R}^*g)(x) = \int_{S^{n-1}} g(x \cdot \Theta, \Theta) d\theta. \quad (\text{I.2})$$

This operator can be interpreted as the spreading of the value of $g(s, \Theta)$ over the hyperplane defined by $s = x \cdot \Theta$. This explains why this operator is often called the Back-projection operator.

The 2-dimensional case This particular case was rediscovered and studied by Cormack and we will focus on it because of its interest in tomography. As we need to give coordinates on the unit sphere S^1 , we denote the unit vector in direction $\varphi \in [0, 2\pi]$ as Θ and its orthogonal as Θ^\perp :

$$\Theta = (\cos \varphi, \sin \varphi), \quad \Theta^\perp = (-\sin \varphi, \cos \varphi). \quad (\text{I.3})$$

We define

$$L(s, \varphi) = \{x \in \mathbb{R}^2 | x \cdot \Theta(\varphi) = s\} \quad (\text{I.4})$$

to be the line perpendicular to $\Theta(\varphi)$ and s directed units from the origin. We see below that equivalently we can define this line in polar coordinates as

$$s = r \cos(\theta - \varphi) \quad \text{with} \quad \varphi - \frac{\pi}{2} < \theta < \varphi + \frac{\pi}{2}. \quad (\text{I.5})$$

The Radon transform of a function $f \in \mathcal{L}^2(\mathbb{R}^2)$ is given by

$$\mathcal{R}f(s, \varphi) = \int_{(x,y) \in L_{s,\varphi}} f(x, y) dl = \int_{\mathbb{R}} f(s\Theta + t\Theta^\perp) dt, \quad (\text{I.6})$$

and is continuous. Another definition using Dirac distribution can be useful

$$\mathcal{R}f(s, \varphi) = \int_{\mathbb{R}^2} f(x, y) \delta(s - x \cos \varphi - y \sin \varphi) dx dy. \quad (\text{I.7})$$

Thanks to this last definition, the point spread function, that is to say the Radon transform of an impulsional function defined as

$$f(x, y) = \delta(x - x_0) \delta(y - y_0), \quad (\text{I.8})$$

can be express as

$$\mathcal{R}f(s, \varphi) = \delta(s - x_0 \cos \varphi - y_0 \sin \varphi) . \quad (\text{I.9})$$

The support curve of the Radon transform is then a sinusoidal function, $s = x_0 \cos \varphi + y_0 \sin \varphi$, and inspired the name of measurement in tomography : the sinogram (see Chapter II).

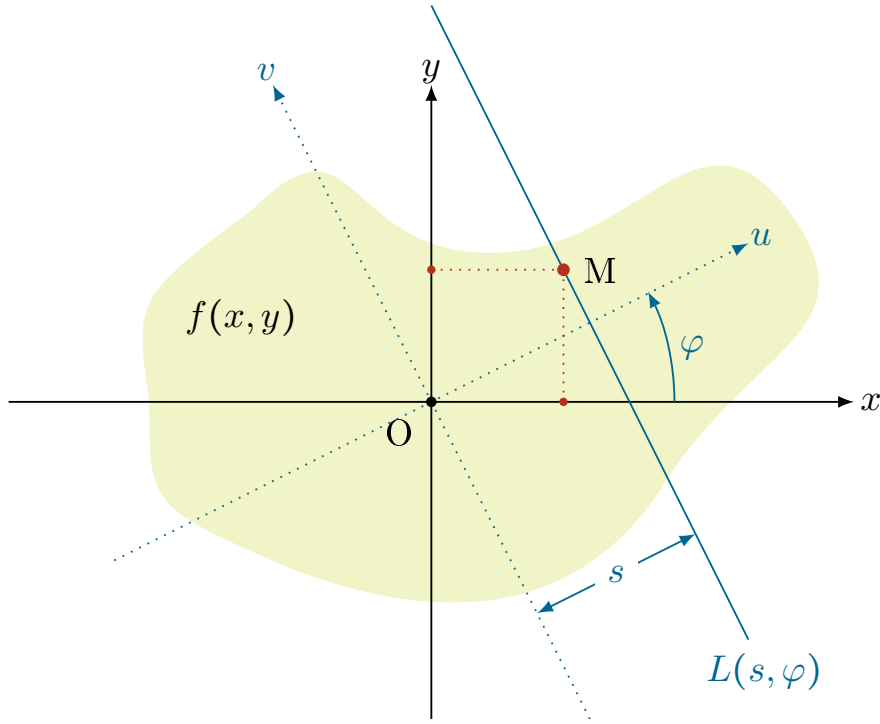


Figure I.1: Geometric setup of the integration along a straight line

I.1.1.b Inversion formulae and reconstruction algorithms

There exist a lot of image reconstruction methods suited for the Radon transform. We can denote two great fields of reconstruction ways : a functional approach where we work on functions and operators and a discrete approach in which data and functions are directly considered as discrete vectors.

In the first approach we can classify it in two groups of methods :

- *Analytical methods* : One can obtain an analytical inversion formula applied directly on the data, or sometimes through a dual space.

Slice theorem This theorem relates the Fourier transform of the measurement with respect to s to the 2D-Fourier transform of the original function.

Let $f \in \mathcal{L}^2(\mathbb{R}^2)$. Then,

$$\frac{1}{\sqrt{2\pi}} \mathcal{F}^1(\mathcal{R}f)(\nu, \theta) = \mathcal{F}^2(f)(\nu\theta). \tag{I.10}$$

This theorem shows why \mathcal{R} is injective on domain $\mathcal{L}^2(\mathbb{R}^2)$: if $\mathcal{R}f \equiv 0$, then $\mathcal{F}^2(f) \equiv 0$ which shows that f is zero by injectivity of the Fourier transform.

Filtered Back-projection Let $f \in \mathcal{L}^2(\mathbb{R}^2)$. Then

$$f(x) = \frac{1}{4\pi} \mathcal{R}^* (\mathcal{I}^{-1} \mathcal{R}f)(x). \tag{I.11}$$

This formula involves the adjoint operator, $\mathcal{R}^* : \mathcal{L}^2([-1, 1] \times S^1) \rightarrow \mathcal{L}^2([0, 1] \times S^1)$, of the Radon transform which gives its name of "back-projection". And the Riesz potential acts as a filtering of the data, $\mathcal{R}f$. However the term $(\mathcal{I}^{-1}\mathcal{R}f)$ has to be understood as a distribution. This last term is equivalent to apply a ramp filter of the form ν on the Fourier transform of the projections and then to return in the measurement space. In practice this formula is applied by truncating and smoothing the multiplier ν and writing this truncated multiplier as a convolution operator in s [44, 46, 56].

- *Decomposition methods* : One projects the original function and its associated data in a well-chosen basis in order to find an explicit relationship between expansion coefficients of both. The singular value decomposition of such a problem is typically the most researched approach.

Singular value decomposition Properties of the Radon transform in circular harmonic domain lead Cormack to derive its singular value decomposition. We recall this result with the required properties and definition.

Definition I.1.1. The 2D Radon transform \mathcal{R} is defined for a function $f : [0, 1] \times S^1 \rightarrow \mathbb{R}$ by

$$\mathcal{R}f(p, \varphi) = \int_{[0,1] \times S^1} f(r, \theta) \delta(p - r \cos(\theta - \varphi)) r dr d\theta ,$$

with $(p, \varphi) \in [-1, 1] \times S^1$.

Lemma I.1.2. The set $\left\{ v_n^m(r, \theta) = \sqrt{\frac{|n| + 2m + 1}{\pi}} R_n^m(r) e^{in\theta} \right\}$ for $n \in \mathbb{Z}$ and $m \in \mathbb{Z}^+$ forms a complete orthonormal basis set in $\mathcal{L}^2([0, 1] \times S^1)$.

Lemma I.1.3. The set $\left\{ u_n^m(p, \varphi) = \sin((|n| + 2m + 1) \cos^{-1}(p)) \frac{e^{in\varphi}}{\pi} \right\}$ for $n \in \mathbb{Z}$ and $m \in \mathbb{Z}^+$ forms a complete orthonormal basis set for even functions in $\mathcal{L}^2([-1, 1] \times S^1, W)$ with the weight function

$$W(p, \varphi) = (1 - p^2)^{-1/2} . \quad (\text{I.12})$$

Remark I.1.4. The parity of the Radon transform explains the presence of the frequency $|n| + 2m + 1$ in its decomposition.

Theorem I.1.5. The system $\left(u_n^m(p, \varphi), v_n^m(r, \theta), \sqrt{\frac{4\pi}{|n| + 2m + 1}} \right)$ for $n \in \mathbb{Z}$ and $m \in \mathbb{Z}^+$ gives a complete singular system of $\mathcal{R} : \mathcal{L}^2([0, 1] \times S^1) \rightarrow \mathcal{L}^2([-1, 1] \times S^1)$.

Proof. See Cormack [11]. □

Remark I.1.6. The results for the n -dimensional Radon transform was given by Louis in [31].

In this manuscript, we focus on analytical and decomposition methods. However, we recall here the principle of the algebraic field for information purposes.

Unlike analytical methods, where the discretization formulas is made at the end of procedure, algebraic methods are based on an initial discretization of the inverse problem. The unknown distribution function f and measurement g are considered as discrete functions. The forward problem is formulated as a linear system of equations:

$$g = Rf, \quad (\text{I.13})$$

where R is the projection matrix and g and f are vectors. This system can be solved according to two points of view :

- *Deterministic methods* : Direct methods correspond to the resolution of the system by direct inversion of the projection matrix, R . Among these methods, the technique of singular value decomposition (SVD, seen above but with discrete data) is used to regularize the problem by truncating too small singular values (TSVD).

Iterative methods search to find a solution by a sequence of estimates [14]. The most common method is the ART (algebraic reconstruction technique) [17], which follows the method of Kaczmarz.

In conventional imaging, projection matrices are sparse because a ray intersects a limited number of voxels, which accelerates the rate of convergence of this method.

- *Statistical methods* : Statistical approaches are based on a direct model that considers measurement, g_i , as the flow of photons arriving at the detector dependent on stochastic processes (Poisson noise, Gaussian noise ...). The reconstruction problem becomes the probabilistic estimation of values f_i .

One usually solves this estimation problem by maximum likelihood methods [28, 39] for example based on the Expectation Maximization (EM) [60] algorithm. Most of these methods incorporates a Bayesian regularization [19] for introducing an *a priori* modeling of the object.

I.1.1.c The attenuated Radon transform

Because of its use in tomographic imaging, the inversion of the Radon transform said "attenuated" was the subject of intensive investigations by many mathematicians until its discovery by Novikov [50]. Natterer then gave a different proof [45]. Before them Tretiak solved this problem in the case of a constant attenuation [66].

Let f, a be continuous functions of compact support in \mathbb{R}^2 and let θ be a unit vector. We define the divergent beam X-ray transform of a at $x \in \mathbb{R}^2$ in direction $\theta \in S^1$ by

$$(\mathcal{D}a)(x, \theta) = \int_0^\infty a(x + t\theta) dt \quad (\text{I.14})$$

and so the attenuated Radon transform by

$$(\mathcal{R}_a f)(s, \theta) = \int_{x \cdot \theta = s} e^{-(\mathcal{D}a)(x, \theta^\perp)} f(x) dx \quad (\text{I.15})$$

where dx stands for the restriction of the Lebesgue measure in \mathbb{R}^2 to $x \cdot \theta = s$. Its adjoint can be written as

$$(\mathcal{R}_a^* g)(x) = \int_{S^1} e^{-(\mathcal{D}a)(x, \theta^\perp)} g(x \cdot \theta, \theta) d\theta . \quad (\text{I.16})$$

We put

$$h(s, \theta) = \frac{1}{2} (I + i\mathcal{H})(\mathcal{R}a)(s, \theta) , \quad (\text{I.17})$$

with I the identity operator. Then f is reconstructed by the following inversion formula

$$f(x) = \frac{1}{4\pi} R \operatorname{div} \int_{S^1} \theta e^{(\mathcal{D}a)(x, \theta^\perp)} (e^{-h} \mathcal{H} e^h \mathcal{R}_a f)(x \cdot \theta, \theta) d\theta . \quad (\text{I.18})$$

shown by Natterer [45] or equivalently by

$$f(x) = (-) \frac{1}{4\pi} \operatorname{Re} \operatorname{div} \int_{S^1} \theta e^{-(\mathcal{D}\alpha)(x, \theta^\perp)} \left(e^{h\mathcal{H}} e^{\bar{h}\check{y}} \right) (x \cdot \theta, \theta) d\theta . \quad (\text{I.19})$$

with $\check{y}(s, \theta) = \mathcal{R}_\alpha f(-s, -\theta)$ shown by Novikov [50].

I.1.2 Cormack's class of curves and Radon transform

In 1963 Allan Cormack has established the inversion formula in circular harmonic domain on a class of curves to which the straight line (support of the 2D-Radon transform) belongs.

Radon transform on Cormack's family of curves Let (r, θ) and (p, φ) be the polar coordinate in the plane of a point of the curve and of its characteristic point. We can thus define α -curves as

$$r^\alpha \cos(\alpha(\theta - \varphi)) = p^\alpha, \quad \text{avec } |\theta - \varphi| \leq \frac{\pi}{2\alpha} . \quad (\text{I.20})$$

These curves are defined for $\alpha > 0$. If $\alpha < 0$, we put $\beta = -\alpha$ and define the β -curves as

$$p^\beta \cos(\beta(\theta - \varphi)) = r^\beta, \quad \text{avec } |\theta - \varphi| \leq \frac{\pi}{2\beta} . \quad (\text{I.21})$$

The results for the two families of curves are quite similar because a β -curve can be obtained from an α -curve with $\alpha = \beta$ by the transform in the unit circle $((r, \theta) \rightarrow (1/r, \theta))$ and vice versa. Therefore, in the following, we just study α -curves. We can denote the special case $\alpha = 1$ which is the straight line and so the classical Radon transform.

Cormack studied this family for the forward and inverse Radon transforms. The forward Radon transform on α -curves is given by

$$g(p, \varphi) = p \int_{-\pi/2\alpha}^{\pi/2\alpha} f\left(\frac{p}{\cos^{1/\alpha}(\alpha\gamma)}, \varphi + \gamma\right) \frac{d\gamma}{\cos^{1+1/\alpha}(\alpha\gamma)} , \quad (\text{I.22})$$

where $\gamma = \theta - \varphi$. Now considering the circular harmonic decomposition of f and g ,

$$f_n(r) = \frac{1}{2\pi} \int_0^{2\pi} f(r, \theta) e^{-in\theta} d\theta \quad \text{and} \quad g_n(p) = \frac{1}{2\pi} \int_0^{2\pi} g(p, \varphi) e^{-in\varphi} d\varphi , \quad (\text{I.23})$$

Cormack proved that the forward Radon transform becomes

$$g_n(p) = 2 \int_p^\infty f_n(r) \frac{\cos\left(\frac{n}{\alpha} \cos^{-1}\left(\frac{p}{r}\right)^\alpha\right)}{\sqrt{1 - (p/r)^{2\alpha}}} dr . \quad (\text{I.24})$$

We put $r^\alpha = s$ and $p^\alpha = q$ in order to simplify the expression and

$$F_n(s) = \frac{s^{1/\alpha-1}}{\alpha} f_n(s^{1/\alpha}) \quad \text{and} \quad G_n(q) = g_n(q^{1/\alpha}) . \quad (\text{I.25})$$

Therefore the forward Radon transform on α -curves becomes

$$G_n(q) = 2 \int_q^\infty F_n(s) \frac{\cos\left(\frac{|n/\alpha|}{\alpha} \cos^{-1}\left(\frac{q}{s}\right)\right)}{\sqrt{1 - (q/s)^2}} ds . \quad (\text{I.26})$$

Unstable and stable inversion formula The solution of eq. (I.26) were shown to be

$$F_n(t) = -\frac{1}{\pi t} \int_t^\infty G'_n(q) \frac{\cosh(|n/\alpha| \cosh^{-1}(q/t))}{\sqrt{(q/t)^2 - 1}} \quad (\text{I.27})$$

where the prime denotes a derivative. In principle, one can use equation (I.27) to perform numerical computations. However it is numerically unstable. Assuming that the original function is bounded, a close inspection of the integral kernel of equation (I.27) shows that it behaves as

$$\lim_{q \rightarrow +\infty} \frac{\cosh(|l| \cosh^{-1}(q/t))}{q \sqrt{(q/t)^2 - 1}} \approx \lim_{u \rightarrow +\infty} 2 e^{(|l|-2)u}, \quad (\text{I.28})$$

where $u = \cosh^{-1}(q/t)$. Equation (I.28) presents an apparent divergence when $|l| > 2$, since for $q \rightarrow \infty$ the integrand grows very rapidly. The presence of noise in the data $g_n(1/q)$ for large q is reflected into the calculation of $f_l(r)$ which prevents simulation studies. Thus equation (I.27) needs to be regularized.

Cormack proposed a regularization procedure based on consistency conditions of the circular harmonic components of the data

$$\int_0^\infty \frac{dG_n(q)}{dq} q^{\alpha_n} dq = 0 \quad \text{for } \alpha_n = (n/\alpha - 1), (n/\alpha - 3), \dots, > 0. \quad (\text{I.29})$$

Thanks to these conditions and the identity of the Tchebychev polynomial linking the first kind ($T_l(\cdot)$) to the second kind Tchebyshev polynomial ($U_l(\cdot)$)

$$\frac{T_l(x)}{\sqrt{x^2 - 1}} = \frac{(x - \sqrt{x^2 - 1})^l}{\sqrt{x^2 - 1}} + U_{l-1}(x),$$

he could derive the following more stable inversion formula

$$F_n(t) = \frac{1}{\pi t} \int_0^t \frac{dG_n(q)}{dq} U_{|n/\alpha|-1}(q/t) dq - \frac{1}{\pi t} \int_t^\infty \frac{dG_n(q)}{dq} \frac{\left((q/t) - \sqrt{(q/t)^2 - 1}\right)^{|n/\alpha|}}{\sqrt{(q/t)^2 - 1}} dq. \quad (\text{I.30})$$

Chapman and Cary's numerical approach However the stable inversion formula proposed by Cormack, eq. (I.30)) remains hard to implement because of the derivative of the data. Then Chapman and Cary [8] proposed a discrete approach in the case of the classical Radon transform ($\alpha = 1$). Considering T as the finite maximum value of t and making the change of variable $q = r \cos \chi$ and $q = r \cosh \chi$ in the first and second integrals, the transform (I.30) becomes

$$F_n(t) = \frac{1}{\pi} \int_0^{\frac{\pi}{2}} d\chi G'_n(t \cos \chi) \sin(n\chi) - \frac{1}{\pi} \int_0^{\cosh^{-1}(T/t)} d\chi G'_n(t \cosh \chi) e^{-n\chi} \quad (\text{I.31})$$

Now we can define the discretized forms of $F_n(t)$ and $G_n(q)$ as

$$G_{nk} = G_n(k\Delta t) \quad \text{and} \quad F_{nj} = F_n(j\Delta t), \quad (\text{I.32})$$

where $(j, k) \in [0, K]^2$ with $K = \frac{T}{\Delta t}$. The derivative $G'_n(q)$ can be approximated by coefficients a_{nk} where:

$$a_{nk} = \frac{G_{n(k+1)} - G_{nk}}{\Delta t}. \quad (\text{I.33})$$

Equation (I.30) yields

$$F_{nj} = \frac{1}{\pi} \left[\sum_{k=0}^{j-1} a_{nk} \left(I_n(\chi_{j(k+1)}) - I_n(\chi_{jk}) \right) + \sum_{k=j}^{K-1} a_{nk} \left(J_n(\chi_{j(k+1)}) - J_n(\chi_{jk}) \right) \right] \quad (\text{I.34})$$

in terms of the primitive functions

$$I_n(\chi_{jk}) = \int^{\chi_{jk}} \sin(|n|x) dx = -\frac{\cos(|n|\chi_{jk})}{|n|} \quad \text{for } n \neq 0 \quad (\text{I.35})$$

and

$$J_n(\chi_{jk}) = \int^{\chi_{jk}} e^{-|n|x} dx = \begin{cases} -e^{-|n|\chi_{jk}}/|n| & \text{if } n \neq 0 \\ \chi_{jk} & \text{if } n = 0 \end{cases} \quad (\text{I.36})$$

where

$$\chi_{jk} = \begin{cases} \cos^{-1}\left(\frac{k}{j}\right) & \text{for } 0 \leq k \leq j \\ \cosh^{-1}\left(\frac{k}{j}\right) & \text{for } j \leq k \leq K. \end{cases} \quad (\text{I.37})$$

Finally the discretized form of the reconstruction equation appears as

$$F_{nj} = \frac{1}{|n|\pi} \left[\sum_{k=0}^{j-1} a_{nk} \left(\cos |n|\chi_{j(k+1)} - \cos |n|\chi_{jk} \right) + \sum_{k=j}^{K-1} a_{nk} \left(e^{-|n|\chi_{j(k+1)}} - e^{-|n|\chi_{jk}} \right) \right]. \quad (\text{I.38})$$

And for $n = 0$ a separate expression exists

$$F_{0j} = -\frac{1}{\pi} \sum_{k=j}^{K-1} a_{0k} \left(\chi_{j(k+1)} - \chi_{jk} \right). \quad (\text{I.39})$$

Once the F_{nj} are computed, the final step consists in working out the summation in discrete form.

$$F_j(\theta) = \sum_l F_{nj} e^{in\theta}. \quad (\text{I.40})$$

The idea behind the differentiation of the primitives of the integrand is quite simple. As the computation of the derivative is performed by a simple differentiation (first order) between steps k and $k + 1$, the question is how to calculate the corresponding integrand for the same sampling. Then this integral cannot be computed by taking the integrand in k or even in $k + 1$. Thus the computation of the corresponding integrand by differentiation of its primitive solves this problem.

I.1.3 Extension to others kind of curves in the plane

The Radon transform introduced by J. Radon and massively used in imaging concept led mathematicians to extend this transform to different geometry. A lot of pioneering works derived properties of the Radon transform defined over geometric structures. For example Quinto studied the invertibility and the injectivity of circular Radon transforms [1]. In the past decades, the inversion of Radon transforms on circles centered on a smooth curve has been established in the context of Synthetic Aperture Radar [57, 64] or in thermo-acoustic tomography [16]. Later Kurusa generalized invertibility for Radon transform on curves having strictly convex distance function in two-point homogeneous spaces of constant curvature but no practical curve was given [26, 27].

As this manuscript is focused on generalized Radon transforms over the plane, we focus our discussion on this topic and we propose here some examples of extension of the Radon transform to special curves of the plane.

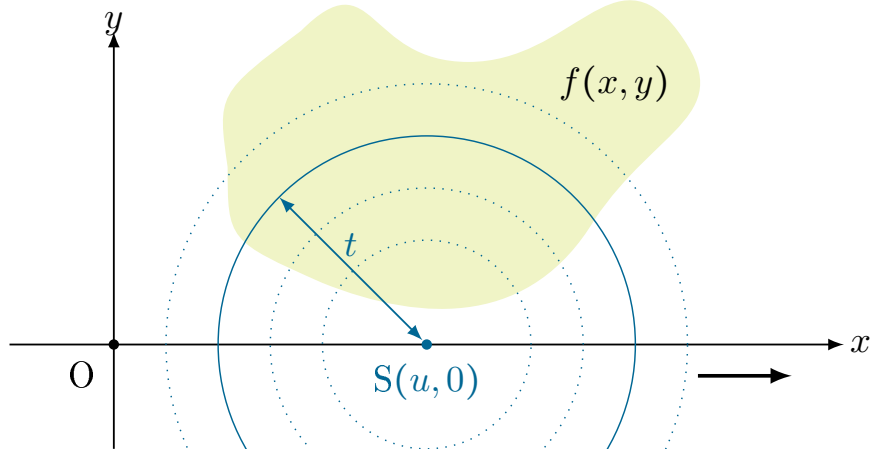


Figure I.2: Geometric setup and scanning of the medium for Redding's curve

Redding's curves In [57] Redding defined a circular Radon transform of a function to be the path integral of the function along a circle of radius t centered on the point $(u, 0)$ on the x -axis, see Figure I.2. This can be written as

$$g(u, t) = \int_{\mathbb{R}^2} f(x, y) \delta(t - \sqrt{(x-u)^2 + y^2}) dx dy. \quad (\text{I.41})$$

Then he proved the following inversion formula

$$\mathcal{F}^2(f)(\nu, \rho) = \frac{|\rho|}{2} g^{(F, H_0)}(\nu, \sqrt{\rho^2 + \nu^2}) \quad (\text{I.42})$$

where $g^{(F, H_0)}$ is the Fourier transform of g with respect to the first variable u and zero-order Hankel transform with respect to the second variable t of $g(u, t)$, given by,

$$g^{(F, H_0)}(\nu, \rho) = 2\pi \int_{-\infty}^{+\infty} \int_0^{+\infty} g(u, t) e^{2i\pi\nu u} J_0(2\pi t \rho) t dt du. \quad (\text{I.43})$$

This approach to image formation provides an alternative view to understanding the SAR image formation process and can be used to develop algorithms that are free of the range curvature limitations of standard techniques used in SAR.

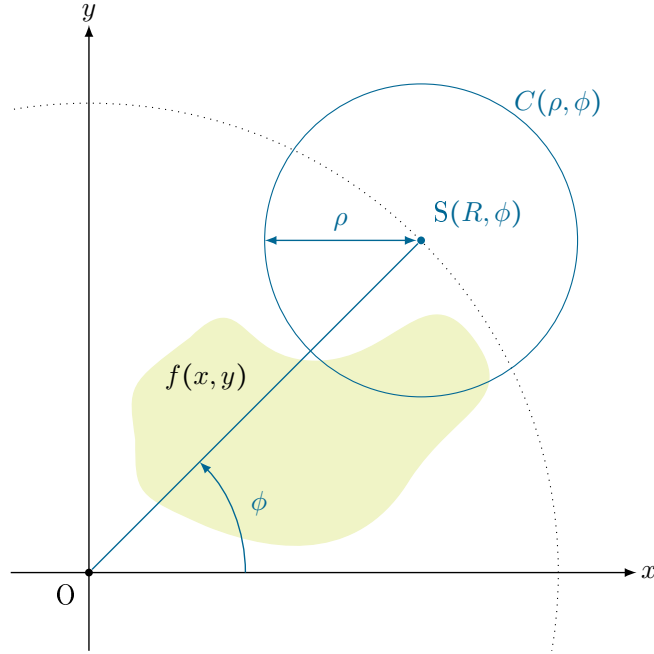
Ambartsoumian curves In [2] Ambartsoumian et al. derived the inversion formula in CHD of a circular Radon transform on an annulus, see Figure I.3. The circular Radon transform of a function f is then

$$g(\rho, \phi) = \int_{C(\rho, \phi)} f(r, \theta) ds. \quad (\text{I.44})$$

The inversion formula is obtained in CHD thanks to its link with a Volterra equation of the second kind. Thus putting $F_n(u) = f_n(R - u)$,

$$K_n(\rho, u) = \frac{4\rho(R-u)T_{|n|}\left(\frac{(R-u)^2 + R^2 - \rho^2}{2R(R-u)}\right)}{\sqrt{(u+\rho)(2R+\rho-u)(2R-\rho-u)}}, \quad (\text{I.45})$$

$$G_n(t) = \frac{1}{\pi K_n(t, t)} \frac{d}{dt} \int_0^t \frac{g_n(\rho)}{\sqrt{t-\rho}} d\rho \quad (\text{I.46})$$

Figure I.3: Geometric setup of integration along the circle $C(\rho, \phi)$

and

$$L_n(t, u) = \frac{1}{\pi K_n(t, t)} \frac{\partial}{\partial t} \int_u^t \frac{K_n(\rho, u)}{\sqrt{\rho - u} \sqrt{t - \rho}} d\rho, \quad (\text{I.47})$$

authors could give the exact inversion formula as

$$F_n(t) = G_n(t) + \int_0^t H_n(t, u) G_n(u) du, \quad (\text{I.48})$$

where the resolvent kernel $H_n(t, u)$ is given by the series of iterated kernels

$$H_n(t, u) = \sum_{i=1}^{+\infty} (-1)^i L_{n,i}(t, u), \quad (\text{I.49})$$

defined by

$$L_{n,1}(t, u) = L_n(t, u), \quad (\text{I.50})$$

and

$$L_{n,i}(t, u) = \int_u^t L_{n,1}(t, x) L_{n,i-1}(x, u) dx, \quad \forall i \geq 2. \quad (\text{I.51})$$

This circular Radon transform is involved in the modeling of thermoacoustic and photacoustic tomography which are two emerging medical imaging modalities.

Truong and Nguyen's broken lines The paper [68] provides a deep study of the Radon transform over a variety of broken lines which can involve many applications in tomography. In particular authors introduce the principle of a V-line Radon transform based on a coupled transmission-reflection modality in tomography. The reflection is ensured by a mirror, see Figure I.4. The forward transform is expressed by

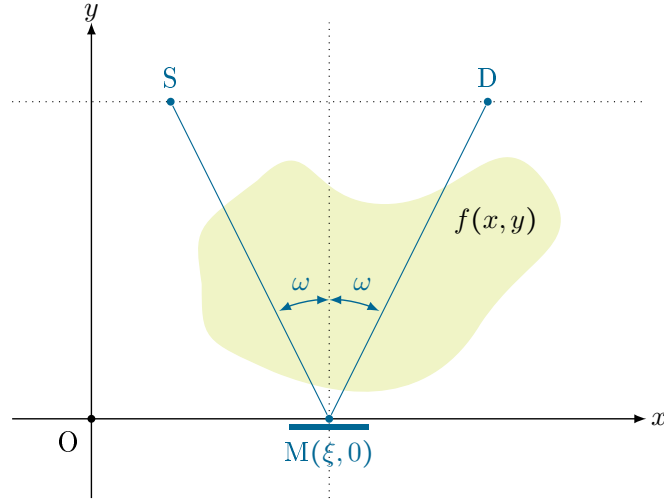


Figure I.4: Parameters of the V-line Radon transform with a mirror

$$g(\xi, \tau) = \int_0^\infty f(\xi \pm r \sin \omega, r \cos \omega) dr \quad (\text{I.52})$$

where $\tau = \tan \omega$ and with $0 < \omega < \pi/2$. Then authors derived an inversion formula which can be understood as a Filtered Back-projection. It is given by

$$f(x, y) = \frac{1}{2\pi^2} \int_0^\infty \frac{d\tau}{\sqrt{1+\tau^2}} \left(p.v. \int_{\mathbb{R}} d\xi \left(\frac{g'(\xi, \tau)}{\xi - x - y\tau} + \frac{g'(\xi, \tau)}{\xi - x + y\tau} \right) \right), \quad (\text{I.53})$$

where *p.v.* stands for the Cauchy principal value and the prime denotes the ξ -derivative. This modeling then proposes an interesting alternative approach in non-destructive testing since no rotation is required for the reconstruction of the attenuation map.

In the same paper, authors establishes the theory for another kind of Radon transform - the compounded V-line Radon transform (CVRT). In Chapter III, we combine the modality based on the CVRT with a transmission modality in CST based on a circular Radon transform (CART_1). This last is presented in Chapter II. Thus see Chapter III for more details about this V-line Radon transform.

In 2012 Truong and Nguyen [69] proposed the study of a generalized Cormack-type class of curves, however only one practical case was treated. In next section, we study the Radon transform over a family of curves which are strongly related to the one proposed in [69]. The analysis of these new Radon transforms leads to the establishment of inversion formulae and to the singular value decomposition in a particular case.

I.2 Inverse Radon transform over generalized Cormack curves

I.2.1 Definition and forward problem

In 1981, A. M. Cormack [12, 13] studied Radon transforms on a remarkable family of curves in the plane defined by

$$r^\alpha \cos(\alpha(\theta - \varphi)) = p^\alpha \quad \text{with} \quad |\theta - \varphi| \leq \frac{\pi}{2\alpha}.$$

Cormack showed several properties of the circular harmonic components of the Radon transforms on these two classes of curves and has established an inversion formula in terms of the circular harmonic components of the unknown function. The purpose of this section is to extend these inversion formulae on a generalized Cormack-type family of curves. Then, we are interested in the following kind of function

$$\mathcal{A}f(p, \varphi) = \int_{(r, \theta) \in C_\alpha} f(r, \theta) dl \quad (\text{I.54})$$

which corresponds to the integral of a certain function f over the curve C_α parametrized by p and φ . First we define the spaces used for (p, φ)

- $\mathbb{R}_1 = [-b_1, -a_1] \cup [a_1, b_1]$ with $(a_1, b_1) \in \bar{\mathbb{R}}^2$,
- $\mathbb{H}_1 = \mathbb{R}_1 \times S^1$,

and for (r, θ)

- $\mathbb{R}_2 = [a_2, b_2]$ with $(a_2, b_2) \in \bar{\mathbb{R}}^2$,
- $\mathbb{H}_2 = \mathbb{R}_2 \times S^1$.

In what follows we consider only functions of $\mathcal{L}^2(\mathbb{H}_1)$ for data and of $\mathcal{L}^2(\mathbb{H}_2)$ for original functions.

Definition I.2.1. We define the class of curves, C_α by

$$C_\alpha(p, \varphi) = \left\{ (r, \theta) \in \mathbb{R}_2 \times S^1 \mid h_1(p^\alpha) = h_2(r^\alpha) \cos(\alpha(\theta - \varphi)), |\theta - \varphi| \leq \frac{\pi}{2\alpha} \right\} \quad (\text{I.55})$$

$\alpha > 0$ and $h_1 : \mathbb{R}_1 \rightarrow \mathbb{R}$ and $h_2 : \mathbb{R}_2 \rightarrow \mathbb{R}^+$ are diffeomorphisms and h_2 is such that

$$\alpha^2 r^{2\alpha} \left(\frac{h_2'(r^\alpha)}{h_2^2(r^\alpha)} \right)^2 - \frac{1}{h_2^2(r^\alpha)} = k, \quad (\text{I.56})$$

where prime denotes the derivative and $k \in \mathbb{R}$ is an arbitrary constant.

The function h_1 has to be odd by definition or by construction. In that case the space \mathbb{R}_1 can be reduced to $[a_1, b_1]$. However \mathbb{R}_1 shall have the same definition than previously when the singular value decomposition will be established.

Remark I.2.2. This class was first defined in [69] except that no scaling of the variable p was considered (function h_1 here). This is understandable since this function has no effect on the inversion problem. However, we take it into account here to study the inversion problem in a unified form and to simplify the use of results presented below in practical applications.

We notice that for h_1 and h_2 identity functions, C_α represents α -curves and that for h_1 and h_2 of the form $1/x$, it represents β -curves studied by Cormack.

Proposition I.2.3. *The 2D Radon transform \mathcal{A} of a function $f : \mathbb{H}_2 \rightarrow \mathbb{R}$ over C_α is defined by*

$$\mathcal{A}f(p, \varphi) = \sqrt{k + \frac{1}{h_1^2(p^\alpha)}} \int_{-\pi/2\alpha}^{\pi/2\alpha} d\gamma \left\{ \frac{1}{\alpha} \frac{h_2^2(r^\alpha)}{h_2'(r^\alpha)} f(r, \gamma + \varphi) \right\}_{r=(h_2^{-1}(\frac{h_1(p^\alpha)}{\cos(\alpha\gamma)}))^{1/\alpha}} \quad (\text{I.57})$$

with $(p, \varphi) \in \mathbb{H}_1$.

Proof. We start from the definition of our transform

$$\mathcal{A}f(p, \varphi) = \int_{(r, \theta) \in C_\alpha} f(r, \theta) dl \quad (\text{I.58})$$

then the proof consists in computing the differential element $dl = \sqrt{dr^2 + r^2 d\gamma^2}$. Deriving $r(\gamma)$ according to Definition I.2.1, we have

$$dr = \frac{\tan(\alpha\gamma)}{\cos(\alpha\gamma)} \frac{h_1(p^\alpha)}{\alpha} \left(h_2^{-1} \left(\frac{h_1(p^\alpha)}{\cos(\alpha\gamma)} \right) \right)^{1/\alpha-1} \left(h_2^{-1} \right)' \left(\frac{h_1(p^\alpha)}{\cos(\alpha\gamma)} \right) d\theta \quad (\text{I.59})$$

and then

$$\begin{aligned} dl &= d\theta \left\{ \frac{1}{\alpha} \frac{h_2^2(r^\alpha)}{h_2'(r^\alpha)} \sqrt{\alpha^2 r^{2\alpha} \left(\frac{h_2'(r^\alpha)}{h_2^2(r^\alpha)} \right)^2 + \frac{1}{h_1^2(p^\alpha)} - \frac{1}{h_2^2(r^\alpha)}} \right\}_{r=(h_2^{-1}(\frac{h_1(p^\alpha)}{\cos(\alpha\gamma)}))^{1/\alpha}} \\ &= d\theta \left\{ \frac{1}{\alpha} \frac{h_2^2(r^\alpha)}{h_2'(r^\alpha)} \sqrt{k + \frac{1}{h_1^2(p^\alpha)}} \right\}_{r=(h_2^{-1}(\frac{h_1(p^\alpha)}{\cos(\alpha\gamma)}))^{1/\alpha}}, \end{aligned} \quad (\text{I.60})$$

assuming that

$$\alpha^2 r^{2\alpha} \left(\frac{h_2'(r^\alpha)}{h_2^2(r^\alpha)} \right)^2 - \frac{1}{h_2^2(r^\alpha)} = k. \quad (\text{I.61})$$

The proof is completed. □

This proof makes arise the requirement in h_2 to fulfill a given differential equation. Thus this condition leads to a separation of different radial parameters (p and r) in the differential element of the Radon-kind integral. This separation is essential to perform Cormack's inversion procedure as we see in next sections.

I.2.2 Inversion formulae

Now we will establish the inversion formula in circular harmonic spaces for the \mathcal{A} -transform. As seen above the separability between the radial functions on p and r in the kernel of the forward problem is essential to make arise invariance properties of the integral over C_α and so to invert analytically \mathcal{A} .

Similarly to Cormack, the circular harmonic decomposition of such an integral makes appear Chebyshev polynomials. The inversion of \mathcal{A} lies then on their properties.

Proposition I.2.4. *The problem $\mathcal{A}f = g$ is invertible and the solution can be expressed using circular harmonic expansions of g and f in its unstable form as*

$$f_n(r) = \frac{\alpha r^{\alpha-1}}{\pi} h_2'(r^\alpha) \int_{h_2(r^\alpha)}^{+\infty} \frac{\cosh\left(\frac{n}{\alpha} \cosh^{-1}\left(\frac{q}{h_2(r^\alpha)}\right)\right)}{\sqrt{q^2 - h_2^2(r^\alpha)}} G_n'(q) dq \quad (\text{I.62})$$

or in its regularized form as

$$\begin{aligned} f_n(r) &= \frac{\alpha r^{\alpha-1}}{\pi} \frac{h_2'(r^\alpha)}{h_2(r^\alpha)} \int_0^{h_2(r^\alpha)} U_{n/\alpha-1} \left(\frac{q}{h_2(r^\alpha)} \right) G_n'(q) dq \\ &\quad - \frac{\alpha r^{\alpha-1}}{\pi} h_2'(r^\alpha) \int_{h_2(r^\alpha)}^{+\infty} \frac{\left(\left(\frac{q}{h_2(r^\alpha)} - \sqrt{\left(\frac{q}{h_2(r^\alpha)} \right)^2 - 1} \right) \right)^{\frac{n}{\alpha}}}{\sqrt{q^2 - h_2^2(r^\alpha)}} G_n'(q) dq \end{aligned} \quad (\text{I.63})$$

with

$$G_n(q) = \frac{(\mathcal{A}f)_n \left((h_1^{-1}(q))^{1/\alpha} \right)}{\sqrt{kq^2 + 1}}. \quad (\text{I.64})$$

Proof. We substitute $f(r, \theta)$ and $\mathcal{A}f(p, \varphi)$ by their circular harmonic expansions in eq (I.55). Considering the reflection symmetry with respect to γ , we bring down the following real form

$$(\mathcal{A}f)_n(p) = 2 \sqrt{k + \frac{1}{h_1^2(p^\alpha)}} \int_0^{\pi/2\alpha} d\gamma \cos(n\gamma) \left\{ \frac{1}{\alpha} \frac{h_2^2(r^\alpha)}{h_2'(r^\alpha)} f_n(r) \right\}_{r=(h_2^{-1}(\frac{h_1(p^\alpha)}{\cos(\alpha\gamma)}))^{1/\alpha}}. \quad (\text{I.65})$$

We pass from γ -variable to r -variable to obtain a more convenient form

$$\frac{(\mathcal{A}f)_n(p)}{\sqrt{kh_1^2(p^\alpha) + 1}} = 2 \int_a^b \frac{\cos\left(\frac{n}{\alpha} \cos^{-1}\left(\frac{h_1(p^\alpha)}{h_2(r^\alpha)}\right)\right)}{\sqrt{1 - \left(\frac{h_1(p^\alpha)}{h_2(r^\alpha)}\right)^2}} f_n(r) dr \quad (\text{I.66})$$

with $a = (h_2^{-1}(h_1(p^\alpha)))^{1/\alpha}$ and $b = (h_2^{-1}(+\infty))^{1/\alpha}$. Now we put $t = h_2(r^\alpha)$ and obtain

$$\frac{(\mathcal{A}f)_n(p)}{\sqrt{kh_1^2(p^\alpha) + 1}} = \frac{2}{\alpha} \int_{h_1(p^\alpha)}^{+\infty} \frac{T_{\frac{n}{\alpha}}\left(\frac{h_1(p^\alpha)}{t}\right)}{\sqrt{1 - \left(\frac{h_1(p^\alpha)}{t}\right)^2}} \frac{(h_2^{-1})'(t)}{(h_2^{-1}(t))^{1-1/\alpha}} f_n\left((h_2^{-1}(t))^{1/\alpha}\right) dt. \quad (\text{I.67})$$

These coefficients are closely related to those shown by Cormack. Indeed introducing new functions by

$$G_n(q) = \frac{(\mathcal{A}f)_n \left((h_1^{-1}(q))^{1/\alpha} \right)}{\sqrt{kq^2 + 1}} \quad (\text{I.68})$$

and

$$F_n(t) = \alpha^{-1} (h_2^{-1}(t))^{1/\alpha-1} (h_2^{-1})'(t) f_n\left((h_2^{-1}(t))^{1/\alpha}\right) \quad (\text{I.69})$$

we obtain

$$G_n(q) = 2 \int_q^{h_1^{-1}(+\infty)} \frac{\cos\left(\frac{n}{\alpha} \cos^{-1}\left(\frac{q}{t}\right)\right)}{\sqrt{1 - \left(\frac{q}{t}\right)^2}} F_n(t) dt \quad (\text{I.70})$$

which are the standard form in Cormack's inversion procedure. The consistency conditions is then given by

$$\int_{a_1}^{b_1} \frac{h_1(p^\alpha)^\gamma}{\sqrt{kh_1^2(p^\alpha) + 1}} (\mathcal{A}f)_n(p) dp = \int_{\mathbb{R}} q^\gamma G_n(q) dq = 0 \quad (\text{I.71})$$

for $\gamma = (n/\alpha) - 2, (n/\alpha) - 4, \dots > -1$ and $n > \alpha$. Once these consistency conditions established, the proof is completed following the Cormack procedure according to the value $h_1^{-1}(+\infty)$. \square

Remark I.2.5. *These two inversion formulae are very similar to the ones shown by Truong and Nguyen [69] and stands for their expressions in original spaces. In addition the derivation makes the consistency conditions of curves C_α appear which represents a powerful tool for expressing the orthogonality properties of these Radon transforms.*

The first inversion formula is unstable since the integrand increases exponentially. Indeed assuming that the original function is bounded, the integrand behaves as

$$\lim_{q \rightarrow +\infty} \frac{\cosh(|n| \cosh^{-1}(\frac{q}{t}))}{q \sqrt{(\frac{q}{t})^2 - 1}} \approx \lim_{u \rightarrow +\infty} 2 e^{(|n|-2)u}. \quad (\text{I.72})$$

The second one is based on the consistency conditions which is easily extended to our case and which avoids this instability.

In the next section we focus on the case $\alpha = 1$ which relates our curves to the standard Radon transform. In particular well-known "filtered back-projection" and singular value decomposition can be established for the Radon transform over this family of curves.

I.3 Singular value decomposition and filtered back-projection for \mathcal{A} defined over C_1

In this case our curves correspond to radial scalings of the straight line and so are related to the standard Radon transform for which the singular value decomposition has been established. In this section we extend the results of Cormack to our generalised Radon transform.

First we give some results for reconstruction methods in this particular case. Indeed previous relationship between $(f, \mathcal{A}f)$ and (F, G) permits to write down the generalized "filtered back-projection" for \mathcal{A} defined over C_1

Corollary I.3.1 (Filtered back-projection). *A closed form for the solution of the equation $\mathcal{A}f = g$, $g \in \mathcal{L}^2(\mathbb{H}_1, W_1)$, is given as*

$$f(r, \theta) = -\frac{h_2'(r)}{2\pi^2} \int_0^\pi p.v. \int_{-\infty}^{+\infty} \frac{\frac{d}{dq} \left(\frac{(\mathcal{A}f)(h_1^{-1}(q), \varphi)}{\sqrt{kq^2+1}} \right)}{q - h_2(r) \cos(\theta - \varphi)} dq d\varphi \quad (\text{I.73})$$

where *p.v.* stands for Cauchy principal value.

Proof. This is a consequence of Proposition I.2.4 with $\alpha = 1$ using the relation shown by Cormack with the corresponding change of variable (see eq. (I.68)). \square

Remark I.3.2. *This formula could be derived also using eq. (25) from [69] with $\alpha = 1$.*

For some functions h_1, h_2 , this last formula could make appear a negative power of $\cos \gamma$. In this case the implementation remains unstable. We propose then the following result which gives a more suited approach for implementation.

Corollary I.3.3 (Stable inversion in CHD). *A stable form for the solution of the equation $\mathcal{A}f = g$, $g \in \mathcal{L}^2(\mathbb{H}_1, W_1)$, is given in circular harmonic domain as*

$$f_n(r) = 2h_2'(r) \int_{-h_2(r)}^{h_2(r)} \left(\mathcal{H} \frac{d}{dq} g_n(q) \right) \frac{T_n(\frac{q}{h_2(r)})}{\sqrt{h_2^2(r) - q^2}} dq. \quad (\text{I.74})$$

with

$$g_n(q) = \left(\frac{(\mathcal{A}f)_n(h_1^{-1}(q))}{\sqrt{kq^2+1}} \right) \quad (\text{I.75})$$

Proof. This is a consequence of the previous corollary. Indeed we have

$$\begin{aligned}
f(r, \theta) &= -\frac{h_2'(r)}{2\pi^2} \int_0^\pi \text{p.v.} \int_{-\infty}^{+\infty} \frac{\frac{\partial}{\partial q} \left(\frac{(\mathcal{A}f)(h_1^{-1}(q), \varphi)}{\sqrt{kq^2+1}} \right)}{q - h_2(r) \cos(\theta - \varphi)} dq d\varphi \\
&= \frac{h_2'(r)}{2\pi^2} \int_0^\pi \text{p.f.} \int_{-\infty}^{+\infty} \frac{\left(\frac{(\mathcal{A}f)(h_1^{-1}(q), \varphi)}{\sqrt{kq^2+1}} \right)}{(q - h_2(r) \cos(\theta - \varphi))^2} dq d\varphi \\
&= h_2'(r) \int_0^\pi \left(\mathcal{H} \frac{\partial}{\partial q} g(q, \varphi) \right) (h_2(r) \cos(\theta - \varphi), \varphi) d\varphi .
\end{aligned} \tag{I.76}$$

We recognize in this last result the "filtered back-projection" of \mathcal{A} over C_1 . The proof is completed by expanding the last equation in circular harmonic domain and by using the parity of \mathcal{A} over C_1 . \square

Now we want to establish the singular value decomposition for \mathcal{A} over C_1 . As this transform is similar to standard Radon transform, we make the assumption that corresponding F, G can be confined in the unit disk. Keeping the same definition on C_1 , it means that f (resp. $\mathcal{A}f$) vanishes outside $[h_2^{-1}(0), h_2^{-1}(1)]$ (resp. $[h_1^{-1}(-1), h_1^{-1}(1)]$). Otherwise a normalization of the radial parameter in both spaces is required. For convenience we recall the definition of C_1 .

Definition I.3.4. *The class of curves C_1 is defined as*

$$h_1(p) = h_2(r) \cos(\theta - \varphi) \tag{I.77}$$

and $h_1 : [a_1, b_1] \rightarrow [-1, 1]$ and $h_2 : [a_2, b_2] \rightarrow [0, 1]$ are diffeomorphisms and h_2 is such that

$$r^2 \left(\frac{h_2'(r)}{h_2^2(r)} \right)^2 - \frac{1}{h_2^2(r)} = k \quad \text{and} \quad h_2'(r) \neq 0, \tag{I.78}$$

where prime denotes a derivative.

Before we have to prove the parity of our transform. It is clear that h_2 is an odd function according to its definition. However, due to the square, we can find two functions for its inverse. These functions are neither even nor odd. But one can define h_2^{-1} alternatively from both solutions in terms of the sign of r .

Lemma I.3.5. *Assuming that h_1 is an odd function, $\mathcal{A}f$ is an even function with respect to its first variable for all $f \in \mathcal{L}^2(\mathbb{H}_2, W_2)$.*

Proof.

$$\begin{aligned}
\mathcal{A}f(-p, \varphi + \pi) &= \sqrt{k + \frac{1}{h_1^2(p)}} \int_{-\pi/2}^{\pi/2} d\gamma \left\{ \frac{h_2^2(r)}{h_2'(r)} f(r, \gamma + \varphi + \pi) \right\}_{r=-h_2^{-1}\left(\frac{h_1(p)}{\cos(\gamma)}\right)} \\
&= \sqrt{k + \frac{1}{h_1^2(p)}} \int_{-\pi/2}^{\pi/2} d\gamma \left\{ \frac{h_2^2(r)}{h_2'(r)} f(r, \gamma + \varphi) \right\}_{r=h_2^{-1}\left(\frac{h_1(p)}{\cos(\gamma)}\right)} \\
&= \mathcal{A}f(p, \varphi),
\end{aligned} \tag{I.79}$$

since $f(r, \theta) = f(-r, \theta + \pi)$ and h_1, h_2, h_2^{-1} are odd. \square

Lemma I.3.6. *The set of $\left\{ v_n^m(r, \theta) = \sqrt{\frac{|n| + 2m + 1}{\pi}} h_2'(r) R_n^m(h_2(r)) e^{in\theta} \right\}$ for $n \in \mathbb{Z}$ and $m \in \mathbb{Z}^+$ forms a complete orthonormal basis set in $\mathcal{L}^2(\mathbb{H}_2, W_2)$ with*

$$W_2(r, \theta) = \frac{h_2(r)}{r \cdot h_2'(r)} . \quad (\text{I.80})$$

We can notice that the inner product is well defined since $h_2(\cdot)$ is a monotonic function on $[a_2, b_2]$ such that $h_2'(r) \neq 0$.

Proof. It follows from the orthogonality relation of radial Zernike polynomials

$$\begin{aligned} \frac{\pi}{|n| + 2m + 1} \delta_{mm'} \delta_{nn'} &= \left\langle R_n^m(r) e^{in\theta}, R_{n'}^{m'}(r) e^{in'\theta} \right\rangle_{[0,1] \times S^1} \\ &= 2\pi \delta_{nn'} \int_0^1 R_n^m(r) R_{n'}^{m'}(r) r dr \\ &= 2\pi \delta_{nn'} \int_{h_2^{-1}(0)}^{h_2^{-1}(1)} (h_2')^2(r) R_n^m(h_2(r)) R_{n'}^{m'}(h_2(r)) W_2(r, \theta) r dr . \end{aligned} \quad (\text{I.81})$$

The completeness comes naturally from the completeness of $R_n^m(r)$ on the unit disc. Let $f \in \mathcal{L}^2(\mathbb{H}_2, W_2)$,

$$\begin{aligned} \left\langle f(r, \theta), h_2'(r) R_n^m(h_2(r)) e^{in\theta} \right\rangle_{\mathbb{H}_2, W_2} = 0 &\Rightarrow \int_{h_2^{-1}(0)}^{h_2^{-1}(1)} f_n(r) h_2'(r) R_n^m(h_2(r)) W_2(r, \theta) r dr = 0 \\ &\Rightarrow \int_0^1 (h_2^{-1})'(r) f_n(h_2^{-1}(r)) R_n^m(r) r dr = 0 \\ &\Rightarrow f = 0 . \end{aligned} \quad (\text{I.82})$$

□

Lemma I.3.7. For $n \in \mathbb{Z}$ and $m \in \mathbb{Z}^+$ the set of

$\left\{ u_n^m(p, \varphi) = \sqrt{kh_1^2(p) + 1} \sin\left((|n| + 2m + 1) \cos^{-1}(h_1(p))\right) \frac{e^{in\varphi}}{\pi} \right\}$ forms a complete orthonormal basis set for even functions in $\mathcal{L}^2(\mathbb{H}_1, W_1)$ with

$$W_1(p, \varphi) = \frac{h_1'(p)}{kh_1^2(p) + 1} \cdot \frac{1}{\sqrt{1 - h_1^2(p)}} . \quad (\text{I.83})$$

Proof. It follows from the orthogonality relation of Chebyshev polynomials of second kind

$$\begin{aligned} &\left\langle u_n^m, u_{n'}^{m'} \right\rangle_{\mathbb{H}_1, W_1} \\ &= 2\pi \delta_{nn'} \int_{a_1}^{b_1} \frac{\sin\left((|n| + 2m + 1) \cos^{-1}(h_1(p))\right) \sin\left((|n'| + 2m' + 1) \cos^{-1}(h_1(p))\right)}{\sqrt{1 - h_1^2(p)}} h_1'(p) dp \\ &= 2\pi \delta_{nn'} \int_{-1}^1 \frac{\sin\left((|n| + 2m + 1) \cos^{-1}(p)\right) \sin\left((|n'| + 2m' + 1) \cos^{-1}(p)\right)}{\sqrt{1 - p^2}} dp \\ &= \pi^2 \delta_{mm'} \delta_{nn'} . \end{aligned} \quad (\text{I.84})$$

The completeness follows from the completeness of Chebyshev polynomial on $[-1, 1]$. Let $g \in \mathcal{L}^2(\mathbb{H}_1, W_1)$ an even function,

$$\begin{aligned}
& \left\langle g(p, \varphi), \sqrt{kh_1^2(p) + 1} \sin \left((|n| + 2m + 1) \cos^{-1} (h_1(p)) \right) e^{in\theta} \right\rangle_{\mathbb{H}_1, W_1} = 0 \\
& \Rightarrow \int_{a_1}^{b_1} \frac{g_n(p)}{\sqrt{kh_1^2(p) + 1}} \sin \left((|n| + 2m + 1) \cos^{-1} (h_1(p)) \right) h_1'(p) \frac{dp}{\sqrt{1 - h_1^2(p)}} = 0 \\
& \Rightarrow \int_{-1}^1 \frac{g_n(h_1^{-1}(p))}{\sqrt{kp^2 + 1}} U_{n+2m}(p) dp = 0 \quad \text{with } n \text{ even} \\
& \Rightarrow g = 0 .
\end{aligned} \tag{I.85}$$

□

Remark I.3.8. We can notice that the inner product is well defined since $h_1(\cdot)$ is a monotonic function on $[a_1, b_1]$. Furthermore, we see that the inner product is defined for $|h_1(p)| < 1$. This implies to normalize h_1 . To simplify the algebra, we consider below that h_1 is normalized (h_2 too).

Proposition I.3.9 (Singular value decomposition). *The system*

$$\begin{cases}
u_n^m(p, \varphi) &= \sqrt{kh_1^2(p) + 1} \sin \left((|n| + 2m + 1) \cos^{-1} (h_1(p)) \right) \frac{e^{in\varphi}}{\pi} , \\
v_n^m(r, \theta) &= \sqrt{\frac{|n| + 2m + 1}{\pi}} h_2'(r) R_n^m(h_2(r)) e^{in\theta} , \\
\sigma_n^m &= \sqrt{\frac{4\pi}{|n| + 2m + 1}} .
\end{cases} \tag{I.86}$$

for $n \in \mathbb{Z}$ and $m \in \mathbb{Z}^+$ gives a complete singular system of \mathcal{A} from $\mathcal{L}^2(\mathbb{H}_2, W_2) \rightarrow \mathcal{L}^2(\mathbb{H}_1, W_1)$.

Proof. We start from :

$$\frac{(\mathcal{A}f)_n(p)}{\sqrt{kh_1^2(p) + 1}} = 2 \int_{a_2}^{b_2} \frac{\cos \left(n \cos^{-1} \left(\frac{h_1(p^\alpha)}{h_2(r^\alpha)} \right) \right)}{\sqrt{1 - \left(\frac{h_1(p^\alpha)}{h_2(r^\alpha)} \right)^2}} f_n(r) dr \tag{I.87}$$

Then putting

$$f_n(r) = \sqrt{\frac{|n| + 2m + 1}{\pi}} h_2'(r) R_n^m(h_2(r)) \tag{I.88}$$

for a fixed value of m , using the result obtained for the classical Radon transform equation (I.87) becomes

$$\begin{aligned}
\frac{(\mathcal{A}f)_n(p)}{\sqrt{kh_1^2(p) + 1}} &= 2 \sqrt{\frac{|n| + 2m + 1}{\pi}} \int_{a_2}^{b_2} \frac{T_n \left(\frac{h_1(p)}{h_2(r)} \right)}{\sqrt{1 - \left(\frac{h_1(p)}{h_2(r)} \right)^2}} h_2'(r) R_n^m(h_2(r)) dr \\
&= 2 \sqrt{\frac{|n| + 2m + 1}{\pi}} \int_{h_1(p)}^1 \frac{R_n^m(t) T_n \left(\frac{h_1(p)}{t} \right)}{\sqrt{1 - \left(\frac{h_1(p)}{t} \right)^2}} dt \\
&= \sqrt{\frac{4\pi}{|n| + 2m + 1}} \sin \left((|n| + 2m + 1) \cos^{-1} (h_1(p)) \right) .
\end{aligned} \tag{I.89}$$

Lemmas I.3.5, I.3.6 and I.3.7 complete the proof.

□

Once the singular value decomposition established, the following corollary can be deduced for the reconstruction way of the \mathcal{A} -problem by Chebyshev/Zernike expansions.

Corollary I.3.10 (Chebyshev/Zernike expansions). *The minimum-norm solution of the equation $\mathcal{A}f = g$, $g \in \mathcal{L}^2(\mathbb{H}_1, W_1)$, is given as*

$$f(r, \theta) = \sum_n e^{in\theta} \sum_{m=0}^{\infty} a_n^m \sqrt{\frac{|n| + 2m + 1}{\pi}} h_2'(r) R_n^m(h_2(r)) , \quad (\text{I.90})$$

with

$$a_n^m = \sigma_n^{m-1} \langle \mathcal{A}f, u_n^m \rangle_{\mathbb{H}_1, W_1} . \quad (\text{I.91})$$

This solution of the equation $\mathcal{A}f = g$ is very interesting to understand the behaviour and the properties of \mathcal{A} . Indeed when we consider continuous spaces, the completeness of Zernike polynomials in Hilbert spaces implies that the null space of \mathcal{A} is reduced to $\{0\}$. However if we take only a finite number of projections, these series become sums and in this case the completeness is no more ensured on the whole studied Hilbert spaces. This makes arise a different representation of the null space of \mathcal{A} and in particular ghosts which are responsible of many artifacts in the reconstruction. One can refer to [30] for the two dimensional case and to [31] for the n dimensional case in order to understand in more details this aspect.

We advise [35, 37, 52, 54] as complementary literature concerning the singular value decomposition of Radon-kind problems.

In next section we see that this family has numerous applications in Compton scattering tomography. Previous results are then used to deduce properties and reconstruction methods for these Radon transforms. Hence, we solve the problem for the modeling and the image reconstruction associated to these modalities of Compton scattering tomography.

I.4 Some examples of curves

To solve eq (I.56), it is more convenient to use the variable $x = r^\alpha$. The new equation to solve is

$$\alpha^2 x^2 \left(\frac{h_2'(x)}{h_2^2(x)} \right)^2 - \frac{1}{h_2^2(x)} = k . \quad (\text{I.92})$$

Its solution depends on one integration constant s and is given for $|x| > 0$ by

$$h_2(x) = \left\{ \frac{2sx^{1/\alpha}}{x^{2/\alpha} - ks^2}, \frac{2sx^{1/\alpha}}{1 - ks^2x^{2/\alpha}} \right\} . \quad (\text{I.93})$$

If we are interested in the special case $\alpha = 1$, we can deduce four well-known curves. With the first solution of the differential equation and with $h_1(p) = p^{-1}$, we have thus

- for $k = 0$ and $s = 0.5$, the circle passing through O (see Fig. I.5(b)),

and with the second solution of the differential equation and with $h_1(p) = p$, we have thus

- for $k = 0$ and $s = 0.5$, the straight line (see Figure I.5(a)),
- for $k = 1$ and $s = R^{-1}$, the circular arc having a chord of fixed length rotating around its center (see Fig. I.5(c)).
- for $k = -1$ and $s = R^{-1}$, the circular arc orthogonal to a circle centered at the coordinate origin and of fixed radius (see Fig. I.5(d)).

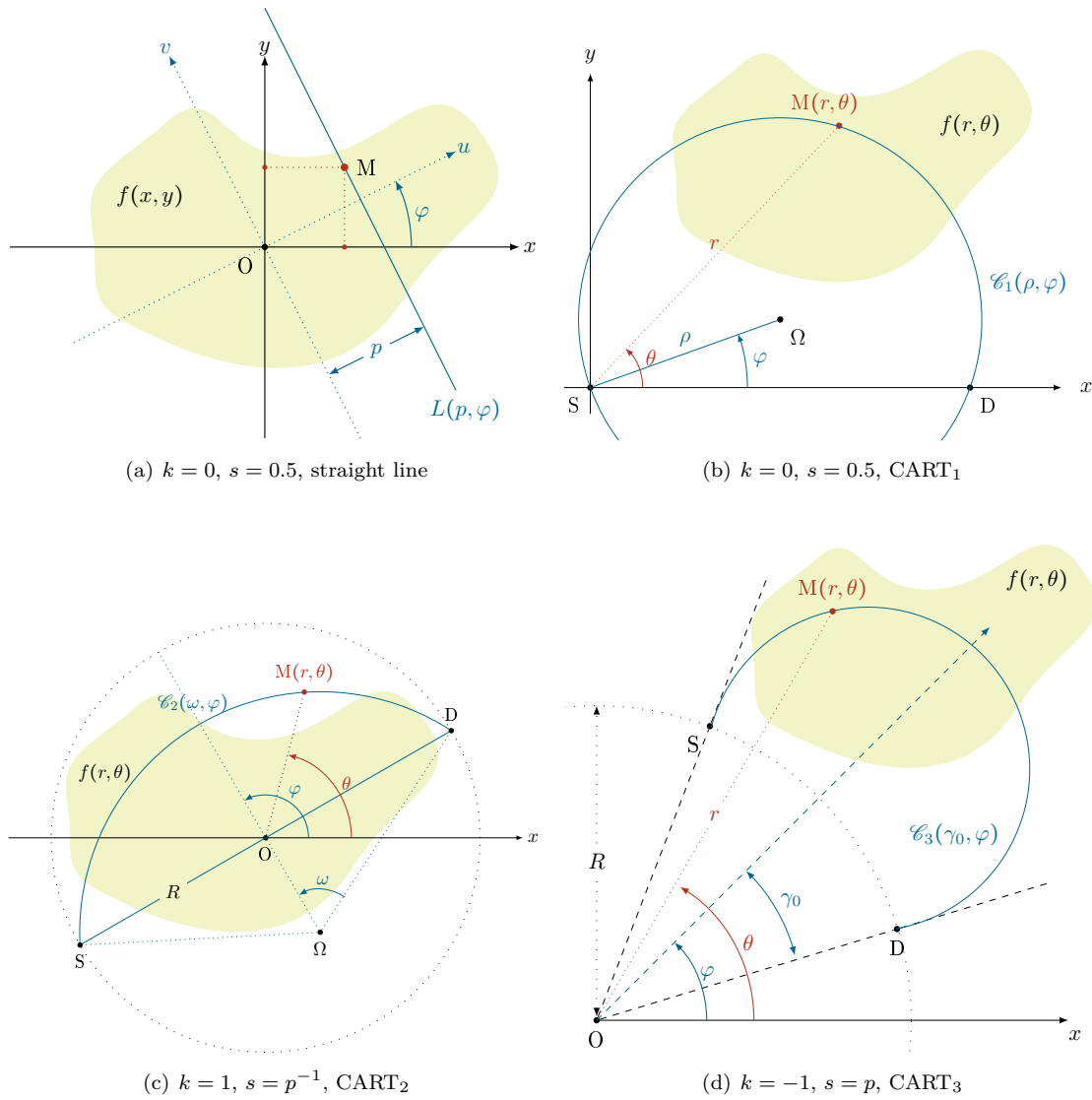


Figure I.5: Representations of particular $\alpha = 1$ solutions

I.5 Conclusion

We have established inversion formulae for the class C_α as well as the singular value decomposition and the well-known filtered back-projection for C_1 . In the examples given above, the first case and the last two cases give Radon transform over corresponding circular arcs. For convenience, we call them circular-arc Radon transforms, $\text{CART}_{1,2,3}$. In next chapter, we see how these last Radon transforms can have many applications in Compton scattering tomography.

We can notice that in the Cormack's family, the case $\alpha = 1/2$ corresponds to a class of paraboloid. This support can be used in seismic exploration for instance. Thus it appears that the class $C_{1/2}$ could be useful in future applications in seismic imaging.

The main result of this Chapter lies on the singular value decomposition of \mathcal{A} . As mentioned above it ensures the injectivity of \mathcal{A} on the orthogonal of its null space and even gives a representation of its null space. When we consider a finite number of projections and a required regularization step, it could be relevant to study the optimal sampling to choose in presence of noise and also the good truncation degree to perform. In [44, 46] an exhaustive overview is proposed.

In a different way approximate inversions could be established to provide some relevant solutions to regularization problems, see [32].

Applications in Compton scattering tomography

The concept of non-invasive imaging techniques is based on the interaction between an object (human being, materials, ...) and a physical or chemical vector (electromagnetic wave, ultrasound, magnetic field, biological ligand) so as to study the structure or the internal functioning of this object. Ionising radiation imaging makes use of photons with an energy enough high such that a part of the emitting radiation can go through the studied object: X and Gamma rays. Imaging techniques by transmission use information obtained from the interaction between ionising radiation and matter and so give some structure features of the object. While those by emission use the information obtained from the positioning and the activity of radiating sources existing or injected within the studied object. In conventional tomography, primary radiation is used as an imaging agent while the rest of the emitting radiation brings no information and even can induce an important noise in the measurement. This last part which represents a disturbing obstacle in conventional tomography could be used as imaging agent in an alternative kind of tomography: Compton scattering tomography. In the last decades some modalities of Compton scattering tomography have been proposed to recover alternative structure features about the object. Using Chapter I, we establish inversion formulae and show several properties for the Radon transforms associated to these new modalities of Compton scattering tomography. Thus, from the study of generalized Radon transforms, new applications in Compton scattering tomography arise and this chapter proposes to solve by many ways image reconstruction in those modalities.

First we present the basis of conventional and Compton scattering tomography through a review of interactions ionising radiation/matter and of the standard modalities and through the motivations behind the Compton scattering tomography. Then sections 2,3 and 4 focus on the modeling and the image reconstruction for three modalities in Compton scattering tomography : $CART_{1,2,3}$. Simulation results are finally given and show the strong interest in this theoretical study.

II.1 Basis of conventional and Compton scattering tomographies

The purpose of this part is to describe interactions between ionising radiation and matter. To understand how to use ionising radiation in imaging, it is important to be aware of implied physical phenomenon and of their corresponding modeling when a photon flux travels through an object under study. Then we present a state-of-the-art of existing techniques used in the field of imaging and give the interest which could bring modalities in Compton scattering tomography as an alternative way to study the structure of a given medium.

II.1.1 Ionising radiation : interactions with matter

II.1.1.a Origins of electromagnetic radiation

Electromagnetic radiation is a straight energy transfer at the speed $3 \times 10^8 \text{m.s}^{-1}$ in the void. When it goes through a medium, its speed decreases and its trajectory can be changed by interactions with the matter. The radiation can be subjected to an absorption or to a scattering.

Wave length (λ), frequency (ν) and energy (E) permit to differentiate different kinds of electromagnetic radiation in the electromagnetic spectrum : radio waves, microwaves, infrared, visible spectrum, ultraviolet, X-rays and Gamma rays. Each kind of electromagnetic radiation has its own properties which are used in imaging, see figure II.1. For example

- Gamma rays are used to study the distribution of radioactive markers
- X-rays permit to reconstruct the density of an object
- Visible spectrum leads to observations possible with bare eye or optical instruments
- Radio frequencies are used for transmission and reception of the signal in magnetic resonance imaging (MRI).

Two inseparable aspects describe the electromagnetic radiation : undulatory aspect and corpuscular aspect. In some cases, it behaves as a wave but in other cases it is described by a quantum called photons. Every wave (mechanical and electromagnetic) is characterized by its magnitude, its wave length, its frequency and its period. Its speed is related to its frequency and its wave length by

$$c = \lambda\nu. \quad (\text{II.1})$$

In the void its speed is constant, this is why the frequency is inversely proportional to its wave length. The energy of a photon is then given by the Planck formula

$$E = h\nu = \frac{hc}{\lambda} \quad (\text{II.2})$$

where $h = 6.62 \times 10^{-34} \text{J.s} = 4.13 \times 10^{-18} \text{keV.s}$ is the Planck constant.

In spite of its equivalence, we prefer describe radio waves by their frequency, infrared, visible spectrum and ultraviolet by their wave length and X- or Gamma rays by their energy in keV.

In the part of the spectrum larger than ultraviolet, electromagnetic radiation have enough energy to eject electrons from their atomic orbit and so produce ionised atoms and molecules. This is why radiation in this part of the spectrum is said ionising. Below this energy level it is said non ionising. The threshold of ionising energy depends on the nature of the matter. For example, water needs a minimal energy of 12.6 keV to eject electrons.

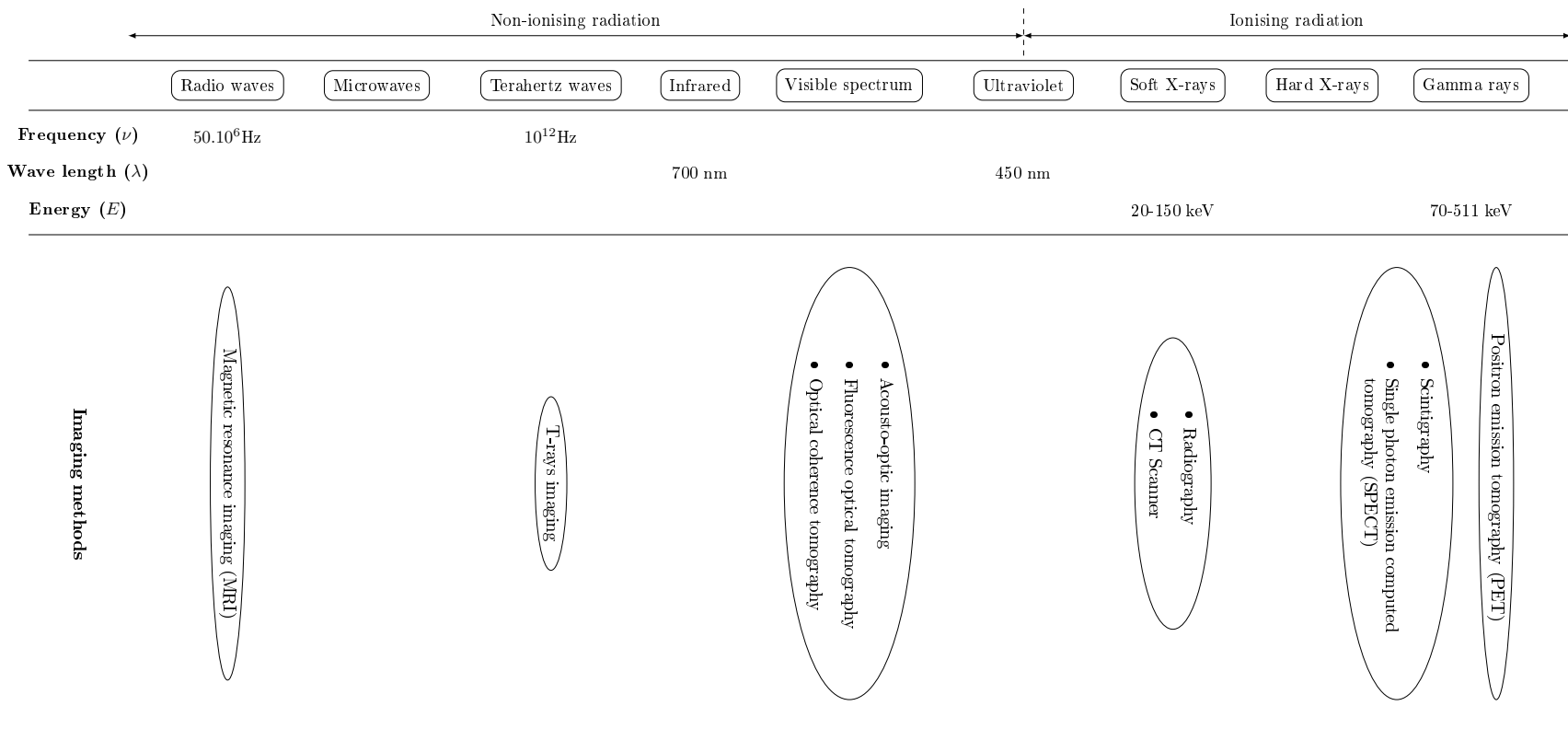


Figure II.1: Electromagnetic spectrum and non-invasive imaging methods

II.1.1.b Different kinds of interactions

A photon can interact with electrons, nuclei, or electromagnetic fields of the atomic structure. After interaction a photon can keep all its energy (elastic scattering), lose one part of it (inelastic scattering) or its entire energy (absorption) [3].

Thomson-Rayleigh scattering

- **Thomson scattering** : elastic scattering of a photon by an electron for low-energy photons which are absorbed by the electron. This latter is forced to oscillate and reemits then a photon with the same energy than the absorbed one but not necessarily in the same direction.
- **Rayleigh scattering** : When the wave length of a photon is of the same order of magnitude than the size of the atom, the photon interacts with each electrons of the reached atom. This last oscillates and emits a photon with the same energy as the incident one. Typically the lower is the incident energy, the greater is the scattering angle.

Compton scattering Compton effect stands for the collision between a photon (of energy E_0) and a free electron. The photon gives a part of its energy to the electron which starts to move with a direction of angle β with respect to the incident angle. The photon is scattered with an angle ω with respect to its incident angle and its energy after collision is given by the Compton formula [10].

$$E_\omega = \frac{E_0}{1 + \frac{E_0}{mc^2}(1 - \cos \omega)} \quad (\text{II.3})$$

where $mc^2 = 0.511$ MeV represents the energy of an electron at rest.

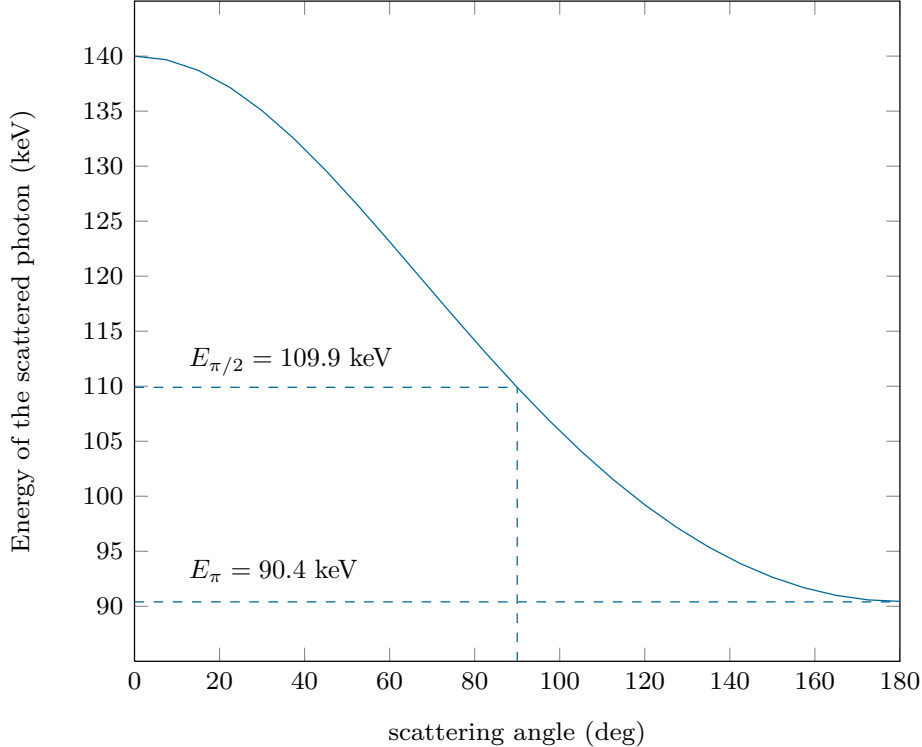


Figure II.2: Energy of a photon scattered by Compton effect with respect to the scattering angle with $E_0 = 140$ keV.

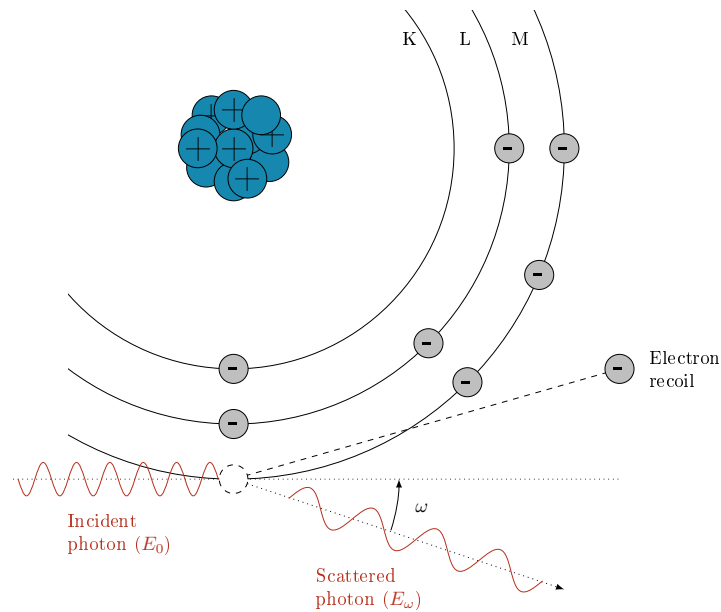


Figure II.3: Geometry of Compton scattering: the incident photon energy E_0 yields a part of its energy to an electron and is scattered with an angle ω .

Photoelectric absorption During a photoelectric effect, the photon gives its entire energy to an atomic electron. The photon is then absorbed and the electron, called photoelectron, is ejected out of the atom. This effect can take place if the energy of the incident photon is higher or equal to the binding energy. The electron goes back to the fundamental state by emission of a characteristic photon or of an Auger electron.

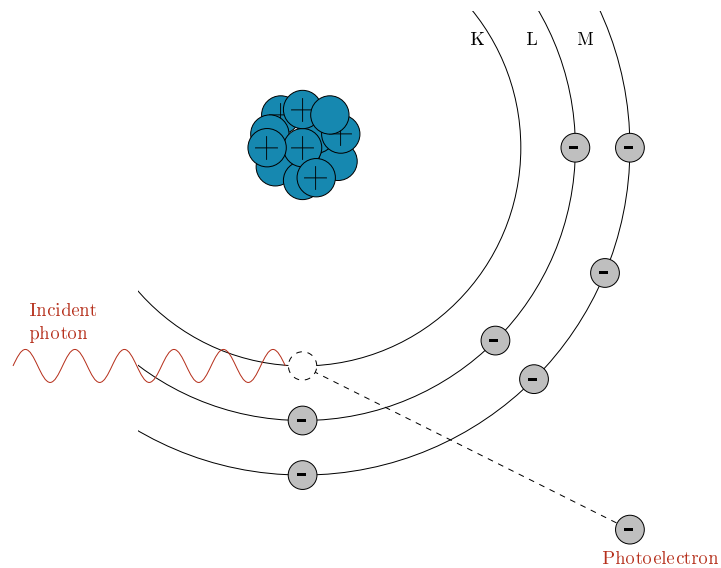


Figure II.4: Photoelectric effect: the incident photon is absorbed by the atom.

Pair production Pair production stands for the materialization of a electron-positron pair when a photon vanishes close to a nucleus or to an atomic electron. The positron is quickly slowed down by collisions and so loses its energy. Then it binds with an electron to create a positronium. This particle has a very short lifetime (10^{-10} s) and changes in two photons by annihilation. Both are emitted in opposite directions with an energy of 511 keV.

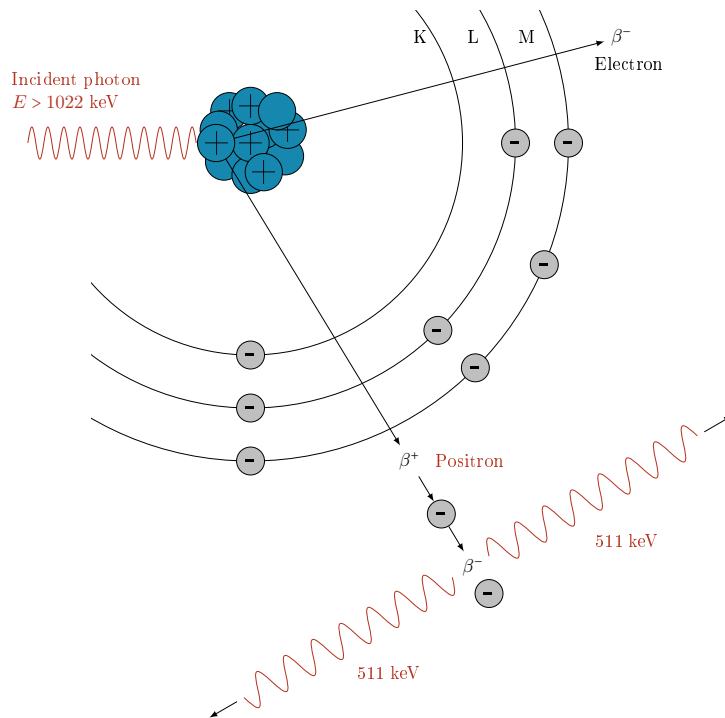


Figure II.5: Pair production: the incident photon is absorbed by the atom, the positron recombines with an electron in creating two annihilation photons of 511keV and opposite directions.

II.1.1.c Beer-Lambert law and attenuation factor

When a photon beam goes through matter, each photon can be subject to an interaction as showed previously, thus this flux is said to be attenuated. The attenuation factor describes both absorption and scattering of the photons from a macroscopic point of view. The variation of the intensity of this monochromatic photon flux while it goes through homogenous medium of width x is given by the Beer-Lambert law:

$$I = I_0 e^{-\mu x} \quad (\text{II.4})$$

where I_0 represents the incident intensity and μ stands for the linear attenuation coefficient (cm^{-1}) of the considered matter. This coefficient depends on the energy of the incident photons, of the kind and of the state of the matter. This is why tables use instead the mass attenuation factor (g.cm^{-2}) defined by the linear attenuation factor divided by the density ρ .

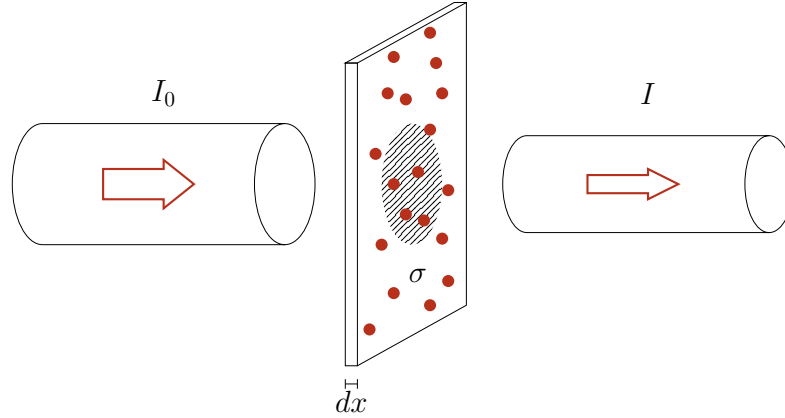


Figure II.6: Attenuation of the incident flux by all cross sections σ surrounding scattering particles in the section S of the flow.

II.1.1.d Cross section and differential cross section

Definition of the cross section The cross section σ is the imaginary surface a particle should have to ensure a given interaction between itself and a photon. Thus cross section connects the probability of an interaction at different positions, and so can be larger or smaller than the real area of the particle.

A part of the incident photon flux Φ , orthogonal to a thin thickness dx of the medium, interacts with attenuating particles of this slice. Considering n_* the number of target elements by volume units, the part $n_*\sigma dx$ of the incident photon flux will be attenuated such that

$$\frac{d\Phi}{\Phi} = -n_*\sigma dx. \quad (\text{II.5})$$

Integrating this expression on a length x , we obtain the Beer-Lambert law assuming that

$$\mu = \sigma n_*. \quad (\text{II.6})$$

For energies about a hundred keV, the incident beam has two ways to be attenuated by the medium :

- photoelectric absorption due to n_a atoms/cm³ with a cross section σ^{pe} cm²/atom,
- Compton scattering due to n_e electrons/cm³ with a cross section σ^c cm²/electron.

Assuming that each electron is free, total cross section σ^{tot} for one atom is

$$\sigma^{tot} = \sigma^{pe} + Z\sigma^c, \quad (\text{II.7})$$

with Z the atomic number. Experimentally, we find the photoelectric cross section varies is given as

$$\sigma^{pe} \approx \frac{Z^5}{(h\nu)^3}. \quad (\text{II.8})$$

From equation (II.6), we deduce the linear attenuation coefficient μ^{tot} for energies about a hundred keV

$$\mu^{tot} = \sigma^{tot}n_a = \mu^{pe} + \mu^c. \quad (\text{II.9})$$

Total cross section due to Compton effect The total cross section due to Compton effect establishes the probability a photon is subjected to a Compton scattering. In a thin slice of thickness dx we can write the probability of scattering as the ratio of the differential part of the flux which is scattered over the whole incident flux

$$\text{scattering probability} = -\frac{d\Phi}{\Phi} = n_e \sigma^c dx, \quad (\text{II.10})$$

and the number of scattered photons by volume units as

$$\frac{dN_S}{dV} = -\frac{d\Phi}{dx} = n_e \sigma^c \Phi. \quad (\text{II.11})$$

In 1928 Klein and Nishina [24] derived a formulation of this cross section thanks to a quantic approach. This relationship depends on the energy E_0 of the incident photon and can be expressed as

$$\sigma^c = \frac{3\sigma_0}{4} \left(\frac{2(1+\epsilon)^2}{\epsilon^2(1+2\epsilon)} + \frac{\ln(1+2\epsilon)}{\epsilon} \left(\frac{1}{2} - \frac{1+\epsilon}{\epsilon^2} \right) - \frac{1+3\epsilon}{(1+2\epsilon)^2} \right), \quad (\text{II.12})$$

with $\epsilon = E_0/m_e c^2$, $\sigma_0 = 8\pi r_e^2/3$ the cross section of the Thomson scattering, and $r_e = e^2/m_e c^2 = 2.818 \times 10^{-13}$ cm the classical electron radius.

Using Avogadro number N_A , the electron density can be expressed as

$$n_e = \rho N_A \frac{Z}{A}, \quad (\text{II.13})$$

where ρ is the density, Z is the number of photons, and A the number of nucleons of the atom. Their ratio is equal to 0.5 for almost all the matter. Therefore the linear attenuation coefficient due to Compton scattering is given by

$$\mu^c = n_e \sigma^c = \sigma^c \rho N_A \frac{Z}{A}. \quad (\text{II.14})$$

As we place this study in the biomedical context, we give some characteristic constants of the human body components (Tab. II.1).

Matter	n_e (cm ⁻³)	Density ρ (g.cm ⁻³)	Total cross section σ_E (cm ²)
Bone	5.91×10^{23}	1.85	4.476×10^{-25}
Water	3.34×10^{23}	1	4.491×10^{-25}
Air	3.61×10^{20}	1.2×10^{-3}	4.161×10^{-23}
Lung	9.94×10^{22}	0.3	4.497×10^{-25}

Matter	μ/ρ (cm ² .g ⁻¹ in terms of energy E (keV))					
	90	100	110	120	130	140
Bone	0.157	0.154	0.151	0.148	0.145	0.143
Water	0.166	0.162	0.159	0.156	0.153	0.150
Air	13.83	13.5	13.25	13	12.75	12.5
Lung	0.164	0.161	0.158	0.154	0.151	0.149

Table II.1: Characteristic constants of the human body components

Klein-Nishina probability The differential cross section, $(d\sigma^c/d\Omega)_\omega$, describes the angular distribution of the Compton scattering. It is defined such that a photon is scattered of an angle ω with the incident direction in the solid angle $d\Omega$ with a probability $d\sigma^c$. The corresponding total cross section is obtained integrating over the whole space

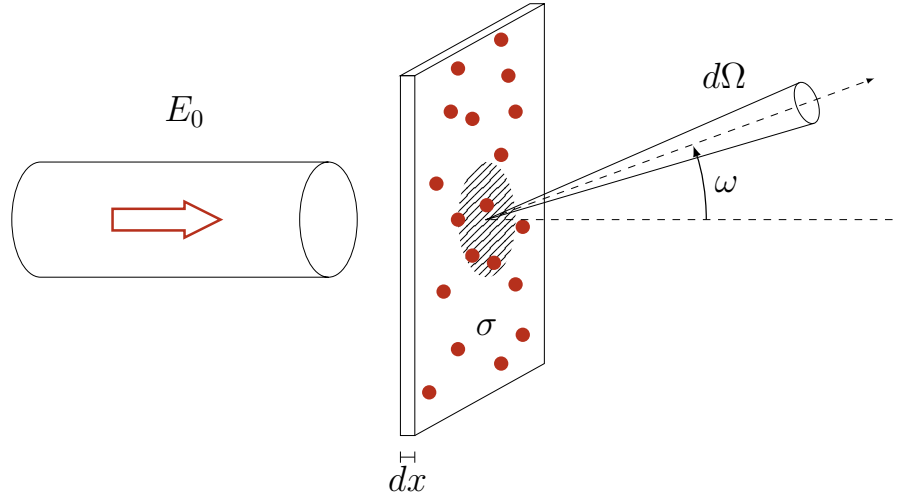


Figure II.7: Geometry of the differential cross section

$$\sigma^c = 2\pi \int_0^\pi \left(\frac{d\sigma^c}{d\Omega} \right)_\omega \sin \omega d\omega. \quad (\text{II.15})$$

The number of scattered photons from an incident flux Φ by particles in a volume dV in a direction ω is deduced from the derivation of equation (II.11)

$$\left(\frac{d^2 N_s}{dV d\Omega} \right)_\omega = \Phi n_e \left(\frac{d\sigma^c}{d\Omega} \right)_\omega. \quad (\text{II.16})$$

The differential cross section is expressed by the Klein-Nishina probability $P(\omega)$ with respect to the scattering angle ω and the incident energy E_0 [15, 24]

$$\begin{aligned} \left(\frac{d\sigma^c}{d\Omega} \right)_\omega &= r_e^2 P(\omega) \\ &= \frac{r_e^2}{2} \left(1 + \frac{\epsilon^2 (1 - \cos \omega)^2}{(1 + \cos^2 \omega)(1 + \epsilon(1 - \cos \omega))} \right) \frac{1 + \cos^2 \omega}{(1 + \epsilon(1 - \cos \omega))^2}, \end{aligned} \quad (\text{II.17})$$

with $\epsilon = E_0/m_e c^2$ and r_e the classical electron radius.

II.1.1.e Poisson emission

The phenomenon of radioactive disintegration is not homogeneous in time but follows in fact a Poisson law. Thus the number of observed disintegrations is the realization of a random variable X which follows a Poisson distribution of parameter λ_m representing the mean value of X . The probability to observe k disintegrations during a given time interval is

$$P(X = k) = e^{-\lambda_m} \frac{\lambda_m^k}{k!}. \quad (\text{II.18})$$

The Variance of X is $\sqrt{\lambda_m}$ and the relative mean error is $1/\sqrt{\lambda_m}$. Therefore the smaller is λ_m , the greater is the error.

II.1.2 Conventional tomography

In this section we detail three well-known tomographic methods in ionising radiation imaging : X-ray tomography (CT), Single photon emission computerized tomography (SPECT) and Positron

emission tomography (PET). We can divide tomographic methods in two categories : transmission and emission modality.

- Transmission modalities : akin to CT scan, the working principle of transmission modalities is to illuminate a studied object with a X- or gamma-ray source and to measure the outgoing radiation with detectors. According to the considered range of energy of the emitting source, the method of detection, etc, the measurement can have different meanings and so different modelings. Furthermore 3D imaging systems exist and propose to recover the attenuation map as a volume where the standard transmission modality in tomography (CT scan) recovers this volume slice by slice with a bidimensional approach. In the three-dimensional case, the modeling is thus given by the X-ray transform. This kind of modalities are commonly used in non destructive testing or in the biomedical field.
- Emission modalities : this kind seeks to locate and quantify ionizing radiation whose origin is located within the object. The radioactivity at the origin of the radiation may be inherently in the object (nuclear reactor, radioactive waste, nuclear weapons ...), or be injected into the bloodstream through radioisotope in the biomedical imaging case. This radionuclide attaches to an interest area (heart for example) and emits gamma rays by radioactive decay. Thus the measurement of the outgoing photon flux gives an information about the activity of the area of interest. This approach is used in SPECT scan (Single Photon Emission Computed Tomography) to reconstruct the studied volume slice by slice. Another technique is used in the PET scan (Positron Emission Tomography). Here the emitted radiation is due to the creation of a pair of positrons after injection of a radiotracer.

II.1.2.a X-ray tomography

The goal of X-ray computed tomography (CT) is to get a picture of the internal structure of an object by X-raying the object from many different directions. We focus on the 2D case, for more details about the 3D case, see Louis [33].

As X-rays travel on a line L from the X-ray source through the object to an X-ray detector. This X-ray beam is so attenuated by the material on the line L . Indeed interactions between photons and matter consist of Rayleigh scattering, Compton scattering and photoelectric absorption which take off photons of the primary radiation.

According to Beer-Lambert's law, the X-rays at a point x are attenuated proportionally to the number there, and the proportionality constant is called the linear attenuation coefficient. If the X-rays is monochromatic, then the linear attenuation coefficient is proportional to the density of the object. Let $f : \mathbb{R}^2 \rightarrow \mathbb{R}$ be the density of the object, we have according to Beer-Lamber law :

$$\ln \left(\frac{I(\text{source})}{I(\text{detector})} \right) = \int_L f(x) dl = \mathcal{R}f(L). \quad (\text{II.19})$$

This integral is exactly the classical Radon transform of f on the line L [23, 44], and since $I(\text{source})$ and $I(\text{detector})$ are measured, the line integral $\mathcal{R}f(L)$ is known.

Mathematically the goal of X-ray CT is to recover f from these measurements and so to invert the Radon transform (see Chapter I). The work of Cormack and Hounsfield showed that a discrete set of projections with a constant angular step can be inverted to recover the original function.

The architecture of CT scanners has changed a lot since its first prototype. Figure II.8 shows the fourth generation of scanner in which an annulus of detectors is placed around the object and only the X-ray source rotates around the object. This architecture leads to find a more suitable modeling of the data, the fan-beam Radon transform. Grangeat [18] thus proposed an algorithm to link the fan-beam Radon transform to the classical Radon transform and so open the way for image reconstruction with this new structure.

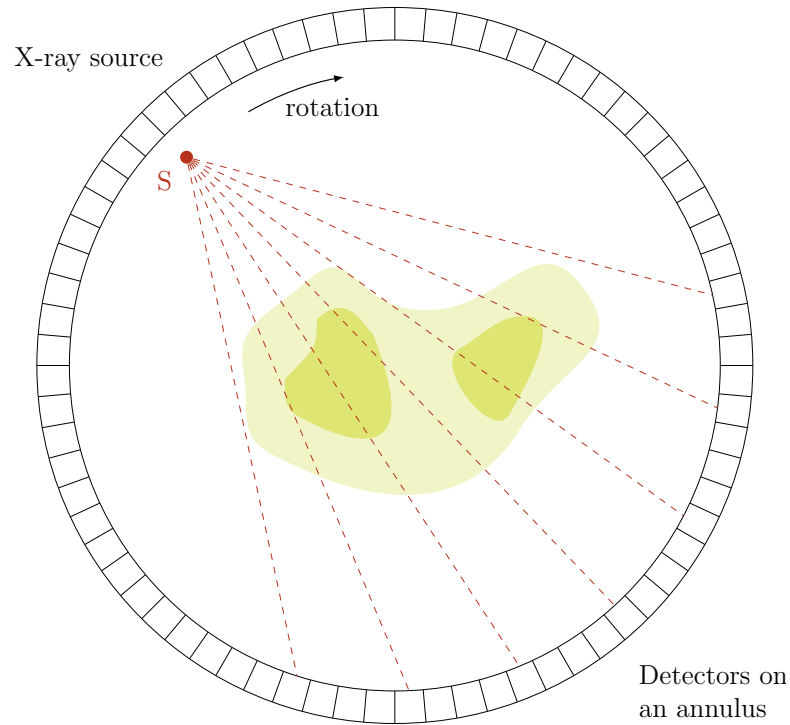
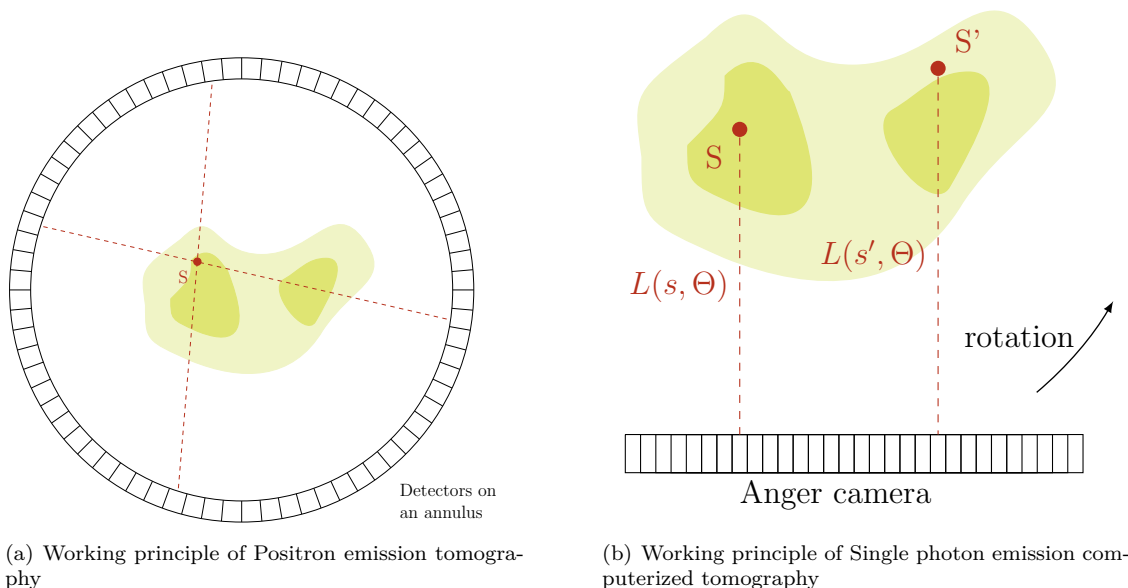


Figure II.8: Working principle of X-ray tomography

II.1.2.b Single photon emission computerized tomography

Introduced in 1963 by Kuhl and Edwards [25], the Single photon emission computerized tomography is an emission modality. In this one, one searches for reconstructing the distribution of radioactive tracers which emit monoenergetic gamma photon inside the object under study. Knowing that the emission of photons is isotropic, a collimator is placed before the detector in order to measure photons in the wanted direction. Then the camera rotates around the object to perform the set of measurements. Thus one measures the weighted sum of every radioactive contributions along the straight line from the emitting point to the camera following the direction given by the collimator. The weighted factor is expressed by the distribution of the attenuation map along the travelling line. We can notice that the attenuation factor which is the basis of the imaging by transmission becomes here a harmful parameter. The transformation which links the emission distribution weighted by the attenuation distribution to the attenuated integral projections measured by the camera is called attenuated X-ray transform (see Chapter I).

The image quality of reconstruction depends first on the quality of the measurements. However measurements obtained by Anger cameras have a very low sensitivity. The first reason is the attenuation effect since 80% of emitted photons are either scattered or absorbed. The second reason is the presence of the collimator which harms data : letting not wanted photons be detected and scattering some photons instead of absorbed them (because of its material). Moreover the collimator can stop a significative part of photons which are supposed to be detected. To this inherent defaults, we can add the mechanical filtering of the collimator which detect scattered photons with the good incident direction to the camera. These last photons lead to important errors in the reconstruction. Currently an energetic filtering and an iterative correction algorithm are used to eliminate those photons.



(a) Working principle of Positron emission tomography

(b) Working principle of Single photon emission computerized tomography

II.1.2.c Positron emission tomography

Based on the work of Ter-Pogossian [65], PET-scan is the most recent imaging technique. It is an emission modality but contrary to SPECT, the marker emits positrons. After having released its kinetic energy on a short way, a positron disintegrates with an electron emitting two photons of energy 511 keV in opposite directions. They are detected by two detectors placed at the opposite of each other. When a coincidence is detected, the system determines the path of the detected photons called line of response. Therefore, the detection is no longer mechanical but electrical which increases the sensitivity of the detector. Nowadays advances in technology on crystals and on electronic lead to estimate the emission area through the difference between time-travel of both photons. Thus we don't need to rotate around the object to reconstruct its activity distribution, we just need enough lines. PET-scan has a better resolution than SPECT-scan but this system remains expensive and needs radiotracers produced by a close cyclotron. For this reason it is used essentially in medical research field.

II.1.3 Motivations behind Compton scattering tomography (CST)

II.1.3.a Degrations due to Compton effect

In conventional imaging Compton effect harms importantly to image quality obtained by the detector (Gamma camera for example). On the first hand, Compton scattering is involved in the attenuation of the incident flux since it is responsible of the loss of photons for primary radiation. On the other hand, Compton scattering can induce bad detections which leads to the delocalization issue. Thus the scattered radiation appears like a blur decreasing image contrast and responsible of some diagnostic errors.

To solve the Compton effect issue remains a technological and mathematical challenge in Gamma imaging¹. Until now existing methods consider scattered radiation like a noise and therefore look for eliminate it from the measurement, see Fig. II.9.

Works carried out in order to improve conventional Gamma imaging brought three observations:

¹In X-ray imaging, energy is less large and so Rayleigh scattering can be the main interaction before Compton scattering.

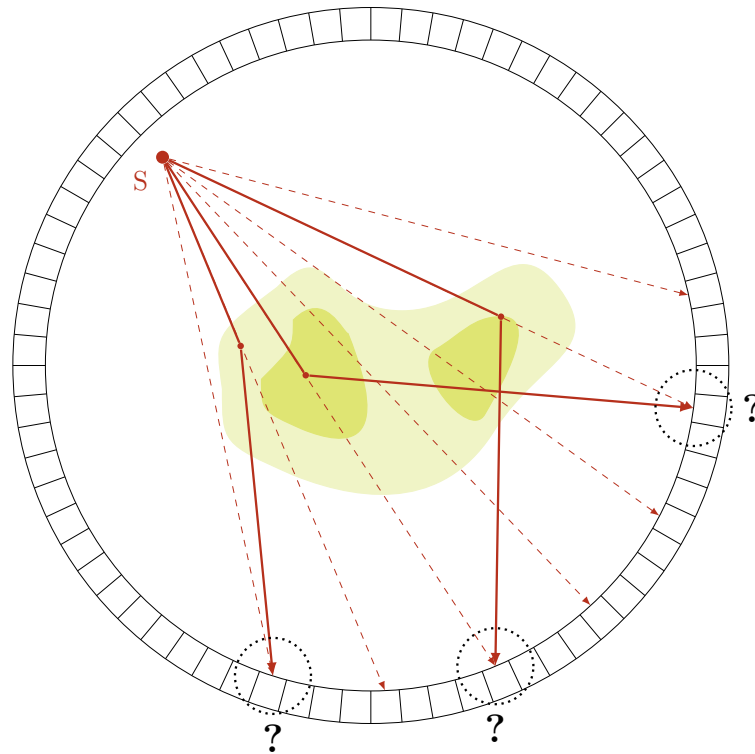


Figure II.9: Wrong detections in CT-scan due to Compton scattering.

- **Sensitivity and image quality are very low.** Scattered radiation is separated from primary radiation either by subtraction or by energetic filtering centered at the incident energy (photopic). Nevertheless the image which is made up of gamma ray without Compton collision and reaching the detector alongside of the collimator represents only 10^{-4} from the whole emitted radiation. In spite of a good consistency with expected image formation, this data are noisy because of the statistical variance, detection noise, scattering photons due to collimator, Thus its improvement appears necessary and numerous image post-processing methods were proposed in this case.
- **Signal to noise ratio is very low.** Until now it is not possible to separate perfectly scattered and primary radiations: 30 to 40% of the detected radiation was scattered. Then 70 to 80% of the incident radiation is rejected by energetical filtering. This point is particularly harmful in medical imaging where low dose are used.
- **Scattered radiation can be used as imaging agent.** The study of Compton effect led to the Compton formula which links energy and scattering angle. In next section, we will see how this relation can permit the modeling of this phenomenon with a circular geometry.

II.1.3.b Exploiting of scattered radiation

The scattering phenomenon is specific to waves and radiation. It is both a cause of disturbance and degradation, but it can also be usefully exploited for image reconstruction as can be seen in a wide range of frequencies.

In the field of visible optics, properties of propagation of the light through a scattering medium are used for the detection at distance in the upper atmospheres terrestrial era (Remote sensing), the study of stellar dust, monitoring of industrial production, medical diagnosis, The high resolution optical imaging LIDAR (laser imaging Version radar, Light Detection and Ranging) is

strongly affected by the atmosphere. In wave phenomena, one can extract information about a system by observing the scattered radiation in all directions during a broadcast. A method of detection and use of LIDAR optical scattered radiation was proposed and shown feasible [6].

In the field of ionizing radiation, several exploitations of Gamma radiation appeared in different areas. In medical imaging the tract of H.H. Barrett and W. Swindel devotes an entire chapter (Chapter 11 in [3]) at the study of scattered radiation. These authors affirmed that the detection of scattered photons does not provide useful information to image formation. On the contrary it decreases contrast and increases the noise in the measurement. But shortly afterwards methods with automatic detection of the contour of a convex object have been developed from the exploitation of projections of the object in the range of Compton effect [36, 71, 73]. And more recently, Compton scattering were used to differentiate normal and diseased tissues in oncology [58].

In non-destructive testing, imaging modalities called "Compton radiography" appeared in the 60's and continue to be studied. These methods provide the distribution of the Compton cross section which is proportional to the electron density. This map coupled with the attenuation map obtained by conventional X-ray radiography, can improve the characterization of the studied object.

In high energetic gamma-ray astronomy Compton scattering is used to study supernovae which produce gamma radiation. These very energetic gamma rays produce by Compton effect relativistic electrons during their travel in the atmosphere. Instead of directly detect them, ultrasensitive cameras record the light emitted by Cherenkov radiation of these electrons.

In Gamma imaging, Compton camera uses the principle of collimation: the primary radiation goes through a planar scattering layer and undergoes Compton scattering before being detected by a conventional gamma detector. Currently, only Compton telescopes (Comptel) uses this principle [61].

II.1.3.c Concept of Compton scattering tomography modalities

The scattered gamma radiation is used in different non-invasive imaging applications. The main idea is to model the process of Compton scattering inside the object in order to follow the path of photons and so deduce information about internal properties of the object.

In imaging modalities by emission, the gathering of information contained in the images of scattered radiation taken for different energies permit to restore the scintigraphic images used in conventional tomography. The signal to noise ratio is strongly increased, and the source delocalisation issue is decreased. Another very interesting obtained result is that these measurements can be used to reconstruct the object in 3D. The analytical inversion was proved through the compounded conical Radon transform [48]. Thus data from scattered radiation can be used to strengthen image reconstruction in conventional imaging, but they can also constitute underlying images for a novel three-dimensional imaging. This implies important advances in technology of detectors because the spatial resolution of the image reconstruction depends now on the energetic resolution of detectors.

In imaging modalities by transmission, the Compton scattered radiation allows to identify an object through its electron density. This is due to the physics of Compton effect. An ionising source² irradiates the studied medium and a detector with high energy resolution will catch and collect photons with respect to their energy E_ω (see eq. (II.3)). Then assuming that detected photons have suffered only one scattering, modeling of measurement will be possible according to certain configurations of the pair source/detector. The advantage of this concept is to rule the problem of noise in the measurement due to first-order scatter since this last is directly used as an imaging agent. Moreover in non destructive testing the electron density map brings a more relevant information about the matter than the attenuation map.

However multiple scatters will remain as a noise for this kind of modality and so collimation and/or filtering could be applied to reduce it.

²Gamma source, more than X-ray source, in order to increase the dominance of Compton effect over Rayleigh scattering. However with a suited detection and post-processing, the modeling of CST modalities is possible for the energy range of X-rays.

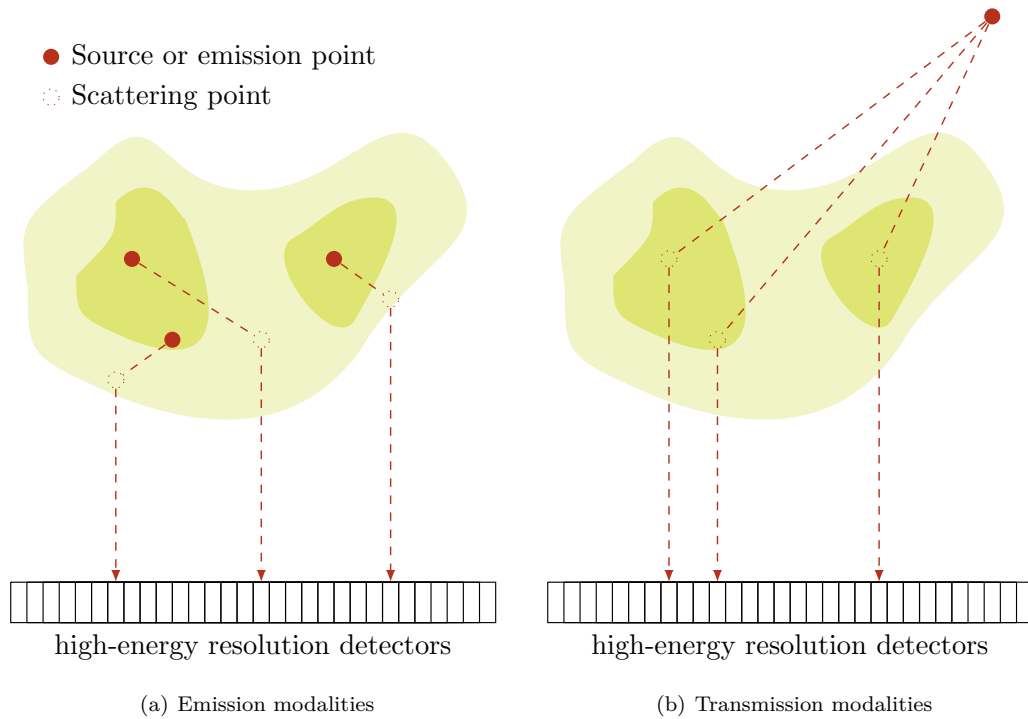


Figure II.10: Working principle of modalities on Compton scattering tomography

In the following sections, we introduce three modalities in CST and solve the image reconstruction problem using results of Chapter I. Nevertheless the attenuation factor is not taken into account. We see in Chapter III this factor has to be corrected (while analytical inversion formulae are not showed for the associated attenuated Radon transforms) and propose there a suited correction algorithm.

II.2 CST modality based on CART₁

II.2.1 Working principle

In 1994, S.J. Norton worked out a CST modality which is based on a Radon transform on circles having a fixed common point [49]. We consider a Gamma-ray of known energy emitted into an object from a point source \mathbf{S} , Compton scattered once, and detected at a point \mathbf{D} located outside the object. To an excellent approximation, the energy loss suffered by the photon upon scattering is a function only of the scattering angle ϖ subtended by the points \mathbf{S} and \mathbf{D} . Assuming the scattering is confined to a plane, the locus of scattering points having the same emitting point \mathbf{S} , detecting point \mathbf{D} , and scattering angle ϖ - or equivalently, recorded energy E_{ϖ} (cf. Compton formula eq. (II.3)) - can be shown to be a circle whose center and radius are uniquely determined by the three parameters \mathbf{S}, \mathbf{D} and ϖ (or energy $E_{\pi-\varpi}$) as illustrated in Figure II.11. Thus, when point \mathbf{S} is an omnidirectional source of Gamma-rays, the number of Compton scattered photons recorded at \mathbf{D} with a given energy $E_{\pi-\varpi}$ is a weighted line integral of the electron density, $n_e(r, \theta)$, over this circular path.

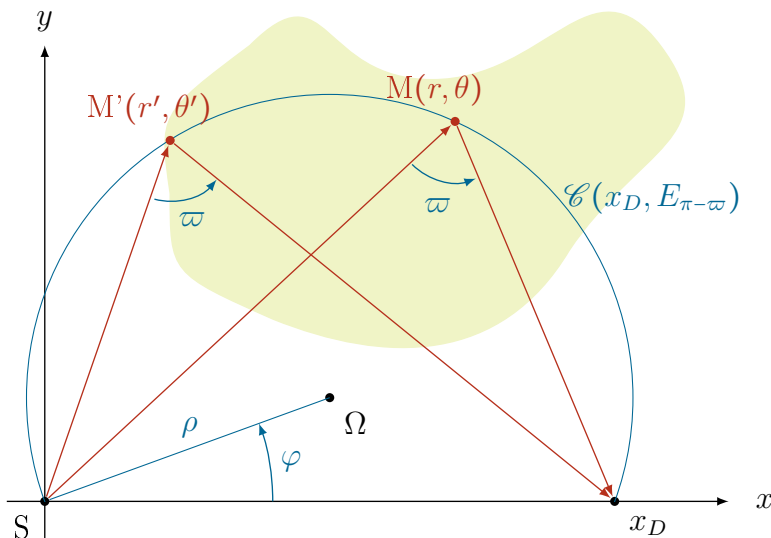


Figure II.11: Representation of the Norton's modality

We assume the detector to be located at the x coordinate x_D and to record Compton scattered photons. Let the number of photons recorded at detector coordinate x_D , of energy $E_{\pi-\varpi}$, be given by $I(x_D, E_{\pi-\varpi})$. This function can be expressed as a weighted line integral of the electron density in the upper half plane around the scattering circle identified by the parameters $(x_D, E_{\pi-\varpi})$. Then a measurement $I(x_D, E_{\pi-\varpi})$ is related to the electron density, $n_e(r, \theta)$, by

$$I(x_D, E_{\pi-\varpi}) = \int_{(r,\theta) \in \mathcal{C}(x_D, E_{\pi-\varpi})} n_e(r, \theta) w(r, \theta; x_D, E_{\pi-\varpi}) dl, \quad (\text{II.20})$$

where $\mathcal{C}(x_D, E_{\pi-\varpi})$ is the scattering circle, dl is an element of path length around the circle, and $w(r, \theta; x_D, E_{\pi-\varpi})$ is a weighted function to be taken into account

- the angular dependance of a (possibly) anisotropic source,
- the dependance of the differential cross-section (Klein-Nishina formula, see eq. (II.17)) on the scattering angle $(\pi - \varpi)$,

- the variation in solid angle subtended by a finite-sized detector from the scattering point.

The scattering circle that passes through the source point ($x = 0$) and detector point ($x = x_D$) is given in polar coordinate by

$$r = 2\rho \cos(\theta - \varphi), \quad (\text{II.21})$$

where $\varphi = \pi/2 - \varpi$ and ρ is the radius of the scattering circle given by

$$\rho = \frac{x_D}{2 \cos \varphi}, \quad -\pi/2 \leq \varphi \leq \pi/2. \quad (\text{II.22})$$

As the variables x_D and $E_{\pi-\varpi}$ are related to ρ and φ , we find it more convenient to use the variables (ρ, φ) . Figure II.12 shows the scanning of the scattering medium for two different positions of the detector (x_{D1} and x_{D2}) and varying the scattering angle $\pi - \varpi$.

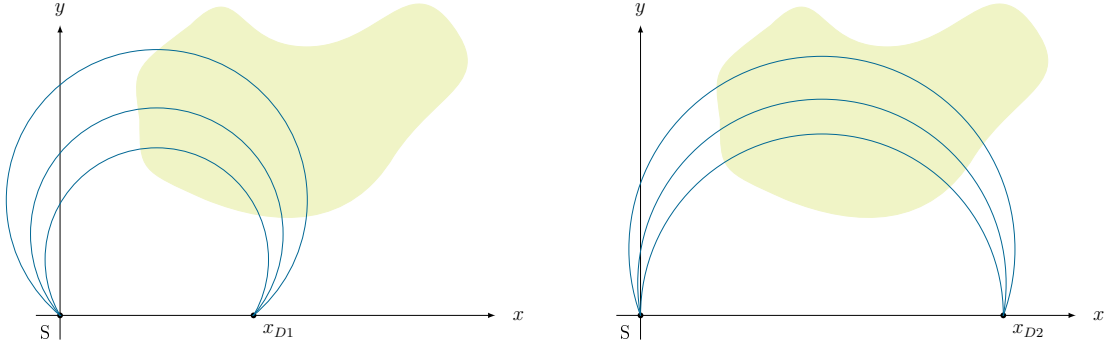


Figure II.12: Scanning of the medium in CST₁

The modeling of these measurement ($I(x_D, E_{\pi-\varpi})$) is acceptable in the Gamma-rays (energy regime from 0.1 to 1 MeV) since in this case Compton scattering is by far the dominant interaction mechanism in matter. Moreover we shall neglect the multiple scattering. However the multiple-to-single scatter ratio can be arbitrarily reduced by collimating both the source and the detector to one plane. Alternatively, multiple scattering can be treated as a source of background noise, and so various pre- and post-processing schemes can be applied [53]. The main issue for the acceptance of the modeling consists in taking into account the attenuation factor. In this chapter we neglect this factor because we don't know how to analytically invert the associated transform but in Chapter III, we propose a suited correction algorithm which permits to take into account this factor.

II.2.2 Norton's inversion method

Norton gave the expression of the non-attenuated measurements I as :

$$I(\rho, \varphi) = \int_{\varphi-\pi/2}^{\varphi+\pi/2} d\theta \int_{-\infty}^{\infty} dr \, 2\rho n_e(r, \theta) w(r, \theta; \rho, \varphi) \times \delta[r - 2\rho \cos(\theta - \varphi)] , \quad (\text{II.23})$$

where $\delta(\cdot)$ is the Dirac delta function concentrated on a circular-arc of equation $r = 2\rho \cos(\theta - \varphi)$ and $w(\cdot)$ is defined by:

$$w(r, \theta; \rho, \varphi) = \frac{a r s(\theta) P(\varphi + \pi/2)}{4\pi (2\rho)^4 \sin^2 \theta} .$$

In the above equation, a represents the area of an element of detection, $s(\theta)$ expresses any angular dependance of the gamma-ray source distribution, and $P(\omega)$ (where $\omega = \pi/2 + \varphi$) is the Klein-Nishina differential cross subsection.

Mathematically, I is essentially the Radon transform of the object electron density $n_e(M)$ on arcs of circle (CART_1), when radiation attenuation and photoelectric effects on radiation propagation are neglected.

Norton gave an inversion formula :

$$n_e(r, \theta) = \frac{1}{\pi^2} \int_0^{2\pi} d\varphi \int_0^\infty d\rho \frac{I(\rho, \varphi)}{w(r, \theta; \rho, \varphi)} h[r - 2\rho \cos(\theta - \varphi)] ,$$

where

$$h(x) = \int_{-\infty}^{\infty} e^{-i\zeta x} |\zeta| d\zeta . \quad (\text{II.24})$$

Following Norton, equation (II.24) is the same convolution kernel employed in the Filtered Back-Projection algorithm used in X-ray transmission computed tomography (CT). The difference is that the Back-Projection is performed along straight lines in transmission CT, whereas here this is performed along the circles $r = 2\rho \cos(\theta - \varphi)$.

II.2.3 Definition of the CART_1 and of its adjoint

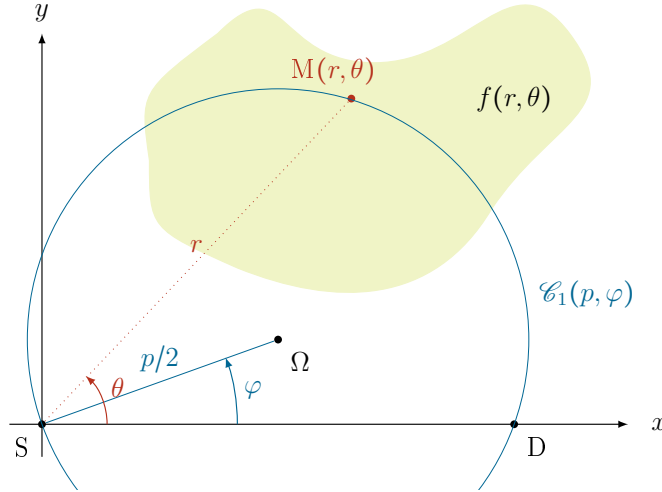


Figure II.13: Representation of the curve $\mathcal{C}_1(p, \varphi)$

Forward transform Now we consider a mathematical point of view and study the associated Radon transform (CART_1). See Figure II.13 for the parametrization. The studied circle, $\mathcal{C}_1(p, \varphi)$, is now defined by the following polar equation

$$p = \frac{r}{\cos(\theta - \varphi)} \quad (\text{II.25})$$

with p the diameter of the circle $\mathcal{C}_1(p, \varphi)$ and φ the angle between the center of the circle and the axis Sx . This equation belongs to \mathcal{C}_1 and is the special case, $h_1(p) = p^{-1}$ and $h_2(r) = r^{-1}$.

We put $\mathbb{H}_1^1 = \mathbb{R} \setminus]-1, 1[\times S^1$ and $\mathbb{H}_2^1 = [1, +\infty[\times S^1$. Following previous results shown in Chapter I, we have the following definition for CART_1 .

Definition II.2.1. The 2D Radon transform \mathcal{C}^1 of a function $f : \mathbb{H}_2^1 \rightarrow \mathbb{R}$ over curves defined by eq. (II.25) is given as

$$\mathcal{C}^1 f(p, \varphi) = p \int_{-\frac{\pi}{2}}^{\frac{\pi}{2}} f(p \cos \gamma, \gamma + \varphi) d\gamma \quad (\text{II.26})$$

with $(p, \varphi) \in \mathbb{H}_1^1$.

As we have

$$f(p \cos(\theta - \varphi), \theta) = \int_{-\infty}^{+\infty} f(r, \theta) \delta(r - p \cos(\theta - \varphi)) dr, \quad (\text{II.27})$$

equation (II.27) may be put under the form of an integral transform in $[\varphi - \frac{\pi}{2}, \varphi + \frac{\pi}{2}] \times \mathbb{R}$ with a delta function kernel concentrated on the $\mathcal{C}_1(p, \varphi)$ circles

$$\mathcal{C}^1 f(p, \varphi) = \int_{\varphi - \frac{\pi}{2}}^{\varphi + \frac{\pi}{2}} \int_{-\infty}^{+\infty} f(r, \theta) \mathcal{K}_{\mathcal{C}^1}(\rho, \varphi | r, \theta) r dr d\theta. \quad (\text{II.28})$$

with

$$\mathcal{K}_{\mathcal{C}^1}(\rho, \varphi | r, \theta) = \frac{p}{r} \delta(r - p \cos(\theta - \varphi)). \quad (\text{II.29})$$

Point spread function (PSF) For a single point object, located at (r_0, θ_0) , represented by

$$f_0(r, \theta) = \frac{1}{r} \delta(r - r_0) \delta(\theta - \theta_0),$$

the response of the CART₁ (equation (II.26)), called the Point Spread Function (PSF), is given by the equation

$$(\mathcal{C}^1 f_0)(p, \varphi) = \frac{p}{r_0} \delta(r_0 - p \cos(\theta_0 - \varphi)).$$

Thus the support of the CART₁ is the curve $p(\varphi)$ defined by

$$p(\varphi) = \frac{r_0}{\cos(\theta_0 - \varphi)}.$$

Figure II.14 shows the shape of the \cos^{-1} function which characterizes the CART₁ of the point object for $r_0 = 10$ and $\theta_0 = 0$.

Adjoint transform To express its adjoint transform, we have to rewrite the forward transform on the same support than for (r, θ)

$$\begin{aligned} \mathcal{C}^1 f(p, \varphi) &= \int_{\varphi - \frac{\pi}{2}}^{\varphi + \frac{\pi}{2}} \int_{-\infty}^{+\infty} f(r, \theta) \mathcal{K}_{\mathcal{C}^1}(\rho, \varphi | r, \theta) r dr d\theta \\ &= \int_{\varphi - \frac{\pi}{2}}^{\varphi + \frac{\pi}{2}} \int_0^{+\infty} f(r, \theta) \mathcal{K}_{\mathcal{C}^1}(\rho, \varphi | r, \theta) r dr d\theta + \int_{\varphi - \frac{\pi}{2}}^{\varphi + \frac{\pi}{2}} \int_{-\infty}^0 f(r, \theta) \mathcal{K}_{\mathcal{C}^1}(\rho, \varphi | r, \theta) r dr d\theta \\ &= \int_{\varphi - \frac{\pi}{2}}^{\varphi + \frac{\pi}{2}} \int_0^{+\infty} \left(f(r, \theta) \mathcal{K}_{\mathcal{C}^1}(\rho, \varphi | r, \theta) + f(r, \theta + \pi) \frac{p}{r} \delta(r + p \cos(\theta - \varphi)) \right) r dr d\theta \\ &= \int_{\varphi - \frac{\pi}{2}}^{\varphi + \frac{\pi}{2}} \int_0^{+\infty} f(r, \theta) \mathcal{K}_{\mathcal{C}^1}(\rho, \varphi | r, \theta) r dr d\theta + \int_{\varphi + \frac{\pi}{2}}^{\varphi + \frac{3\pi}{2}} \int_0^{+\infty} f(r, \theta) \mathcal{K}_{\mathcal{C}^1}(\rho, \varphi | r, \theta) r dr d\theta \\ &= \int_0^{2\pi} \int_0^{+\infty} f(r, \theta) \mathcal{K}_{\mathcal{C}^1}(\rho, \varphi | r, \theta) r dr d\theta. \end{aligned} \quad (\text{II.30})$$

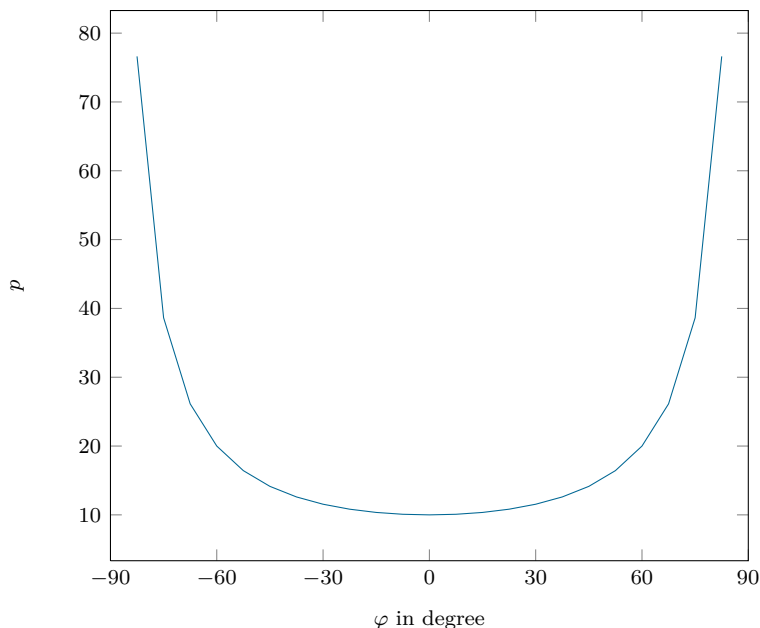


Figure II.14: Shape of the PSF for $r_0 = 10$ and $\theta_0 = 0$.

This expression is due to the equivalence between the polar representation of a function in $\mathbb{R}^+ \times [0, 2\pi[$ and in $\mathbb{R} \times [0, \pi]$.

Then the kernel $\mathcal{K}_{C^1}(\rho, \varphi | r, \theta)$ may be used to define an adjoint circular Radon transform C^{1*} . For an integrable function $g(p, \varphi)$, $C^{1*}g(r, \theta)$ is given by

$$\begin{aligned}
 C^{1*}g(r, \theta) &= \int_0^{2\pi} \int_0^{+\infty} \mathcal{K}_{C^1}(\rho, \varphi | r, \theta) g(p, \varphi) dp d\varphi \\
 &= \int_0^{2\pi} \int_0^{+\infty} \frac{p}{r} \delta(r - p \cos(\theta - \varphi)) g(p, \varphi) dp d\varphi \\
 &= \int_0^{2\pi} \frac{1}{\cos^2(\theta - \varphi)} g\left(\frac{r}{\cos(\theta - \varphi)}, \varphi\right) d\varphi
 \end{aligned} \tag{II.31}$$

We observe that the term $g\left(\frac{r}{\cos(\theta - \varphi)}, \varphi\right)$ is constant on the circle $\mathcal{C}_1(p, \varphi)$ but the factor behind does not permit us to call this operator a Back-projection operator along correspondings circles.

II.2.4 Modeling of the image formation process

For the sake of implementation it shall be useful to express image formation process and so the forward $CART_1$ in cartesian coordinates. Then data becomes

$$\int_{(x,y) \in \mathcal{C}_1(p,\varphi)} f(x,y) dl \tag{II.32}$$

with $dl = \sqrt{dx^2 + dy^2}$. The solution of $(x, y) \in \mathcal{C}_1(p, \varphi)$ is given by

$$\begin{cases} x = \frac{p}{2} \times (\cos \theta + \cos \varphi) \\ y = \frac{p}{2} \times (\sin \theta + \sin \varphi), \end{cases} \tag{II.33}$$

which implies that $dl = \frac{p}{2} d\theta$ and so that

$$\mathcal{C}^1 f(p, \varphi) = \frac{p}{2} \int_{S^1} f\left(\frac{p}{2} \times (\cos \theta + \cos \varphi), \frac{p}{2} \times (\sin \theta + \sin \varphi)\right) d\theta. \quad (\text{II.34})$$

It means that in cartesian coordinates image formation can be performed by integration of the function $f(x, y)$ over the circle of center $(p/2 \cos \varphi, p/2 \sin \varphi)$ and of radius $p/2$ with respect to the integration variable θ .

II.2.5 Associated inversion formulae

In this section, we establish and discuss different inversion approaches which can be applied for the inversion of the CART₁.

II.2.5.a Singular value decomposition

Since $h_1(p) = p^{-1}$ and $h_2(r) = r^{-1}$ we can apply Proposition I.3.9 and deduce the following result.

Corollary II.2.2. *The system*

$$\begin{cases} u_n^m(p, \varphi) &= \sin\left(\left(|n| + 2m + 1\right) \cos^{-1}\left(\frac{1}{p}\right)\right) \frac{e^{in\varphi}}{\pi}, \\ v_n^m(r, \theta) &= \sqrt{\frac{|n| + 2m + 1}{\pi}} R_n^m(1/r) \frac{e^{in\theta}}{r^2}, \\ \sigma_n^m &= \sqrt{\frac{4\pi}{|n| + 2m + 1}}. \end{cases} \quad (\text{II.35})$$

for $n \in \mathbb{Z}$ and $m \in \mathbb{Z}^+$ gives a complete singular system of \mathcal{C}^1 from $\mathcal{L}^2(\mathbb{H}_1^1, W_1)$ into $\mathcal{L}^2(\mathbb{H}_2^1, W_2)$.

This result is very important and very useful for the analysis of this transform. It gives the eigenvalues which can make easier for any frequency study or filtering in order to erase noise, And it ensures the injectivity of the CART₁ on Hilbert spaces.

A Chebyshev/Zernike expansion can naturally be given and so allows the reconstruction of a function f from the decomposition of $\mathcal{C}^1 f$ on the Chebyshev basis.

Corollary II.2.3. *The minimum-norm solution of the equation $\mathcal{C}^1 f = g$, $g \in \mathcal{L}^2(\mathbb{H}_1^1)$, is given as*

$$f_n(r) = \frac{1}{r^2} \sum_{m=0}^{\infty} (|n| + 2m + 1) a_n^m R_n^m\left(\frac{1}{r}\right), \quad (\text{II.36})$$

with

$$a_n^m = \sigma_n^{m-1} \langle \mathcal{C}^1 f, u_n^m \rangle_{\mathbb{H}_1^1, W} . \quad (\text{II.37})$$

II.2.5.b Regularized inversion formula in CHD

Proposition I.2.4 gives us the following inversion formula in circular harmonic domain for the CART₁ which was first given by Cormack [12] with $\beta = 1$.

Corollary II.2.4.

$$f_n(r) = \frac{1}{\pi r} \int_0^r \frac{e^{-|n| \cosh^{-1}(r/p)}}{\sqrt{\left(\frac{r}{p}\right)^2 - 1}} (\mathcal{C}^1 f)'_n(p) dp - \frac{1}{\pi r} \int_r^{+\infty} U_{|n|-1}(r/p) (\mathcal{C}^1 f)'_n(p) dp, \quad (\text{II.38})$$

This integral represents the regularized form of the inversion formula of the CART_1 in circular harmonic domain. It has the advantage to be stable but it is difficult to implement because of the derivative of the data. Therefore we will establish a numerical approach inspired from Chapman and Cary [8]. First a numerical approach requires finite boundaries. This is why we let a minimum value ϵ and a maximum value ρ_{max} as boundaries of the integration support. The function to recover is of course assumed to vanish outside this domain.

We let $r = \rho \cosh(\chi)$ in the first integral and $r = \rho \cos(\chi)$ in the second integral. Therefore differential elements are

$$d\rho = -r \frac{\sinh \chi}{\cosh^2 \chi} d\chi \quad \text{and} \quad d\rho = r \frac{\sin \chi}{\cos^2 \chi} d\chi \quad (\text{II.39})$$

and the change of boundaries is

$$\begin{cases} \rho = \rho_{min} & \implies \chi = \cosh^{-1}\left(\frac{r}{\rho_{min}}\right) \\ \rho = r & \implies \chi = 0 \end{cases} \quad \text{and} \quad \begin{cases} \rho = r & \implies \chi = 0 \\ \rho = \rho_{max} & \implies \chi = \cos^{-1}\left(\frac{r}{\rho_{max}}\right) \end{cases} .$$

Equation (II.38) becomes

$$f_n(r) = \frac{1}{\pi} \int_0^{\cosh^{-1}\left(\frac{r}{\rho_{min}}\right)} \frac{e^{-|n|\chi}}{\cosh^2 \chi} \mathcal{C}^1 f'_n\left(\frac{r}{\cosh \chi}\right) d\chi - \frac{1}{\pi} \int_0^{\cos^{-1}\left(\frac{r}{\rho_{max}}\right)} \frac{\sin(|n|\chi)}{\cos^2 \chi} \mathcal{C}^1 f'_n\left(\frac{r}{\cos \chi}\right) d\chi \quad (\text{II.40})$$

In order to simplify the mathematical expressions, we consider only linear interpolations, and the discretized form of f_n et $\mathcal{C}^1 f_n$ defined by

$$g_{nk} = \mathcal{C}^1 f_n(k\Delta r) \quad \text{and} \quad f_{nj} = f_n(j\Delta r) \quad (\text{II.41})$$

where $j, k \in [1, K]$ with $K = \frac{\Delta r}{\rho_{max}}$. The derivative of $\mathcal{C}^1 f_n$ can be written, in the interval $k\Delta r < p < (k+1)\Delta r$

$$g'_{nk} = \frac{g_{n(k+1)} - g_{nk}}{\Delta r} . \quad (\text{II.42})$$

As we take $\rho_{min} = \Delta r$, we obtain a discretized form of equation (II.40)

$$f_{nj} = -\frac{1}{\pi} \left[\sum_{k=1}^{j-1} g'_{nk} \left(J_n(\chi_{j(k+1)}) - J_n(\chi_{jk}) \right) + \sum_{k=j}^{K-1} g'_{nk} \left(I_n(\chi_{j(k+1)}) - I_n(\chi_{jk}) \right) \right] \quad (\text{II.43})$$

with I et J the primitive integral defined by

$$I_n(\chi_{jk}) = \int^{\chi_{jk}} \frac{\sin(|n|x)}{\cos^2 x} dx \quad (\text{II.44})$$

and

$$J_n(\chi_{jk}) = \int^{\chi_{jk}} \frac{e^{-|n|x}}{\cosh^2 x} dx . \quad (\text{II.45})$$

χ_{jk} is defined by

$$\chi_{jk} = \begin{cases} \cosh^{-1}\left(\frac{j}{k}\right) & \text{for } 1 \leq k \leq j \\ \cos^{-1}\left(\frac{j}{k}\right) & \text{for } j \leq k \leq K \end{cases} \quad (\text{II.46})$$

- $n = 0$: In this case, Tchebychev polynomial of second kind is zero and only the first sum ,

$$\begin{aligned} J_0(\chi_{jk}) &= \int^{\chi_{jk}} \frac{1}{\cosh^2 x} dx = \frac{\sinh \chi_{jk}}{\cosh \chi_{jk}} = \frac{\sqrt{\left(\frac{j}{k}\right)^2 - 1}}{\frac{j}{k}} \\ &= \sqrt{1 - \left(\frac{k}{j}\right)^2} , \end{aligned} \quad (\text{II.47})$$

remains:

$$f_{0j} = -\frac{1}{\pi} \sum_{k=1}^{j-1} g'_{0k} \left(\sqrt{1 - \left(\frac{k+1}{j}\right)^2} - \sqrt{1 - \left(\frac{k}{j}\right)^2} \right) . \quad (\text{II.48})$$

- **Computation of J_n** : Letting $u = e^x$, we have

$$J_l(\chi_{jk}) = 4 \int^{e^{\chi_{jk}}} \frac{du}{u^{|l|-1} (u^2 + 1)^2} \quad (\text{II.49})$$

or to simplify the algebra,

$$J_n(u) = \int \frac{du}{u^n (u^2 + 1)^2} . \quad (\text{II.50})$$

Now we can write $J_{n+1} + J_{n-1}$,

$$\begin{aligned} J_{n+1}(u) + J_{n-1}(u) &= \int \left(\frac{1}{u^{n+1}} + \frac{1}{u^{n-1}} \right) \frac{du}{(u^2 + 1)^2} \\ &= \int \frac{du}{u^{n+1} (u^2 + 1)} . \end{aligned} \quad (\text{II.51})$$

Making the following integration by parts

$$\begin{cases} U = \frac{1}{u^2 + 1} & U' = -\frac{2u}{(u^2 + 1)^2} \\ V' = \frac{1}{u^{n+1}} & V = -\frac{1}{nu^n} \end{cases} \quad (\text{II.52})$$

and substituting it in equation (II.51), we obtain the following recurrence relation between J_{n+1} and J_{n-1}

$$\begin{aligned} J_{n+1}(u) + J_{n-1}(u) &= -\frac{1}{nu^n (u^2 + 1)} - \frac{2}{n} \int \frac{du}{u^{n-1} (u^2 + 1)^2} \\ &= -\frac{1}{nu^n (u^2 + 1)} - \frac{2}{n} J_{n-1}(u) , \end{aligned} \quad (\text{II.53})$$

and so

$$J_{n+1}(u) = -\frac{1}{nu^n (u^2 + 1)} - \frac{n+2}{n} J_{n-1}(u) . \quad (\text{II.54})$$

According to the parity of $|n|$, the calculation of J_n is performed by recurrence with J_0 or J_1 as initial condition

$$J_0(u) = \frac{u}{2(u^2 + 1)} + \frac{1}{2} \arctan(u) \quad \text{and} \quad J_1(u) = -\frac{1}{2} \ln(u^2 + 1) + \ln(u) + \frac{1}{2(u^2 + 1)}. \quad (\text{II.55})$$

- **Computation of I_n :** We let

$$I_n(x) = \int \frac{\sin(nx)}{\cos^2 x} dx. \quad (\text{II.56})$$

We can show that,

$$\begin{aligned} I_n(x) &= \int \frac{\sin((n-2)x + 2x)}{\cos^2 x} dx \\ &= \int \frac{\sin((n-2)x) \cos(2x) + \cos((n-2)x) \sin(2x)}{\cos^2 x} dx \\ &= \int \sin((n-2)x) \frac{2 \cos^2 x - 1}{\cos^2 x} dx + 2 \int \frac{\cos((n-2)x) \sin x}{\cos x} dx \\ &= 2 \int \sin((n-2)x) dx - \underbrace{\int \frac{\sin((n-2)x)}{\cos^2 x} dx}_{I_{n-2}(x)} + 2 \int \frac{\cos((n-2)x) \sin x}{\cos x} dx \\ &= -\frac{2}{n-2} \cos((n-2)x) - I_{n-2}(x) + 2 \underbrace{\int \cos((n-2)x) \tan x dx}_A \end{aligned} \quad (\text{II.57})$$

Making the following integration by parts in A

$$\begin{cases} U = \tan x & U' = \frac{1}{\cos^2 x} \\ V' = \cos((n-2)x) & V = \frac{\sin((n-2)x)}{n-2} \end{cases}. \quad (\text{II.58})$$

we get

$$I_n(x) = -\frac{2}{n-2} \cos((n-2)x) - I_{n-2}(x) + \frac{2 \tan x}{n-2} \sin((n-2)x) - \frac{2}{n-2} \underbrace{\int \frac{\sin((n-2)x)}{\cos^2 x} dx}_{I_{n-2}(x)} \quad (\text{II.59})$$

and so we obtain a recurrence relation between I_n and I_{n-2} given by

$$I_n(x) = \frac{2}{n-2} (\tan x \sin((n-2)x) - \cos((n-2)x)) - \frac{n}{n-2} I_{n-2}(x). \quad (\text{II.60})$$

According to the parity of $|n|$, the computation of I_n is then performed by induction considering I_1 or I_2 as initial condition

$$I_1(x) = \frac{1}{\cos x} \quad \text{and} \quad I_2(x) = -2 \ln(\cos x). \quad (\text{II.61})$$

The main drawback of this approach is the calculus by induction of the integrands I_n and J_n . However if we know the discretization step, one can pre-compute this factors. In this case this method has the same complexity as a classical filtered back-projection algorithm.

II.2.5.c Filtered Back-projection and Stable inversion in circular harmonic domain

Application of the Corollary I.3.1 permits to write down the "Filtered Back-projection" formula of the CART₁.

Corollary II.2.5. *The "filtered back-projection" is given by*

$$f(r, \theta) = (-) \frac{1}{r} \int_0^\pi \left(\mathcal{H} \frac{\partial}{\partial q} g \right) \left(\frac{\cos(\theta - \varphi)}{r}, \varphi \right) d\varphi . \quad (\text{II.62})$$

with

$$g(q, \varphi) = (\mathcal{C}^1 f) (1/q, \varphi) .$$

However this last expression is numerically unstable due to the factor $1/\cos(\theta - \varphi)$. Thus an alternative and more stable form can be obtained in circular harmonic domain using Corollary I.3.3.

Corollary II.2.6 (Stable inversion in CHD).

$$f_n(r) = (-) \frac{1}{r} \int_{-1/r}^{1/r} \left(\mathcal{H} \frac{d}{dq} g_n(q) \right) \frac{T_n(qr)}{\sqrt{1 - (qr)^2}} dq \quad (\text{II.63})$$

with

$$g_n(q) = (\mathcal{C}^1 f)_n (1/q) .$$

By passing into circular harmonic domain, we have changed the stability of this integral. When $p \rightarrow r$, the integrand behaves as $1/\sqrt{x}$ for $x \rightarrow 0$ which is integrable. When $p \rightarrow +\infty$, the integrand is divergent but making the assumption that $\check{h}_n(p)$ for $p \rightarrow +\infty$ converges faster than every power of $1/|x|$ (distribution theory), the convergence is ensured.

It could be interesting to compare analytically this inversion formula to the regularised one proposed by Cormack

$$f_l(r) = \frac{1}{\pi r} \int_0^r \mathcal{C}^1 f'_l(p) \frac{(r - \sqrt{r^2 - p^2})^{|l|}}{\sqrt{r^2 - p^2}} dp - \frac{1}{\pi r} \int_r^{+\infty} \mathcal{C}^1 f'_l(q) U_{|l|-1} \left(\frac{r}{p} \right) dp , \quad (\text{II.64})$$

and to understand how the consistency condition used by Cormack to regularise his inversion formula could be interpreted in the approach proposed above.

In the regularized inversion formula showed by Cormack, the main issue is numerical since the computation of the derivative of the data leads us to compute the primitive integral of the integrand. We have showed that these primitive integrals can be deduce by induction. But the calculus of these functions grows the complexity of the reconstruction algorithm and the accuracy of numerical approximation. Finally the stable CHT inversion formula for circular Radon transform appears to be new, more stable and computationnally more efficient than the previous ones.

II.3 Novel CST modality based on CART₂

II.3.1 Working principle

This modality was first proposed by Nguyen and Truong [47]. Consider a two-dimensional object represented by a non-negative continuous function $f(\mathbf{M})$ with bounded support in \mathbb{R}^2 . An emitting point source \mathbf{S} is placed at a distance $2R$ from a point detector \mathbf{D} . We consider only the upper part of space. This is possible because an angle collimator is placed at \mathbf{D} . The segment \mathbf{SD} rotates around its middle point \mathbf{O} and its angular position is given by φ .

For a fixed rotation angle φ , the energy loss suffered by the photon upon scattering is a function only of the scattering angle ω subtended by the points \mathbf{S} and \mathbf{D} . Assuming the scattering is confined to a plane, the locus of scattering sites \mathbf{M} having the same emitting point \mathbf{S} , detecting point \mathbf{D} , and scattering angle ω can be shown to be a circular-arc, $\mathcal{C}_2(\omega, \varphi)$, whose center and radius are uniquely determined by the two parameters ω and φ as illustrated in Figure II.15. Thus, when point \mathbf{S} is an omnidirectional source of Gamma-rays, the number of Compton scattered photons recorded at \mathbf{D} with a given energy E_ω (see Compton formula eq. (II.3)) is a weighted line integral of the electron density, $n_e(r, \theta)$, over this circular-arc path.

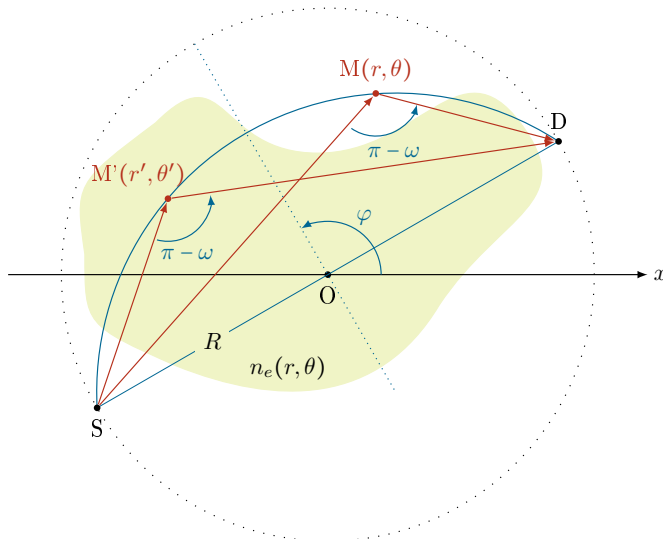


Figure II.15: Working principle

Let the number of photons recorded at \mathbf{D} , of energy E_ω , be given by $I(\omega, \varphi)$. This function can be expressed as a weighted line integral of the electron density in the upper half plane around the scattering circular arc $\mathcal{C}_2(\omega, \varphi)$. Then a measurement $I(\omega, \varphi)$ is related to the electron density, $n_e(r, \theta)$, by

$$I(\omega, \varphi) = \int_{(r, \theta) \in \mathcal{C}_2(\omega, \varphi)} n_e(r, \theta) w(r, \theta; \omega, \varphi) dl, \quad (\text{II.65})$$

where dl is an element of path length around the circular-arc, and $w(r, \theta; \omega, \varphi)$ is a weighted function in which are taken into account

- the dependance of the differential cross-section (Klein-Nishina formula, see eq. (II.17)) on the scattering angle ω ,
- the attenuation due to interactions ray/matter along the path \mathbf{SM} and \mathbf{MD} ,
- the dispersion factor due to photometric propagation effects.

The associated circular arc $\mathcal{C}_2(\omega, \varphi)$ is defined by

$$r(\theta) = R \left(\sqrt{1 + \frac{\cos^2(\theta - \varphi)}{p^2}} - \frac{\cos(\theta - \varphi)}{p} \right), \quad (\text{II.66})$$

or equivalently

$$\frac{R^2 - r^2}{2Rr} = \frac{\cos(\theta - \varphi)}{p} \quad (\text{II.67})$$

with $p = \tan \omega$.

Figure II.16 shows the scanning of the studied medium in this new CST modality at different energies E_ω or at different scattering angles ω . The set of scattering sites for given ω is an isogonal circular arc $\mathcal{C}_2(\omega, \varphi)$ passing through the pair (\mathbf{S}, \mathbf{D}) .

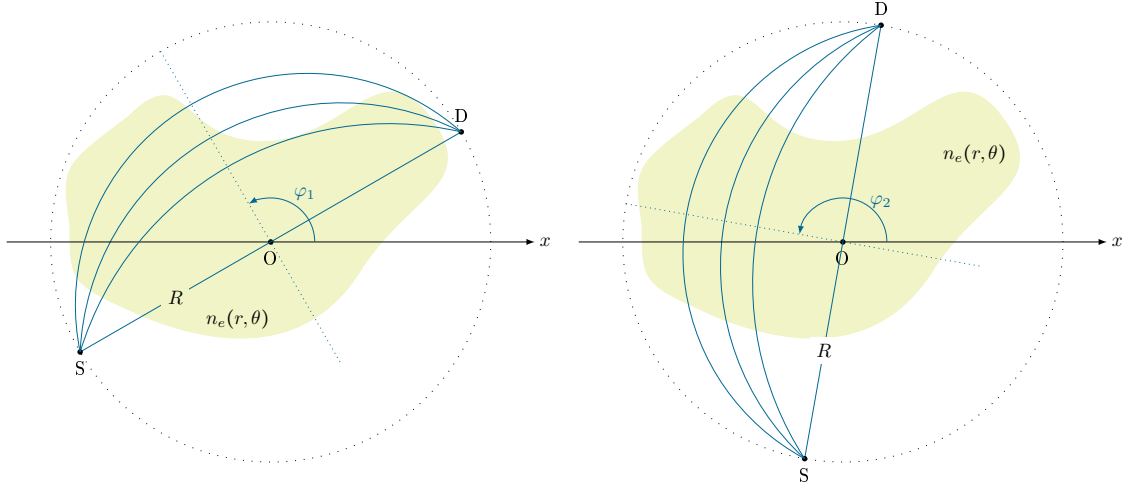


Figure II.16: Scanning of the studied object in CST_2

The modeling of this novel modality in CST leads us to study the integral of a function on a class of circular arcs (different from the one in CART_1). This is the new Radon transform defined on circular arcs called CART_2 , see [47]. However to have a good approximation of our modeling, we have to consider the same assumptions as for the CART_1 . Concerning attenuation and dispersion factors, we will take them into account in Chapter III.

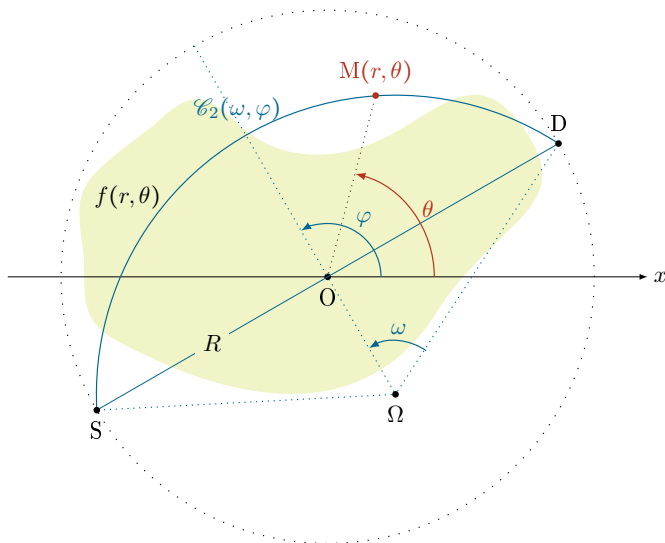
II.3.2 Definition of the CART_2 and of its adjoint

Forward transform We consider a new class of circles of radius R , which have a common chord of length $2p$ making an angle $(\varphi - \frac{\pi}{2})$ with the Ox -axis, see Figure II.17. A point of the circle with polar coordinates (r, θ) satisfies the following equation

$$r(\gamma = \theta - \varphi) = R \left(\sqrt{1 + \frac{\cos^2 \gamma}{p^2}} - \frac{\cos \gamma}{p} \right), \quad (\text{II.68})$$

with $p = \tan \omega$. Thus this curve belongs to C_1 with $h_1(p) = p$ and $h_2(r) = \frac{2Rr}{R^2 - r^2}$.

We put $\mathbb{H}_1^2 = \mathbb{R} \times S^1$ and $\mathbb{H}_2^2 = \mathbb{R}^+ \times S^1$. Following previous results shown in Chapter I, we have the following definition for CART_2 .

Figure II.17: Representation of the curve $\mathcal{C}_2(\omega, \varphi)$

Corollary II.3.1. *The 2D Radon transform \mathcal{C}^2 of a function $f : \mathbb{H}_2^2 \rightarrow \mathbb{R}$ over curves defined by eq. (II.68) is given as*

$$\mathcal{C}^2 f(\varphi, p) = \int_{-\frac{\pi}{2}}^{\frac{\pi}{2}} f(r(\gamma), \gamma + \varphi) r(\gamma) \frac{\sqrt{p^2 + 1}}{\sqrt{p^2 + \cos^2 \gamma}} d\gamma . \quad (\text{II.69})$$

with $(p, \varphi) \in \mathbb{H}_1^2$.

Thus equation (II.69) describes image formation. We can rewrite it using a delta function kernel

$$\mathcal{C}^2 f(\varphi, p) = \int_{\varphi - \frac{\pi}{2}}^{\varphi + \frac{\pi}{2}} \int_0^\infty f(r, \theta) \mathcal{K}_{\mathcal{C}^2}(\varphi, p|r, \theta) r dr d\theta . \quad (\text{II.70})$$

with

$$\mathcal{K}_{\mathcal{C}^2}(\varphi, p|r, \theta) = \frac{\sqrt{p^2 + 1}}{\sqrt{p^2 + \cos^2(\theta - \varphi)}} \delta \left(r - R \left(\sqrt{1 + \frac{\cos^2(\theta - \varphi)}{p^2}} - \frac{\cos(\theta - \varphi)}{p} \right) \right) . \quad (\text{II.71})$$

Point spread function (PSF) For a single point object, located at (r_0, θ_0) , represented by

$$f_0(r, \theta) = \frac{1}{r} \delta(r - r_0) \delta(\theta - \theta_0) ,$$

the response of the CART_2 (equation (II.69)), called the Point Spread Function (PSF), is given by the equation

$$(\mathcal{C}^2 f_0)(p, \varphi) = \frac{\sqrt{p^2 + 1}}{r_0 \sqrt{p^2 + \cos^2(\theta_0 - \varphi)}} \delta \left(r_0 - R \left(\sqrt{1 + \frac{\cos^2(\theta_0 - \varphi)}{p^2}} - \frac{\cos(\theta_0 - \varphi)}{p} \right) \right) .$$

Thus the support of the CART_2 is the curve $\omega(\varphi)$ defined by

$$\omega(\varphi) = \arctan \left(\frac{2Rr_0}{R^2 - r_0^2} \cos(\theta_0 - \varphi) \right) .$$

Figure II.18 shows the shape of the PSF which characterizes the CART_2 of the point object for $R = 10$, $r_0 = 5$ and $\theta_0 = 0$.

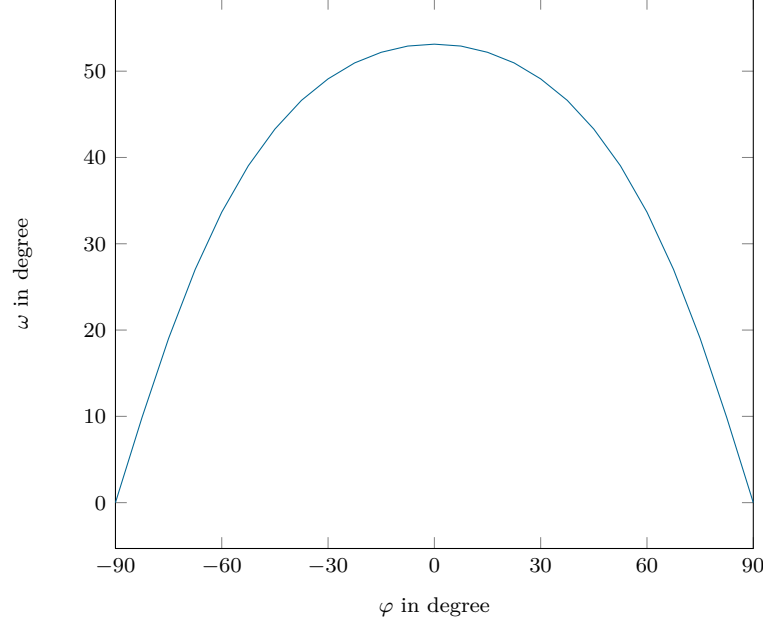


Figure II.18: Shape of the point spread function for $R = 10$, $r_0 = 5$ and $\theta_0 = 0$.

Adjoint transform The kernel $\mathcal{K}_{\text{C}^2}(\varphi, p|r, \theta)$ may be used to define an adjoint circular-arc Radon transform \mathcal{C}^{2*} . For an integrable function $g(\varphi, p)$, $\mathcal{C}^{2*}g(r, \theta)$ is given by

$$\begin{aligned} \mathcal{C}^{2*}g(r, \theta) &= \int_0^{2\pi} \int_0^\infty g(\varphi, p) \mathcal{K}_{\text{C}^2}(\varphi, p|r, \theta) d\tau d\varphi \\ &= \int_0^{2\pi} \int_0^\infty g(\varphi, p) \frac{\sqrt{p^2+1}}{\sqrt{p^2+\cos^2(\theta-\varphi)}} \delta\left(r - R\left(\sqrt{1+\frac{\cos^2(\theta-\varphi)}{p^2}} - \frac{\cos(\theta-\varphi)}{p}\right)\right) dp d\varphi. \end{aligned} \quad (\text{II.72})$$

Now we have to rewrite the kernel in terms of a p -integration by transforming the delta-function

$$\begin{aligned} \delta\left(r - R\left(\sqrt{1+\frac{\cos^2(\theta-\varphi)}{p^2}} - \frac{\cos(\theta-\varphi)}{p}\right)\right) \\ = \frac{2R \cos(\theta-\varphi)(R^2+r^2)}{(R^2-r^2)^2} \delta\left(p - \frac{2Rr}{R^2-r^2} \cos(\theta-\varphi)\right). \end{aligned} \quad (\text{II.73})$$

Finally the adjoint Radon transform becomes

$$\mathcal{C}^{2*}g(r, \theta) = \frac{2R}{R^2-r^2} \int_0^{2\pi} \sqrt{1+\frac{4R^2r^2 \cos^2(\theta-\varphi)}{(R^2-r^2)^2}} g\left(\varphi, \frac{2Rr}{R^2-r^2} \cos(\theta-\varphi)\right) d\varphi. \quad (\text{II.74})$$

The term $g\left(\varphi, \frac{2Rr}{R^2-r^2} \cos(\theta-\varphi)\right)$ is constant on the corresponding circular arc but the factor behind does not permit us to call this operator a Back-projection operator along correspondings circular-arcs.

II.3.3 Modeling of image formation process

For small values of ω ($\omega \approx 0$), the scanning of the circular-arc becomes hard. According to the sampling rate $d\theta$, we can define an angle ω_0 , below which we cannot get all the points of the circular-arc. This is why the area under the circular-arc $\mathcal{C}_2(\varphi, \omega_0)$ is "ill-observed" hence "ill-reconstructed". Numerically we can reduce this phenomenon by decreasing $d\theta$ but at the expense of the computational time.

To avoid it, we have to rewrite the image formation. Now we study a new function $h(x, y)$ which is $f(r, \theta)$ in cartesian coordinates and we consider the rotating basis centered at Ω . The scanning of the corresponding circular-arc $\mathcal{C}_2(\varphi, \omega)$ is now parametrized by $\varpi \in [\pi/2 - \omega, \pi/2 + \omega]$, see Fig. II.19.

In the fixed basis centered at O a point $M(x, y)$ of $\mathcal{C}_2(\varphi, \omega)$ can be defined by ϖ according to the following system

$$\begin{cases} x(\varpi) = \frac{R}{\sin \omega} \sin(\varpi + \varphi) - \frac{R}{\tan \omega} \cos \varphi \\ y(\varpi) = \frac{-R}{\sin \omega} \cos(\varpi + \varphi) - \frac{R}{\tan \omega} \sin \varphi . \end{cases}$$

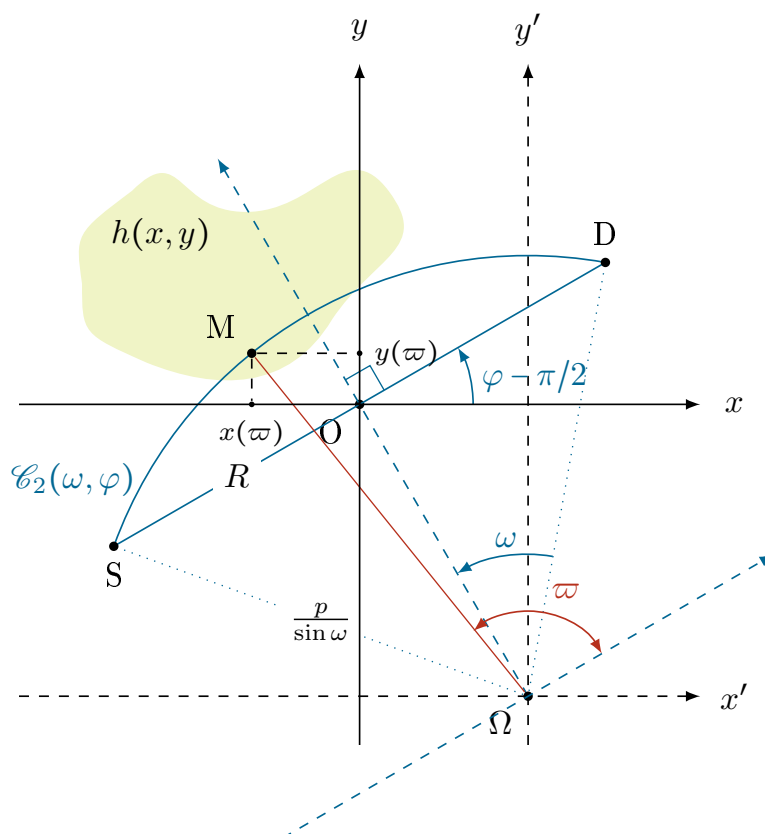


Figure II.19: Principle of CART₂ in cartesian coordinates

Considering these variables, the integral of a function $f(r, \theta)$ on circular-arcs becomes the integral of the corresponding cartesian function $h(x, y)$ on corresponding circular sector

$$\begin{aligned}
 (\mathcal{C}^2 f)(\varphi, \tau) &= \int_{-\frac{\pi}{2}}^{\frac{\pi}{2}} f(r(\gamma), \gamma + \varphi) r(\gamma) \frac{\sqrt{1 + \tau^2}}{\sqrt{1 + \tau^2 \cos^2(\gamma)}} d\gamma \\
 &= \int_{\frac{\pi}{2} - \omega}^{\frac{\pi}{2} + \omega} R \sqrt{1 + \tau^2} h(x(\varpi), y(\varpi)) d\varpi .
 \end{aligned} \tag{II.75}$$

Equation (II.75) is not suitable for inversion but is more adapted to a computation of the image formation.

II.3.4 Associated inversion formulae

In this section, we establish and discuss different inversion approaches which can be applied for the inversion of the CART₂.

II.3.4.a Singular value decomposition

Since $h_1(p) = p$ and $h_2(r) = \frac{2Rr}{R^2 - r^2}$ we can apply Proposition I.3.9 and deduce the following result considering that r and p are normalized and so are within the unit disk.

Corollary II.3.2. *The system*

$$\begin{cases}
 u_n^m(p, \varphi) &= \sqrt{p^2 + 1} \sin\left((|n| + 2m + 1) \cos^{-1}(p)\right) \frac{e^{in\varphi}}{\pi} , \\
 v_n^m(r, \theta) &= \sqrt{\frac{|n| + 2m + 1}{\pi}} \frac{2R(R^2 + r^2)}{(R^2 - r^2)^2} R_m^n \left(\frac{2Rr}{R^2 - r^2}\right) e^{in\theta} , \\
 \sigma_n^m &= \sqrt{\frac{4\pi}{|n| + 2m + 1}} .
 \end{cases} \tag{II.76}$$

for $n \in \mathbb{Z}$ and $m \in \mathbb{Z}^+$ gives a complete singular system of \mathcal{C}^2 from $\mathcal{L}^2(\mathbb{H}_1^2, W_1)$ into $\mathcal{L}^2(\mathbb{H}_2^2, W_2)$.

This result is very important and very useful for the analysis of this transform. It gives the eigenvalues which can make easier any frequency study or filtering in order to erase noise, And it ensures the injectivity of the CART₂ on Hilbert spaces.

A Chebyshev/Zernike expansion can naturally be given and so allows the reconstruction of a function f from the decomposition of $\mathcal{C}^2 f$ on the Chebyshev basis.

Corollary II.3.3. *The minimum-norm solution of the equation $\mathcal{C}^2 f = g$, $g \in \mathcal{L}^2(\mathbb{H}_1^2)$, is given as*

$$f_n(r) = \frac{2R(R^2 + r^2)}{(R^2 - r^2)^2} \sum_{m=0}^{\infty} (|n| + 2m + 1) a_n^m R_m^n \left(\frac{2Rr}{R^2 - r^2}\right) , \tag{II.77}$$

with

$$a_n^m = \sigma_n^{m-1} \langle \mathcal{C}^2 f, u_n^m \rangle_{\mathbb{H}_1^2, W} . \tag{II.78}$$

II.3.4.b Regularized inversion formula in CHD

Proposition I.2.4 gives us the following inversion formula in circular harmonic domain for the CART_2 .

Corollary II.3.4.

$$f_n(r) = (-)^{|n|} \frac{2R(R^2 + r^2)}{(R^2 - r^2)^2} \left[\frac{1}{\pi t} \int_0^t dp \frac{d}{dp} \left(\frac{(\mathcal{C}^2 f)_n(p)}{\sqrt{p^2 + 1}} \right) U_{|n|-1} \left(\frac{p}{t} \right) - \frac{1}{\pi t} \int_t^1 dp \frac{d}{dp} \left(\frac{(\mathcal{C}^2 f)_n(p)}{\sqrt{p^2 + 1}} \right) \frac{\left((p/t) - \sqrt{(p/t)^2 - 1} \right)^{|n|}}{\sqrt{(p/t)^2 - 1}} \right]_{t = \frac{2Rr}{R^2 - r^2}}. \quad (\text{II.79})$$

This integral represents the regularized form of the inversion formula of the CART_2 in circular harmonic domain. It has the advantage to be stable but it is difficult to implement because of the derivative of the data. Therefore we can follow the approach of Chapman and Cary [8] putting

$$F_n \left(t = \frac{2Rr}{R^2 - r^2} \right) = \frac{(R^2 - r^2)^2}{2R(R^2 + r^2)} f_n(r) \quad \text{and} \quad G_n(p) = \frac{(\mathcal{C}^2 f)_n(p)}{\sqrt{p^2 + 1}}. \quad (\text{II.80})$$

II.3.4.c Filtered Back-projection and Stable inversion in circular harmonic domain

Application of the Corollary I.3.1 permits to write down the "Filtered Back-projection" formula of the CART_2 .

Corollary II.3.5. *The "filtered back-projection" is given by*

$$\begin{aligned} f(r, \theta) &= \frac{R}{\pi^2} \frac{R^2 + r^2}{(R^2 - r^2)^2} \int_0^\pi p.v. \int_{-\infty}^{+\infty} \frac{\frac{\partial}{\partial p} \left(\frac{(\mathcal{C}^2 f)(p, \varphi)}{\sqrt{p^2 + 1}} \right)}{\frac{p(R^2 - r^2)}{2Rr} - \cos(\theta - \varphi)} dq d\varphi, \\ &= \frac{(R^2 + r^2)}{r(R^2 - r^2)} \int_0^\pi \left(\mathcal{H} \frac{\partial}{\partial p} \frac{\mathcal{C}^2 f(p, \varphi)}{\sqrt{p^2 + 1}} \right) \left(\frac{2Rr}{R^2 - r^2} \cos(\theta - \varphi), \varphi \right) d\varphi. \end{aligned} \quad (\text{II.81})$$

We see that the term of "filtered back-projection" is a misuse of language since this inversion formula makes appear a "weighted" adjoint operator of the CART_2 . As the filtering is of the same kind than in the classical Radon transform case, same apodization methods can be used : Hann filter, Shepp-Logan filter, And this approach has the advantage to be easily implementable with short computing time.

An alternative form can be obtained in circular harmonic domain using Corollary I.3.3.

Corollary II.3.6 (Stable inversion in CHD).

$$f_n(r) = \frac{4R(R^2 + r^2)}{(R^2 - r^2)^2} \int_{-\frac{2Rr}{R^2 - r^2}}^{\frac{2Rr}{R^2 - r^2}} \left(\mathcal{H} \frac{d}{dp} g_n(p) \right) \frac{T_n \left(\frac{p(R^2 - r^2)}{2Rr} \right)}{\sqrt{\frac{4R^2 r^2}{(R^2 - r^2)^2} - p^2}} dp \quad (\text{II.82})$$

with

$$g_n(p) = \frac{(\mathcal{C}^2 f)_n(p)}{\sqrt{p^2 + 1}}.$$

This formula has the advantage to be very simple to understand and to compute. Furthermore the filtering of the data is very flexible for the regularization such that a mollification of the kernel [32].

II.4 Novel CST modality based on CART₃

II.4.1 Working principle

This modality was first proposed by Truong and Nguyen [69]. A calibrated point source \mathbf{S} of ionizing radiation, located on a fixed circle centered at \mathbf{O} and of radius R , emits photons of definite energy E_0 . A lead shield nearby confines this emitted radiation to a half-space. An object, placed outside the circle, is irradiated by the incoming radiation. Compton scattered radiation by the object electric charges is selectively registered by a point-like detector \mathbf{D} , located on the same circle, at different scattering energies E_ω and so at different scattering energy ω . Then measurement corresponds to the contribution of a set of scattering sites on a circular arc $\mathcal{C}_3(\gamma_0, \varphi)$ defined by

$$r(\gamma) = R \left(\frac{\cos \gamma}{p} + \sqrt{\frac{\cos^2 \gamma}{p^2} - 1} \right), \quad (\text{II.83})$$

with $\gamma = \theta - \varphi$.

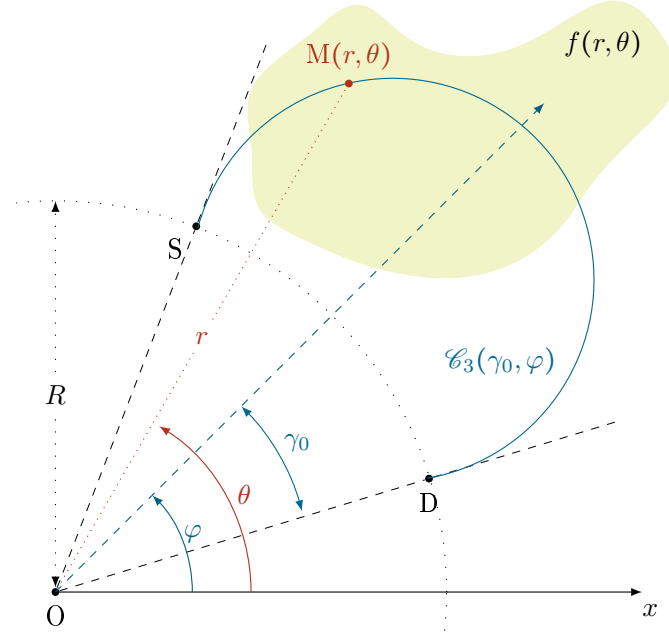


Figure II.20: Representation of the curve $\mathcal{C}_3(\gamma_0, \varphi)$

II.4.2 Defintion of the CART₃ and of its adjoint

Forward transform The circular arc $\mathcal{C}_3(\gamma_0, \varphi)$ can be equivalently expressed as

$$\frac{R^2 + r^2}{2Rr} = \frac{\cos(\theta - \varphi)}{p} \quad (\text{II.84})$$

with $p = \cos(\gamma_0) = \cos(\omega - \pi/2)$. Thus this curve belongs to C_1 with $h_1(p) = p$ and $h_2(r) = \frac{2Rr}{R^2 + r^2}$. The reality of the curve requires that $\cos^2 \gamma \geq p^2$. Defining γ_0 by the relation $\cos^2 \gamma_0 = p^2$, then the domain of existence of the curve in the angular sector $(-\gamma_0 < \gamma < \gamma_0)$, since $p \leq 1$.

We put $\mathbb{H}_1^3 = \mathbb{R} \setminus]-1, 1[\times S^1$ and $\mathbb{H}_2^3 = [1, +\infty[\times S^1$. Following previous results shown in Chapter I, we have the following definition of the CART₃.

Corollary II.4.1. *The 2D Radon transform \mathcal{C}^3 of a function $f : \mathbb{H}_2^3 \rightarrow \mathbb{R}$ over curves defined by eq. (II.25) is given as*

$$\mathcal{C}^3 f(p, \varphi) = \int_{-\gamma_0}^{\gamma_0} \sqrt{\frac{1-p^2}{\cos^2 \gamma - p^2}} r(\gamma) f(r(\gamma), \gamma + \varphi) d\gamma \quad (\text{II.85})$$

with $(p, \varphi) \in \mathbb{H}_1^3$.

As we have

$$f(r(\gamma), \theta) = \int_{-\infty}^{\infty} f(r, \theta) \delta(r - r(\gamma)) dr, \quad (\text{II.86})$$

equation (II.85) may be put under the form of an integral transform in $[\varphi - \gamma_0, \varphi + \gamma_0] \times \mathbb{R}$ with a delta function kernel concentrated on the $C(\tau, \varphi)$ circles

$$\mathcal{C}^3 f(p, \varphi) = \int_{\varphi - \gamma_0}^{\varphi + \gamma_0} \int_{-\infty}^{\infty} \mathcal{K}_{\mathcal{C}^3}(p, \varphi | r, \theta) f(r, \theta) r dr d\theta, \quad (\text{II.87})$$

with

$$\mathcal{K}_{\mathcal{C}^3}(p, \varphi | r, \theta) = \sqrt{\frac{1-p^2}{\cos^2 \gamma - p^2}} \delta \left(r - R \left(\frac{\cos \gamma}{p} + \sqrt{\frac{\cos^2 \gamma}{p^2} - 1} \right) \right). \quad (\text{II.88})$$

Point spread function (PSF) For a single point object, located at (r_0, θ_0) , represented by

$$f_0(r, \theta) = \frac{1}{r} \delta(r - r_0) \delta(\theta - \theta_0),$$

the response of the CART_3 (equation (II.85)), called the Point Spread Function (PSF), is given by the equation

$$(\mathcal{C}^3 f_0)(p, \varphi) = \frac{1}{r_0} \sqrt{\frac{1-p^2}{\cos^2(\theta_0 - \varphi) - p^2}} \delta \left(r_0 - R \left(\frac{\cos(\theta_0 - \varphi)}{p} + \sqrt{\frac{\cos^2(\theta_0 - \varphi)}{p^2} - 1} \right) \right).$$

Thus the support of the CART_3 is the curve $\omega(\varphi)$ defined by

$$\omega(\varphi) = \frac{\pi}{2} + \arccos \left(\frac{2Rr_0}{R^2 + r_0^2} \cos(\theta_0 - \varphi) \right).$$

Figure II.21 shows the shape of the PSF which characterizes the CART_3 of the point object for $R = 10$, $r_0 = 5$ and $\theta_0 = 0$.

Adjoint transform The kernel $\mathcal{K}_{\mathcal{C}^3}(p, \varphi | r, \theta)$ may be used to define an adjoint circular-arc Radon transform \mathcal{C}^{3*} . For an integrable function $g(p, \varphi)$, $\mathcal{C}^{3*}g(r, \theta)$ is given by

$$\begin{aligned} \mathcal{C}^{3*}g(r, \theta) &= \int_0^{2\pi} \int_0^1 g(p, \varphi) \mathcal{K}_{\mathcal{C}^3}(p, \varphi | r, \theta) dp d\varphi \\ &= \int_0^{2\pi} \int_0^1 g(p, \varphi) \sqrt{\frac{1-p^2}{\cos^2 \gamma - p^2}} \delta \left(r - R \left(\frac{\cos \gamma}{p} + \sqrt{\frac{\cos^2 \gamma}{p^2} - 1} \right) \right) dp d\varphi. \end{aligned} \quad (\text{II.89})$$

Now we have to rewrite the kernel in terms of a p -integration by transforming the delta-function

$$\delta \left(r - R \left(\frac{\cos \gamma}{p} + \sqrt{\frac{\cos^2 \gamma}{p^2} - 1} \right) \right) = \frac{R^2 - r^2}{R^2 + r^2} \frac{2r^2 \cos \gamma}{R} \delta \left(p - \frac{2rR}{R^2 + r^2} \cos \gamma \right). \quad (\text{II.90})$$

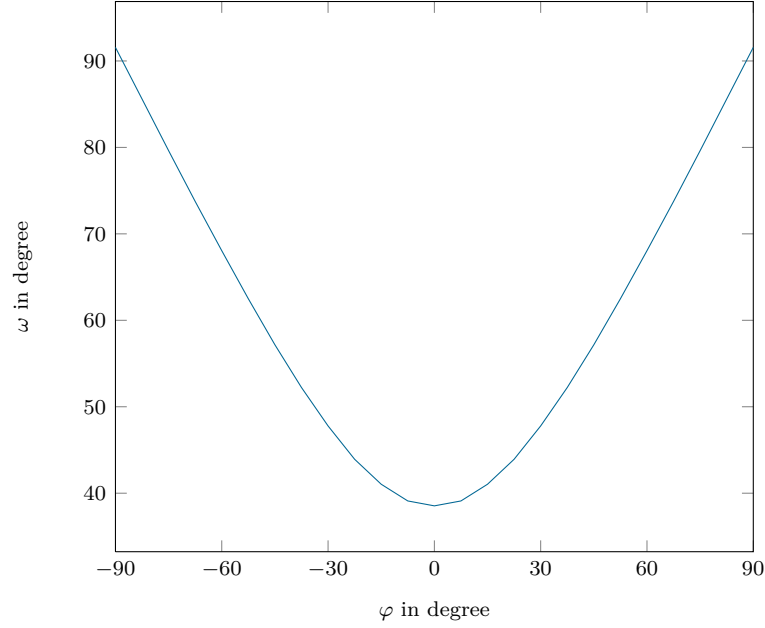


Figure II.21: Shape of the point spread function for $R = 10$, $r_0 = 5$ and $\theta_0 = 0$.

Finally the adjoint Radon transform becomes

$$c^{3*}g(r, \theta) = \frac{2r^2}{R} \int_0^{2\pi} \sqrt{1 - \frac{4R^2r^2 \cos^2(\theta - \varphi)}{(R^2 + r^2)^2}} r \cos(\theta - \varphi) g\left(\frac{2rR}{R^2 + r^2} \cos(\theta - \varphi), \varphi\right) d\varphi. \quad (\text{II.91})$$

The term $g\left(\frac{2rR}{R^2 + r^2} \cos(\theta - \varphi), \varphi\right)$ is constant on the corresponding circular arc but the factor behind does not permit us to call this operator a Back-projection operator along correspondings circular-arcs.

II.4.3 Suited sampling for CART₃

We want a linear sampling for r . If we take a linear sampling for $\omega = \arcsin(p)$, this is not the case. To calculate a more suited sampling for ω , we put $\gamma = 0$ and we consider ω as a function $\omega(x)$ where x is a sampling variable, and so we have

$$\begin{aligned} r &= \frac{R}{p} \left(\sqrt{1 - p^2} + 1 \right) \\ &= \frac{R}{\sin(\omega(x))} (1 + \cos(\omega(x))) . \end{aligned} \quad (\text{II.92})$$

The derivative form leads to

$$\begin{aligned} \frac{dr}{dx} &= \text{constant} = R \\ &= -\frac{1}{2} \omega'(x) \frac{R}{\sin^2\left(\frac{\omega(x)}{2}\right)}, \end{aligned} \quad (\text{II.93})$$

and so to the following differential equation,

$$\omega'(x) + \frac{2c}{R} \sin^2\left(\frac{\omega(x)}{2}\right) = 0. \quad (\text{II.94})$$

The solution of this equation gives

$$\omega(x) = 2 \arctan \left(\frac{R}{cx} \right) . \quad (\text{II.95})$$

Then to construct our sequence $\omega \in [\omega_{\min}, \omega_{\max}]$, we take

$$x = \frac{R}{c \cdot \tan \left(\frac{\omega_{\max}}{2} \right)} : 1 : \frac{R}{c \cdot \tan \left(\frac{\omega_{\min}}{2} \right)} . \quad (\text{II.96})$$

II.4.4 Associated inversion formulae

In this section, we establish and discuss different inversion approaches which can be applied for the inversion of the CART_3 .

II.4.4.a Singular value decomposition

Since $h_1(p) = p$ and $h_2(r) = \frac{2Rr}{R^2 + r^2}$ we can apply Proposition I.3.9 and deduce the following result.

Corollary II.4.2. *The system*

$$\begin{cases} u_n^m(p, \varphi) &= \sqrt{1-p^2} \sin \left((|n| + 2m + 1) \cos^{-1}(p) \right) \frac{e^{in\varphi}}{\pi} , \\ v_n^m(r, \theta) &= \sqrt{\frac{|n| + 2m + 1}{\pi}} \frac{2R(R^2 - r^2)}{(R^2 + r^2)^2} R_m^n \left(\frac{2Rr}{R^2 + r^2} \right) e^{in\theta} , \\ \sigma_n^m &= \sqrt{\frac{4\pi}{|n| + 2m + 1}} . \end{cases} \quad (\text{II.97})$$

for $n \in \mathbb{Z}$ and $m \in \mathbb{Z}^+$ gives a complete singular system of \mathcal{C}^3 from $\mathcal{L}^2(\mathbb{H}_1^3, W_1)$ into $\mathcal{L}^2(\mathbb{H}_2^3, W_2)$.

This result is very important and very useful for the analysis of this transform. It gives the singular values which can make easier any frequency study or filtering in order to erase noise, And it ensures the injectivity of the CART_3 on Hilbert spaces.

A Chebyshev/Zernike expansion can naturally be given and so allows the reconstruction of a function f from the decomposition of $\mathcal{C}^3 f$ on the Chebyshev basis.

Corollary II.4.3. *The minimum-norm solution of the equation $\mathcal{C}^3 f = g$, $g \in \mathcal{L}^2(\mathbb{H}_1^3)$, is given as*

$$f_n(r) = \frac{2R(R^2 - r^2)}{(R^2 + r^2)^2} \sum_{m=0}^{\infty} (|n| + 2m + 1) a_n^m R_m^n \left(\frac{2Rr}{R^2 + r^2} \right) , \quad (\text{II.98})$$

with

$$a_n^m = \sigma_n^{m-1} \langle \mathcal{C}^3 f, u_n^m \rangle_{\mathbb{H}_1^3, W} . \quad (\text{II.99})$$

II.4.4.b Regularized inversion formula in CHD

Proposition I.2.4 gives us the following inversion formula in circular harmonic domain for the CART_3 .

Corollary II.4.4.

$$\begin{aligned} f_n(r) &= (-)^n \frac{2R(R^2 - r^2)}{(R^2 + r^2)^2} \left[\frac{1}{\pi t} \int_0^t dp \frac{d}{dp} \left(\frac{(\mathcal{C}^3 f)_n(p)}{\sqrt{1-p^2}} \right) U_{|n|-1} \left(\frac{p}{t} \right) \right. \\ &\quad \left. - \frac{1}{\pi t} \int_t^1 dp \frac{d}{dp} \left(\frac{(\mathcal{C}^3 f)_n(p)}{\sqrt{1-p^2}} \right) \frac{\left((p/t) - \sqrt{(p/t)^2 - 1} \right)^{|n|}}{\sqrt{(p/t)^2 - 1}} \right]_{t = \frac{2Rr}{R^2 + r^2}} . \end{aligned} \quad (\text{II.100})$$

This integral represents the regularized form of the inversion formula of the CART₃ in circular harmonic domain. It has the advantage to be stable but it is difficult to implement because of the derivative of the data. Therefore we can follow the same approach of Chapman and Cary [8] or the one we derived for the CART₁ above with the appropriated change of functions.

II.4.4.c Filtered Back-projection and Stable inversion in circular harmonic domain

Application of the Corollary I.3.1 permits to write down the "Filtered Back-projection" formula of the CART₃.

Corollary II.4.5. *The "filtered back-projection" is given by*

$$\begin{aligned} f(r, \theta) &= \frac{R}{\pi^2} \frac{R^2 - r^2}{(R^2 + r^2)^2} \int_0^\pi p.v. \int_{-\infty}^{+\infty} \frac{\frac{\partial}{\partial p} \left(\frac{(\mathcal{C}^3 f)(p, \varphi)}{\sqrt{1-p^2}} \right)}{\frac{p(R^2+r^2)}{2Rr} - \cos(\theta - \varphi)} dq d\varphi, \\ &= \frac{(R^2 - r^2)}{r(R^2 + r^2)} \int_0^\pi \left(\mathcal{H} \frac{\partial}{\partial p} \left(\frac{\mathcal{C}^3 f(p, \varphi)}{\sqrt{1-p^2}} \right) \right) \left(\frac{2Rr}{R^2 + r^2} \cos(\theta - \varphi), \varphi \right) d\varphi. \end{aligned} \quad (\text{II.101})$$

We see that the term of "filtered back-projection" is a misuse of language since this inversion formula makes appear a "weighted" adjoint operator of the CART₃. As the filtering is of the same kind than in the classical Radon transform case, same apodization methods can be used : Hann filter, Shepp-Logan filter, And this approach has the advantage to be easily implementable with short computing time.

An alternative form can be obtained in circular harmonic domain using Corollary I.3.3.

Corollary II.4.6 (Stable inversion in CHD).

$$f_n(r) = \frac{4R(R^2 - r^2)}{(R^2 + r^2)^2} \int_{-\frac{2Rr}{R^2+r^2}}^{\frac{2Rr}{R^2+r^2}} \left(\mathcal{H} \frac{d}{dp} g_n(p) \right) \frac{T_n \left(\frac{p(R^2+r^2)}{2Rr} \right)}{\sqrt{\frac{4R^2 r^2}{(R^2+r^2)^2} - p^2}} dp \quad (\text{II.102})$$

with

$$g_n(p) = \frac{(\mathcal{C}^2 f)_n(p)}{\sqrt{1-p^2}}.$$

This formula has the advantage to be very simple to understand and to compute. Furthermore the filtering of the data is very flexible for the regularization such that a mollification of the kernel [32].

II.5 Implementation methods for different equations

As an illustration we present different steps of the implementation for the CART_2 . The same scheme can be applied in the case of CART_1 and CART_3 . The implementation is based on three steps : image formation, adding a noise on the data and image reconstruction.

II.5.1 Image formation

Equation (II.69) describes the image formation process but we have seen an alternative formulation, eq. (II.75), which is more suited to a numerical computation since it considers the cartesian representation of the studied function f , h . In order to simplify the calculation of the forward CART_2 , we use the parameter ω and the cartesian representation. From now on we consider the following notation for the image formation process

$$(\mathcal{C}^2 h)(\varphi, \omega) = \int_{\frac{\pi}{2}-\omega}^{\frac{\pi}{2}+\omega} \frac{R}{\sin \omega} h(x(\varpi), y(\varpi)) d\varpi . \quad (\text{II.103})$$

Let :

- H : be the original matrix of size $N \times N$ (the studied function $h(x, y)$).
- $\bar{\omega}$: be a linearly spaced vector of size N_ω from $d\omega$ to ω_{\max} where

$$\omega_{\max} = \arctan \left(\frac{\sqrt{2} RN}{R^2 - \frac{N^2}{2}} \right)$$

represents the maximum value of the angle ω considering a scattering medium of size $N \times N$ and $d\omega = \frac{\omega_{\max}}{N_\omega}$ stands for the sampling step,

- $\bar{\varphi}$: be a linearly spaced vector of size N_φ from $d\varphi$ to 2π where $d\varphi = \frac{2\pi}{N_\varphi}$ is the sampling step,
- P : be the projection matrix of size $N_\varphi \times N_\omega$ corresponding to the forward CART_2 of the cartesian function $h(x, y)$,
- $\bar{\varpi}_j$: be a linearly spaced vector of size N_ϖ from $\left(\frac{\pi}{2} - \omega_j\right)$ to $\left(\frac{\pi}{2} + \omega_j\right)$ defined for each value of $\omega_j \in \bar{\omega}$ with a sampling step $d\varpi = \frac{2\omega_j}{N_\varpi}$,
- the following parametric system be for $(\varphi_i, \omega_j, \varpi_k) \in \bar{\varphi} \times \bar{\omega} \times \bar{\varpi}_j$:

$$\begin{cases} x_{ijk} = \frac{R}{\sin \omega_j} \sin(\varpi_k + \varphi_i) - \frac{R}{\tan \omega_j} \cos \varphi_i \\ y_{ijk} = \frac{-R}{\sin \omega_j} \cos(\varpi_k + \varphi_i) - \frac{R}{\tan \omega_j} \sin \varphi_i . \end{cases}$$

To calculate the numerical value of this integral, we use the trapezoidal rule to interpolate H_{ijk} from $h(x_{ijk}, y_{ijk})$ and we obtain the following sum

$$P_{ij} = \frac{2R}{N_\omega} \frac{\omega_j}{\sin \omega_j} \sum_{k=1}^{N_\omega} H_{ijk} .$$

II.5.2 Noisy data

Adding gaussian noise is a standard technique. Considering Poisson noise, we consider all the points in the data space bounded, then $Y \sim \mathcal{P}(X)$ can be obtained from X with a given SNR with

$$Y \sim \frac{1}{10^{\frac{SNR}{10}}} \frac{\sum_{i=1}^{N_X} X(i)^2}{\sum_{i=1}^{N_X} X(i)} \mathcal{P} \left(\frac{\sum_{i=1}^{N_X} X(i)}{\sum_{i=1}^{N_X} X(i)^2} X \right). \quad (\text{II.104})$$

II.5.3 Image reconstruction

II.5.3.a Filtered back-projection

We use the standard way performing the Hilbert transform in Fourier space and multiplying by an apodized ramp filter (here Hann function is used as apodization).

The analytical inversion formula has the following form

$$h(x, y) = \frac{2R(R^2 + (x^2 + y^2))}{(R^2 - (x^2 + y^2))^2} \int_0^\pi \check{g}^* \left(\varphi, \frac{2R}{R^2 - (x^2 + y^2)} (x \cos \varphi + y \sin \varphi) \right) d\varphi.$$

The function $\check{g}^*(\varphi, q)$ corresponds to the filtering of the function $\check{g}(\varphi, q) = \frac{(\mathcal{C}^2 h)(\varphi, \arctan q)}{\sqrt{1 + q^2}}$. Hence before reconstructing the original image, $h(x, y)$, we compute the filtering of g . This step is the same as in the classical Radon transform, that is to say

$$\check{g}^*(\varphi, q) = \mathcal{F}^{-1} \{ |\nu| \cdot \mathcal{F} \{ \check{g}(\varphi, q) \} \},$$

where \mathcal{F} (resp. \mathcal{F}^{-1}) stands for the 1D-Fourier transform (resp. the inverse 1D-Fourier transform). Its computation is performed by a Fast Fourier transform (FFT). Because of frequency unstability and cut-off we have to apodize the ramp filter, $|\nu|$, with a smooth function. We choose the Hann filter defined by :

$$H(\nu) = \begin{cases} 0.5 \left(1 + \cos \left(\pi \frac{\nu}{\nu_{\max}} \right) \right) & \text{if } |\nu| < \nu_{\max} \\ 0 & \text{if } |\nu| \geq \nu_{\max} \end{cases},$$

where ν_{\max} is the maximum value of the frequency of the discretized projections. Thus the ramp filter becomes $H(\nu)|\nu|$, see Fig. II.22.

Then the adjoint operator is applied on the curve

$$q = \frac{2R}{R^2 - (x^2 + y^2)} (x \cos \varphi + y \sin \varphi),$$

which is the arc of circle $C(\varphi, \omega)$. Therefore the Back-Projection is performed over the same circular arcs as in the forward transform.

Let

- \bar{q} : be a linearly spaced vector of size N_q from $\tan d\omega$ to $\tan \omega_{\max}$ and
- G : be the filtered projections matrix of size $N_\varphi \times N_q$.

Finally the back-projection operator is computed by

$$\forall (i, j) \in [1, N]^2, \quad H_{ij} = \frac{4\pi}{N_\varphi} \frac{R(R^2 + (x_i^2 + y_j^2))}{(R^2 - (x_i^2 + y_j^2))^2} \sum_{k=1}^{N_q} G_{ijk},$$

where G_{ijk} is calculated by linear interpolation of $\check{g}^* \left(\varphi_k, \frac{2R}{R^2 - (x_i^2 + y_j^2)} (x_i \cos \varphi_k + y_j \sin \varphi_k) \right)$ on the vector \bar{q} .

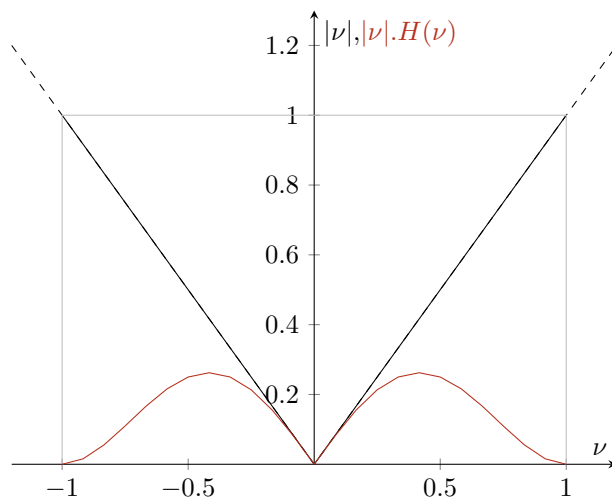


Figure II.22: Representation of the ramp filter $|\nu|$ with apodization $H(\nu) \cdot |\nu|$.

II.5.3.b Regularized inversion formula in CHD

We are inspired by the numerical approach of Chapman [8] which considers a Gauss-Lobatto interpolation to compute the inversion formula. Then the integral becomes a summation of the integrand for the following zeros of $T_n(x)$:

$$x_k = \cos\left(\frac{\pi(k + 1/2)}{N}\right). \quad (\text{II.105})$$

Therefore we can apply the same numerical approach after changing the function space from the corresponding CART space to the standard Radon transform space. However in the case of CART_1 and CART_3 , we derived a more suited way because of the parametrization see II.2.5.b.

II.5.3.c Stable inversion formula in CHD

In this case no interpolation step is required. We just have to evaluate the integral for the same sampling between p and r and by summation over p . In addition the filtering of the data is performed by the same way that in the FBP case, see above.

II.5.3.d Chebyshev/Zernike expansions

The reconstruction by Chebyshev/Zernike expansions is performed by projection of the data CART_i in the corresponding basis (Chebyshev polynomials in the straight line case) and then obtained coefficients are used to reconstruct the studied image, f , through its expansion in Zernike polynomials space.

To obtain an expansion in Chebyshev polynomials, first consider the function

$$(T_\varphi g)(\nu) = \int_{-R}^R \frac{\sin(\nu \arccos(p/R))}{\sqrt{1 - (p/R)^2}} g(p, \varphi), \quad (\text{II.106})$$

and the discrete inverse Chebyshev transform defined by

$$(T_\varphi^{-1} g)(p_j) = \sum_{\nu=-N/2}^{N/2} e^{i\nu \arccos p_j/R} (T_\varphi g)(\nu) = g(p, \varphi). \quad (\text{II.107})$$

Considering the sinogram data of size $N_p \times N_\varphi$ with the samplings

$$\left\{ \begin{array}{l} p_j = R \cos j \frac{2\pi}{N_p}, \quad j \in \mathbb{Z}, \quad -N_p/2 + 1 \leq j \leq N_p/2, \\ \varphi_k = \frac{2\pi}{N_\varphi} k, \quad k \in \mathbb{Z}^+, \quad 0 \leq k \leq N_\varphi, \end{array} \right. \quad (\text{II.108})$$

one can perform the forward Chebyshev transform as a sine transform and the inverse transform as a harmonic sum. The discrete forms of these operations can then be evaluated by the discrete FFT.

We now have the data in the form required for reconstruction using Chebyshev/Zernike expansions. Let the circular harmonic coefficients a_{nm} with index $\nu = |n| + 2m + 1$ be

$$a_{nm} = \int_0^{2\pi} e^{-in\varphi} (T_\varphi g)(\nu) d\varphi. \quad (\text{II.109})$$

Then the underlying object f is reconstructed through a weighted sum of Zernike polynomials $R_m^n(r)$:

$$f(r, \theta) = \frac{1}{2} \sum_{n,m} (|n| + 2m + 1) a_{nm} R_m^n(r) e^{in\theta}. \quad (\text{II.110})$$

Clenshaw's algorithm [9] may be used to evaluate these series with finite upper limits.

II.6 Simulation Results

We propose to test our inversion formulae on the well-known Shepp-Logan phantom for three modalities of Compton scattering tomography presented above. The scattering medium is discretized with 256×256 pixels. We consider the following number of projections for :

- $CART_1$ $N_\varphi = 1024$, $N_p = 1024$, the number of expansions coefficients is 1024 and the center of cartesian coordinates is on the below left of the image,
- $CART_2$ $N_\varphi = 256$, $N_\omega = 256$, the number of expansions coefficients is 512, we display $CART_2$ data in terms of φ and $\omega = \arctan p$ and the center of cartesian coordinates is the center of the image,
- $CART_3$ $N_\varphi = 1024$, $N_\tau = 901$, the number of expansions coefficients is 1024, we display $CART_3$ data in terms of φ and $\tau = p^{-1}$ and the center of cartesian coordinates is on the below of the image.

In the case of $CART_1$ and $CART_3$ we consider a very large number of projections because the measurement space is unbounded and consequently too large. Despite this increasing of the resolution, data remain uncomplete which generates much artifacts inside and outside the object under study. To erase outside artifacts, we may invoke a support theorem corresponding to our case which is based on the one shown by Helgason [22] for the classical Radon transform. Furthermore the object is off-centered and then can be considered outside of a given unit disk. By this way the definition of the corresponding curves and of its integral supports are satisfied.

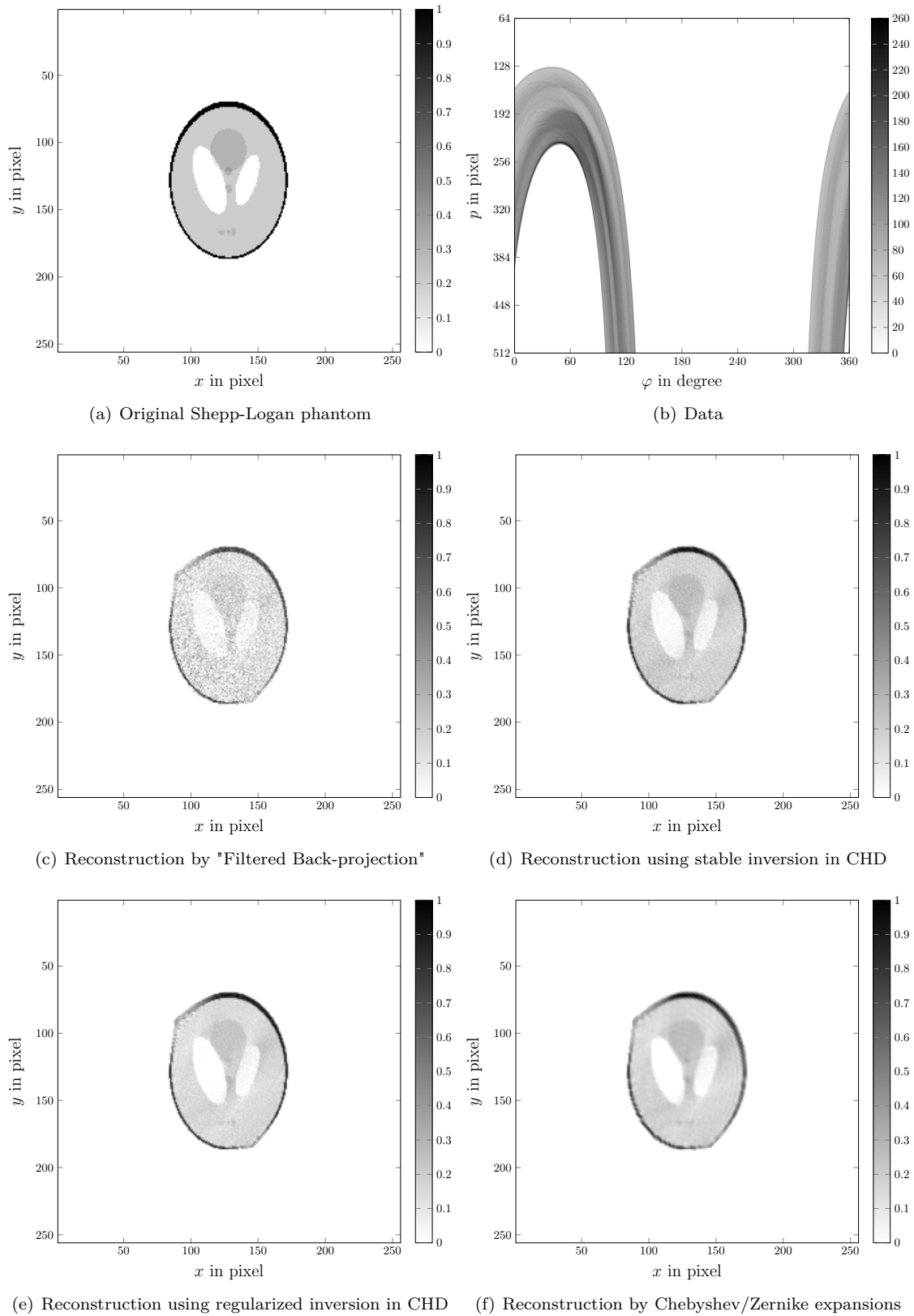
On the one hand we test the robustness of each inversion formulae for each CART in presence of gaussian noise with a signal-to-noise (SNR) equals to 20 dB (*i.e.* 1%). This kind of noise are typical in the modeling of detectors. On the other, since photon emission process follows Poisson's law, this phenomenon is one of the main cause of degradation of the quality of image reconstruction in Compton scattering tomography. Thus the projections become in both cases $\tilde{g}(\mathbf{t}) \sim \mathcal{P}(\mathcal{C}^i f(\mathbf{t}))$ where \mathcal{P} stands for the Poisson law. Here we study the robustness of our algorithms taking into account this phenomenon for $SNR = 13dB$ (*i.e.* 5%).

Figures II.23,II.25 and II.27 (resp. II.24,II.26 and II.28) give the results of reconstruction using gaussian (resp. Poisson) noisy data (b) obtained from original image (a). We can separate these four reconstructions in two categories : filtered (c,d) and consistent (e,f). In the case of $CART_1$ even if filtered approaches are fast and simple to implement, they are less robust to noise than consistent ones. In particular the "filtered back-projection" algorithm gives a reconstruction with a lot of artifacts. As mentioned above, it is due to the inverse of cos function which is numerically unstable. For $CART_2$ we see that the robustness with Poisson noise is variable according to the method. Nevertheless as our data are complete (bounded measurement space) the filtered approaches seem to be better than consistent ones in this example and in presence of noise. And concerning $CART_3$ the problem of incomplete data appears clearly with the "filtered back-projection" algorithm since the center area of the phantom is ill-recovered. With the Zernike/Chebyshev expansions this lack of data is reflected by a too smooth reconstruction.

We have tested our reconstruction methods on three different CART for two noises, gaussian and Poisson, and simulation results appear to be good. Indeed for a 20 dB gaussian noise, the small structures are well recovered. And even if Poisson law cannot be defined with a \mathcal{L}^2 -norm, results are satisfying in this case. However total variation algorithms could be applied in future works in order to take it into account more rigorously in the inversion procedure.

II.7 Conclusion

We knew that Radon transform defined on generalized Cormack's curves could be defined and inverted analytically. In chapter I we gave the analytical inversion formulae for Radon transforms over C_α . The exploration of a certain subclass, C_1 , permitted to extend the singular value decomposition for these generalized Radon transforms. In particular this last subclass make appear the well-known straight line as well as three others kind of curves which are the basis of three different modalities of Compton scattering tomography ($CART_{1,2,3}$). Then, inversion formulae and singular value decomposition are directly deduced in those cases. Finally we have tested our different reconstruction formulae on the different CARTs for two noises, gaussian and Poisson. In the case of the gaussian noise, the small structures are well recovered and results are satisfying in the Poisson case which attests of the theoretical feasibility and future interest of the associated modalities on Compton scattering tomography. As Poisson law cannot be defined with a \mathcal{L}^2 -norm, total variation algorithms could be applied in future works to take into account this last point. In addition the $CART_1$ and the $CART_3$ suffered incompleteness in data because of their integration support. This aspect could be studied in more details in future works.

Figure II.23: Simulation Results for $CART_1$ with a gaussian noise of 20 dB

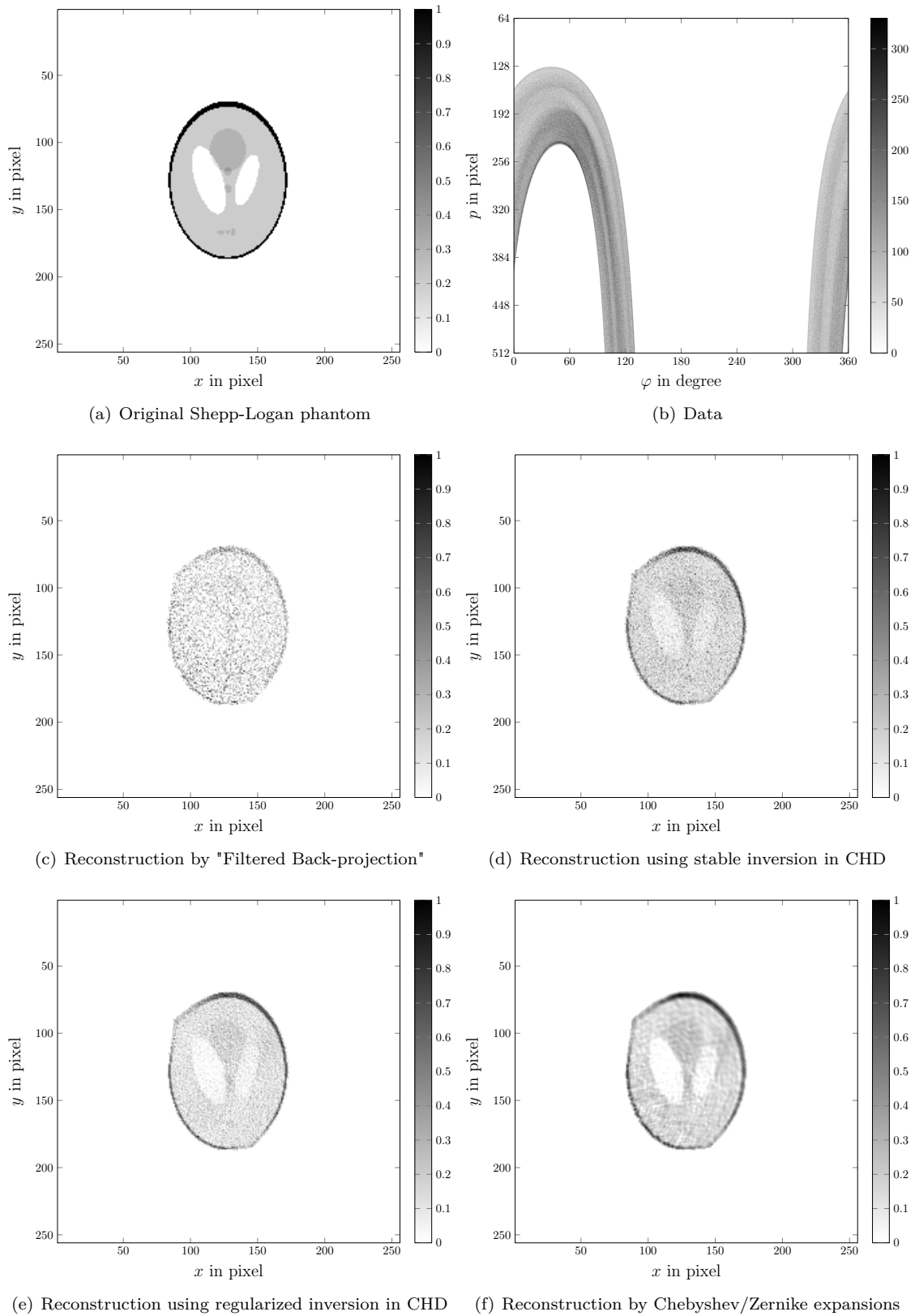
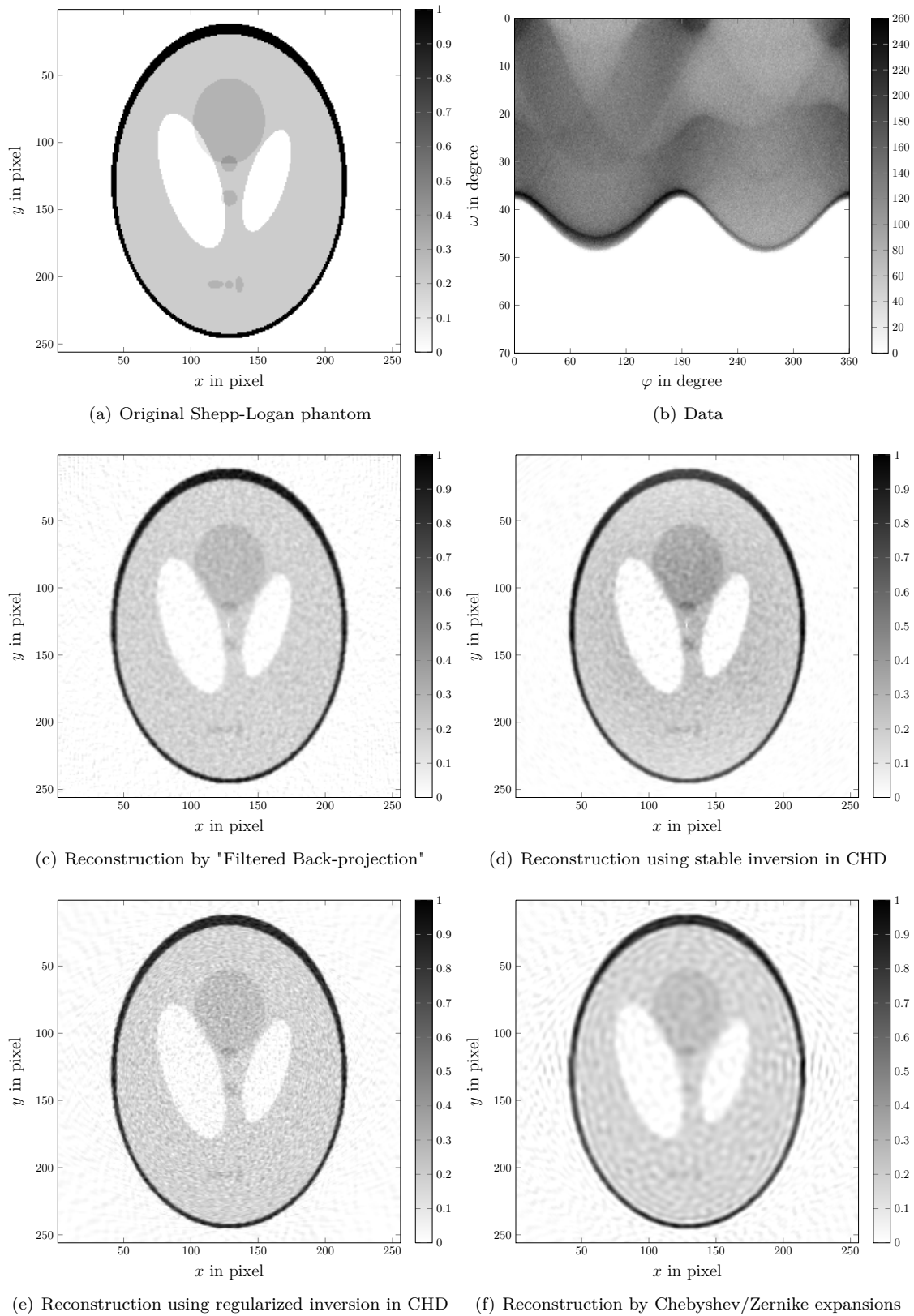


Figure II.24: Simulation Results for $CART_1$ with a Poisson noise of 13 dB

Figure II.25: Simulation Results for $CART_2$ with a gaussian noise of 20 dB

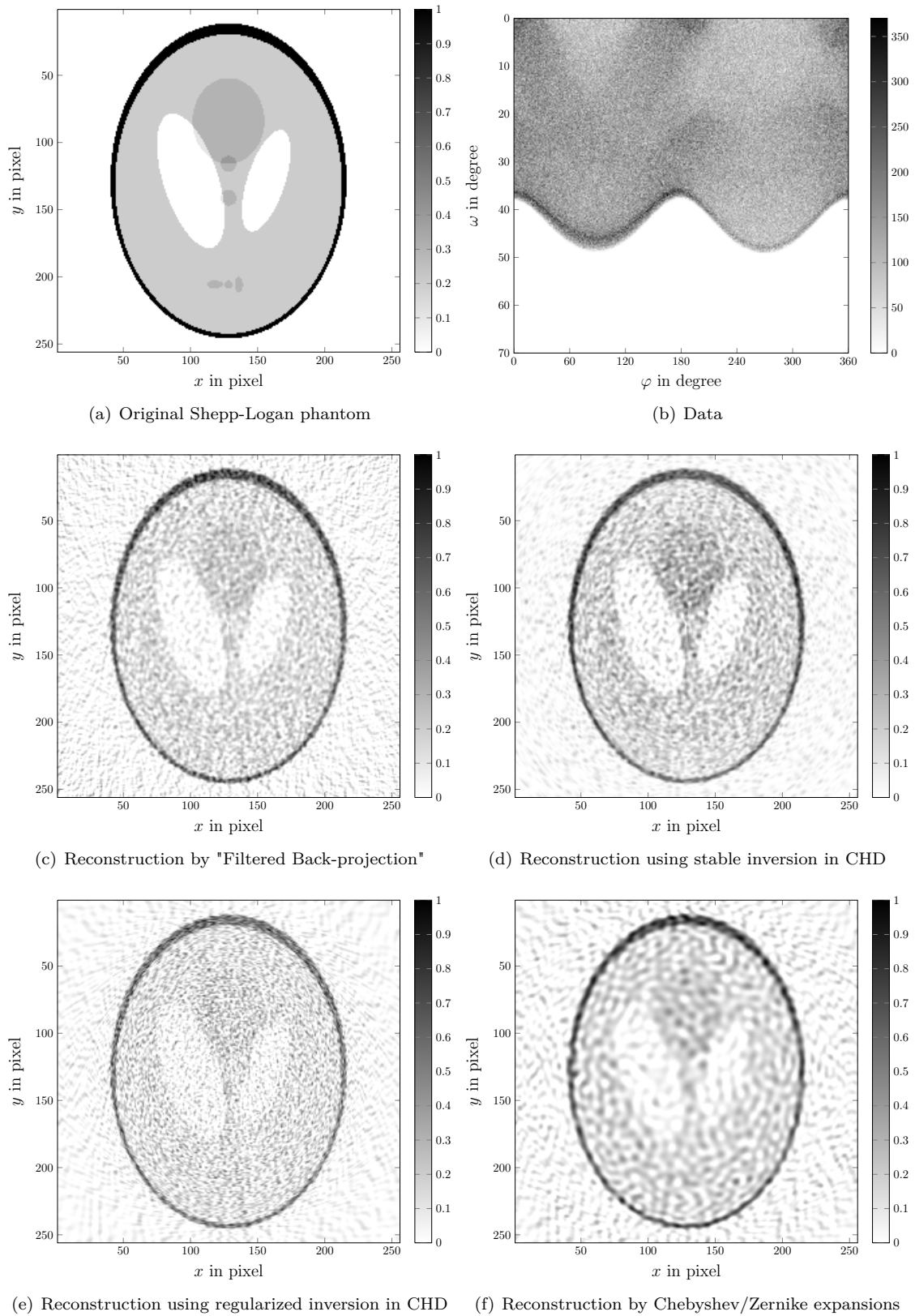
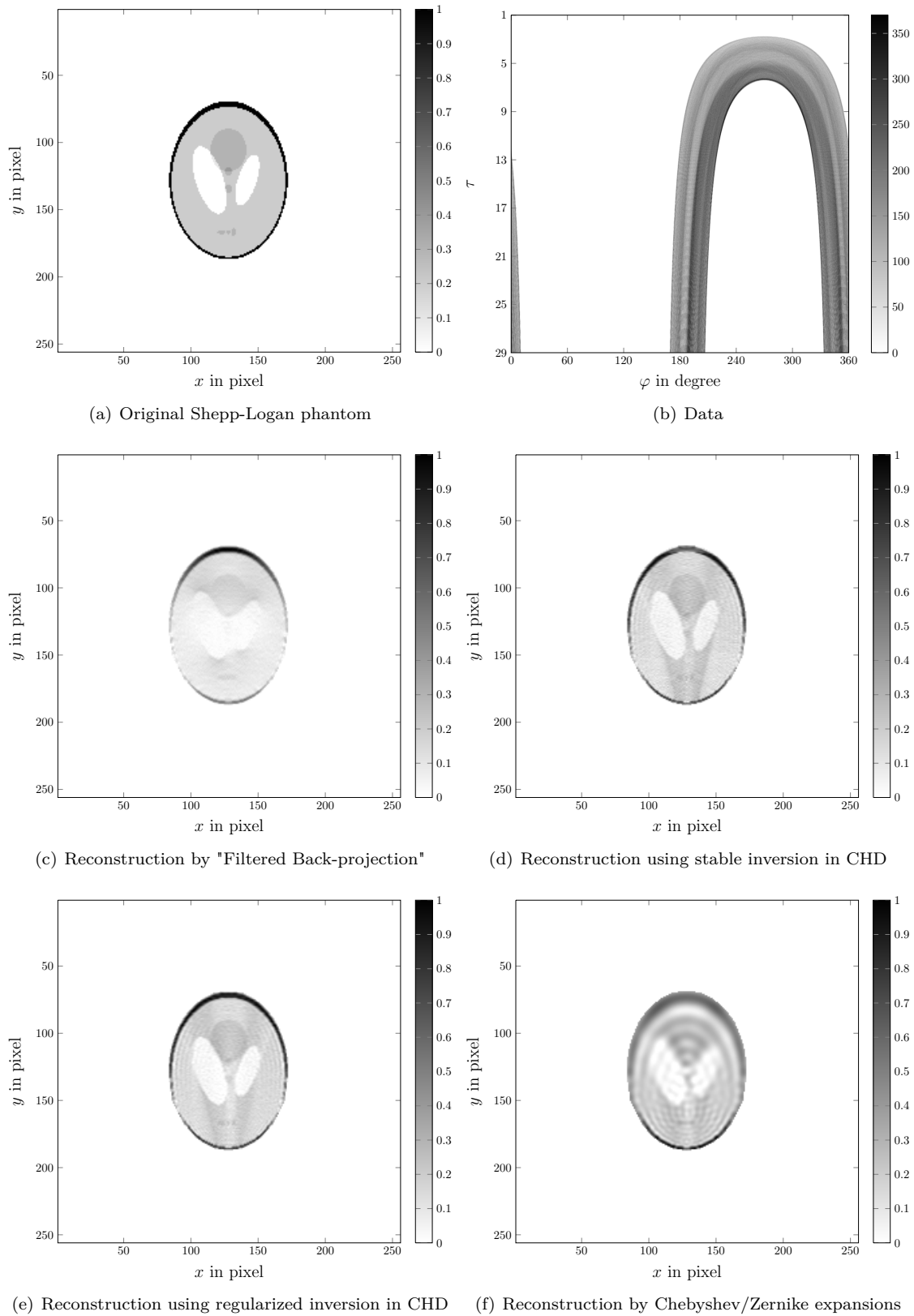


Figure II.26: Simulation Results for $CART_2$ with a Poisson noise of 13 dB

Figure II.27: Simulation Results for $CART_3$ with a gaussian noise of 20 dB

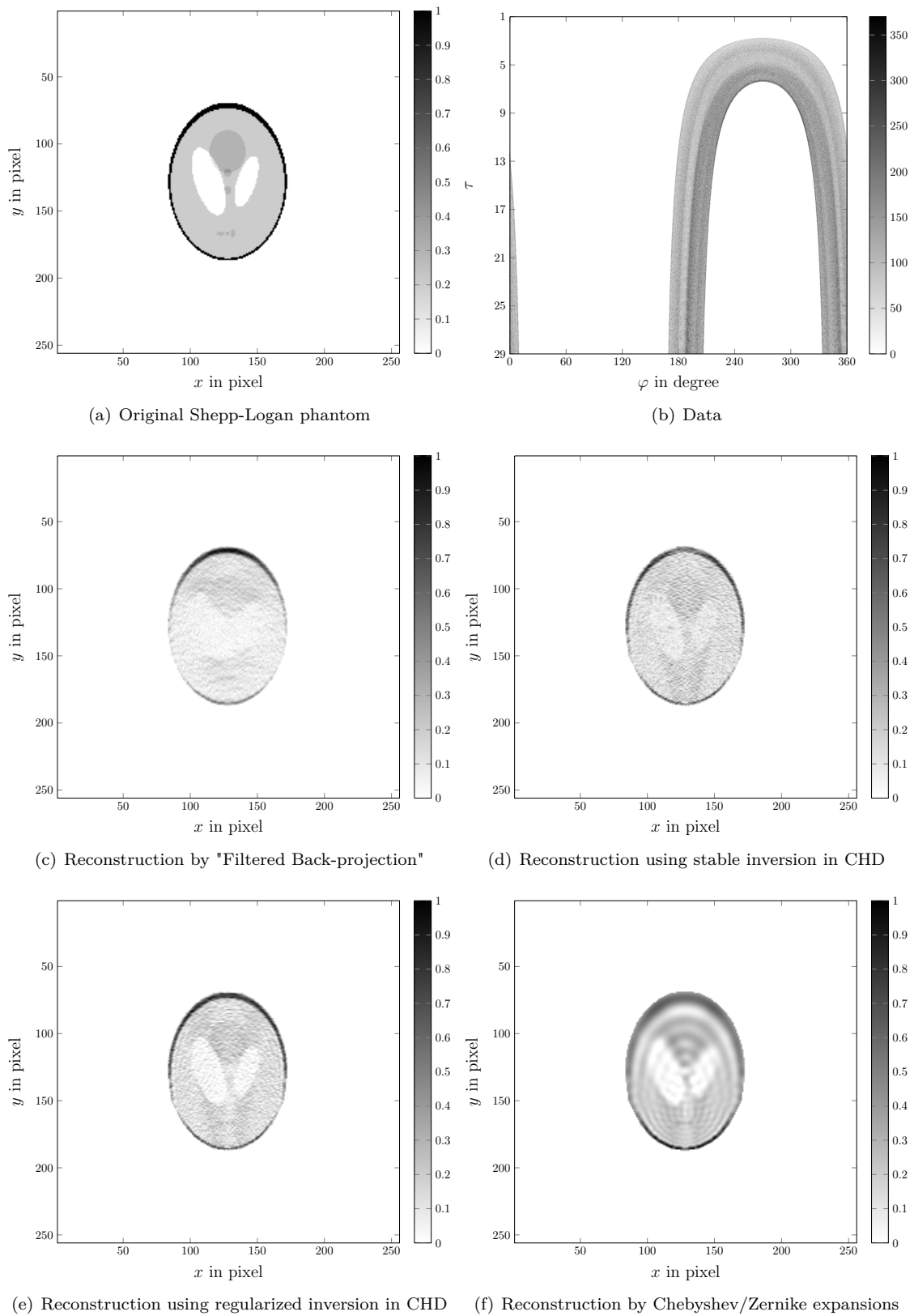


Figure II.28: Simulation Results for $CART_3$ with a Poisson noise of 13 dB

A new concept of bimodality in Compton scattering tomography

The requirement for fast and reliable diagnostics or therapy planning in modern healthcare systems has led to a wealthy development of hybrid imaging technologies. While traditional imaging techniques such as X-ray Computed Tomography (CT) and magnetic resonance imaging (MRI) provide information on patient's anatomy or on the location and extent of the disease, Positron Emission Tomography (PET) and Single-Photon Emission Computed Tomography (SPECT) are able to detect biomolecular changes (even prior to anatomic change) and the biochemical status or the physiological function of a human organ. The idea of combining imaging techniques has become a very useful clinical tool. The introduction of combined PET/CT scanners revolutionized clinical practice and received widespread clinical acceptance [5, 21]. At the beginning of the 21st century, a further advance was made in the use of scattered radiation for imaging, to be feasible for emission imaging. For a radiating (or made radiating) object, a SPECT gamma camera can be set to register, without having to rotate around this object, a set of images at different scattered energies. The crux of the matter is that one can show that from this data set, a three-dimensional object reconstruction is possible. Moreover, a two-dimensional version of this scattered radiation has been shown to be feasible in the last few years, referred to as V-line emission imaging (VEI) [42, 68]. Thus, it is tempting (and logical) to combine Compton scattering tomography with V-line emission imaging as the first bimodal scatter radiation imaging, which is the topic of this chapter.

First we introduce the concept of attenuation correction techniques in conventional tomography. Then in section 2 a suited attenuation correction algorithm is proposed in order to take into account physical phenomenon in our modalities. Section 3 presents our novel bimodality in CST and the associated attenuation correction process with simulation results attesting of the theoretical feasibility and interest of this new imaging system.

This chapter invokes a lot of concepts presented in the chapter II. So we encourage the reader to look into the first section of this chapter before to continue.

III.1 Attenuation correction algorithms

III.1.1 Detection of the contours of the attenuating medium

Most of the methods of attenuation correction requires knowledge of contours of the attenuating medium. For more details we invite the reader to relate to the state of the art of Gullberg [20] on the detection of contours of the attenuating medium.

III.1.2 Constant attenuation factor correction

These methods are particularly suited to cases of brain and abdominal studies. Besides the skull made of bone (and relatively thin compared to the head), the tissues have about the same attenuation. And so one attenuation coefficient can be attributed to this zone. Several methods exist for this case, in addition to those that we present later, we note in particular the exact method of Bellini [4], which compensates the attenuation factor in an uniformly absorbing medium. Recent developments [75, 76] showed that image enhancement could be made, by considering no longer attenuation as uniform for these applications.

Pre-processing methods The attenuation compensation is performed on the projections before image reconstruction. An average of the combined projections is performed to make the degradation due to attenuation less dependent on emitting sources. The average strongly depends on the geometric thickness of the patient, is substantially independent of the thickness of the source and does not depend on the depth of the source. The arithmetic mean depends strongly on the thickness of the patient but is substantially independent of the thickness of the source. Both methods are easy to implement, but are only really effective with a radioactive source that is not distributed in an uniformly attenuating medium [70], moreover they require more knowledge of the thickness of the source. With methods using the arithmetic mean, the activity located at the center of the reconstructed region is underestimated, whereas the methods using geometric mean tend connecting the sources normally isolated.

- **The method of Sorenson [63]** - The idea is to get an attenuation correction for each pixel from the geometric mean of the measured projections: $p'(r, \theta)$ and $p'(r, \theta + \pi)$ by the camera in two opposite positions at 180° . At this average a term correction in sinh is applied. The modified projections are obtained assuming an uniformly distributed activity (if the source is extended) and the attenuation factor constant. The corrected projections $p(r, \theta)$ are then

$$p(r, \theta) = \sqrt{p'(r, \theta) \cdot p'(r, \theta + \pi)} \frac{\mu FL}{2} \frac{e^{\mu FL/2}}{\sinh(\mu FL/2)}, \quad (\text{III.1})$$

with μ the constant linear attenuation coefficient, L the thickness of the attenuating medium and F the active fraction of L on which the activity is considered (assumed constant with respect to θ).

Ideally the attenuation correction method calculates projections that would be obtained if the attenuation was null, the effect of the attenuation is thus removed from acquired images. It is then possible to use a method of reconstruction taking not into account attenuation such as filtered backprojection for the studied object.

In practice F (portion of activity) is not known and is usually set to 1 or 0.5. This choice has little influence on the results because the correction factor added to the geometric mean depends little on F [51]. This method is very easy to implement but improves the quality of the image reconstruction only for objects with a simple geometry and a constant activity.

Post-processing methods These methods are essentially adaptations of the method proposed by Chang. In this approach, the projections are first reconstructed without attenuation correction, then the object is corrected (post-treatment) to eliminate distortions caused by attenuation factor.

- **The method of Chang [7, 62]** - This is the most used method. A reconstruction is applied to the measured projections. An non-corrected attenuation image is obtained. Each pixel of this will be corrected by the average attenuation coefficients over all projection angles. For the pixel coordinates (x, y) we have the following correction coefficient:

$$C(x, y) = \left(\frac{1}{N} \sum_{i=1}^N e^{-\mu I_{\theta_i}} \right)^{-1}, \quad (\text{III.2})$$

with N the number of projections, μ the constant attenuation factor of the studied matter and I_{θ_i} the distance from the contour of the object to the point (x, y) in the spreading direction θ_i . This method is true only in the case of a point source in a medium of uniform attenuation factor. With an extended source, the correction factor overstates or understates some parts of the distribution.

Studies of Murase [43] showed that the method of Chang is an iterative method that converges the most quickly with a relatively small error.

- **Iterative methods** - Even if they often require a longer computation time, they offer the advantage of access quantitative results and can be used in cases where the analytical solution is unknown. The best known methods are those of Walter and Morozumi [29, 40, 41, 72].

III.1.3 Attenuation correction with a given heterogeneous attenuation map

In this section, we assume that the attenuation map is known. The comparative study of Murase [43] on the various iterative methods showed that the method of Chang is one of the most effective. We will see an adaptation of it for cases of non-uniform attenuation, called GCC (Generalized Chang Correction). The correction is performed by multiplying the correction matrix by the reconstructed image without correction: it is a post-correction.

Maze [38] proposed another iterative method, called Iterative Pre Correction (IPC). This corrects the projections before the reconstruction step.

Any iterative method requires to compute new projections of radioactive distribution and then reconstructions from projections estimated at each step.

Generalized Chang Correction (GCC) The principle of the GCC method is quite similar to the standard method of Chang. The correction matrix is modified to reflect heterogeneity of the medium. Thus the correction factor at point (x, y) is given by

$$C(x, y) = \left(\frac{1}{N} \sum_{i=1}^N e^{-\int_{P_{x,y}^{\theta_k}} \mu_{x,y}(r, \theta_k) dr} \right)^{-1}, \quad (\text{III.3})$$

with N the number of projections, $P_{x,y}^{\theta_k}$ the straight line path from the point (x, y) to the contour of the object in the direction θ_k , and $\mu_{x,y}(r, \theta_k)$ the attenuation value in polar coordinates centered at (x, y) in the direction θ_k .

Iterative Pre-Correction (IPC) Another alternative proposed by Maze [38] is possible to correct the attenuation map. The projections are corrected before reconstruction. From the measurement, the aim is to get the images that would be measured without attenuation. The

attenuation of the activity of each coordinate point (x, y) measured in the direction θ_k is given by the following factor:

$$e^{-\int_{P_{x,y}^{\theta_k}} \mu_{x,y}(r, \theta_k) dr}, \quad (\text{III.4})$$

with $P_{x,y}^{\theta_k}$ the straight line path from the point (x, y) to the contour of the object in the direction θ_k , and $\mu_{x,y}(r, \theta_k)$ the attenuation value in polar coordinates centered at (x, y) in the direction θ_k .

For each point of a projection, a number of pixels of the source object are involved in its formation. Between a given point of the projection and each pixel of the source object, the photon flux undergoes a given attenuation. The correction factor used for this point of projections is then the mean of all previously defined attenuations

$$C(x, y) = \sum_{E_k} e^{-\int_{P_{x,y}^{\theta_k}} \mu_{x,y}(r, \theta_k) dr}, \quad (\text{III.5})$$

with E_k the set of pixels of the area involved in the formation of the projections in the direction θ_k on a given line.

The initial step of IPC algorithm provides the first corrected projections dividing point by point the original projections (measured by the detector) by the correction matrix proposed. The filtered back-projection of corrected projections allows us to obtain a first estimation of the object. Then successive iterations of the IPC algorithm can refine the estimate of the object.

III.2 Generalized Iterative Pre-Correction (GIPC) algorithm for Cormack's Radon transforms

The gap between a theoretical modeling (in integral geometry for instance) and realistic applications can be large. And in numerous cases taking into account some phenomenon can hinder the derivation of an analytical inversion formula. Hence to correct these factors becomes necessary for image reconstruction.

In the case of the attenuated Radon transform, Novikov showed an analytical inversion formula but before that Chang was the first to propose a correction method on the image. After him Mazé [38] gave a method to correct the data, the iterative pre-correction algorithm (IPC). In these two approaches the correction consists in dividing by the mean of the distortion but in different spaces.

In this section, we establish a generalized iterative pre-correction algorithm (GIPC) which suits to the problem of attenuation correction in our modalities in CST presented in Chapter II. The convergence is proven if we consider the set of functions in which the studied transform is injective. Following Chapter I, this injectivity is ensured in Hilbert spaces (see SVD).

III.2.1 Presentation of the algorithm

We consider two measurable spaces $\mathcal{X}, \mathcal{Y} \subset \mathbb{R}^n$. Let $\mathcal{L}_+^2(\mathcal{X})$ (resp. $\mathcal{L}_+^2(\mathcal{Y})$) be the space of square-summable functions defined on \mathcal{X} (resp. \mathcal{Y}) such that

$$\forall f \in \mathcal{L}_+^2(\mathcal{X}) \quad \text{and} \quad \forall X \in \mathcal{X}, \quad f(X) \geq 0. \quad (\text{III.6})$$

Let $T : \mathcal{L}_+^2(\mathcal{X}) \longrightarrow \mathcal{L}_+^2(\mathcal{Y})$ be a integral operator defined by its integral kernel

$$(Tf)(Y) = \int_{X \in \mathcal{X}} K_T(Y, X) f(X) dX. \quad (\text{III.7})$$

with

$$\forall (X, Y) \in \mathcal{X} \times \mathcal{Y}, \quad K_T(Y, X) \geq 0,$$

then T is a positive linear operator.

Definition III.2.1. Let T' be the restriction of T such that T' is bijective. T' is then defined on a subset of $\mathcal{L}_+^2(\mathcal{X})$, \mathcal{F}_1 and we can define the inverse operator $T^{-1} : \mathcal{F}_2 \subset \mathcal{L}_+^2(\mathcal{Y}) \longrightarrow \mathcal{F}_1$ such that $T^{-1} \circ T' = Id_{\mathcal{F}_1}$. T^{-1} is a positive linear operator.

The kernel of the operator T' is submitted to a positive distortion $D(Y, X) \in \mathcal{L}^2(\mathcal{X} \times \mathcal{Y})$ such that

$$\exists d, D_m \in \mathbb{R}^+ < \infty \quad \text{s.t.} \quad \forall (X, Y) \in \mathcal{X} \times \mathcal{Y}, \quad d < D(Y, X) \leq D_m \quad (\text{III.8})$$

Thus we can define a "distorted" operator $T^\Phi : \mathcal{F}_1 \longrightarrow \mathcal{F}_2$,

$$(T^\Phi f)(Y) = \frac{1}{D_m} \int_{X \in \mathcal{X}} D(Y, X) K_T(Y, X) f(X) dX. \quad (\text{III.9})$$

From this definition, we can write

$$d \|Tf\|_2 \leq \|T^\Phi f\|_2 \leq D_m \|Tf\|_2.$$

Then the injectivity of T^Φ is proven by contradiction as a consequence of the injectivity of T' .

Proposition III.2.2. The following sequence converges towards f

$$f^{n+1} = f^n + T^{-1} \circ T^\Phi (f - f^n) \quad \text{with} \quad f^0 = 0.$$

Proof. To prove the convergence of this algorithm, we have to show that the error tends towards 0, i.e.

$$|f^{n+1} - f^n| \xrightarrow{n \rightarrow +\infty} 0_{\mathcal{F}_1} . \quad (\text{III.10})$$

This error can be written

$$\begin{aligned} f^{n+1} - f^n &= T^{-1} \circ T^\Phi (f - f^n) \\ &= T^{-1} \circ T^\Phi ((f - f^{n-1}) - (f^n - f^{n-1})) \\ &= (f^n - f^{n-1}) - T^{-1} \circ T^\Phi (f^n - f^{n-1}) \\ &= (Id_{\mathcal{F}_1} - T^{-1} \circ T^\Phi) (f^n - f^{n-1}) \\ &= (Id_{\mathcal{F}_1} - T^{-1} \circ T^\Phi)^n (f^1) . \end{aligned} \quad (\text{III.11})$$

Providing our space with the \mathcal{L}_2 -norm and defining the norm of the operator T as :

$$|||T||| = \sup_{f \in \mathcal{F}_1} \frac{\|Tf\|_2}{\|f\|_2} , \quad (\text{III.12})$$

we have by the inequality of Cauchy-Schwartz,

$$\|f^{n+1} - f^n\|_2 \leq |||Id_{\mathcal{F}_1} - T^{-1} \circ T^\Phi||| \|f^1\|_2 . \quad (\text{III.13})$$

To prove the convergence is equivalent to prove

$$|||Id_{\mathcal{L}_+^2(\mathcal{X})} - T^{-1} \circ T^\Phi||| < 1 . \quad (\text{III.14})$$

Now we can notice that $T^{-1} \circ T = Id_{\mathcal{F}_1}$ so

$$Id_{\mathcal{F}_1} - T^{-1} \circ T^\Phi = T^{-1} \circ (T - T^\Phi) . \quad (\text{III.15})$$

For $f \in \mathcal{F}_1$, we have

$$(T^{-1} \circ (T - T^\Phi)) f = T^{-1} \left(\int_{\mathcal{X}} \left(1 - \frac{D(Y, X)}{D_m} \right) K_T(Y, X) f(X) dX \right) . \quad (\text{III.16})$$

Therefore it exists a constant M such that

$$\left(1 - \frac{D(Y, X)}{C} \right) \leq M = 1 - \min_{(X, Y) \in \mathcal{X} \times \mathcal{Y}} \left\{ \frac{D(Y, X)}{C} \right\} < 1 . \quad (\text{III.17})$$

In this case,

$$\begin{aligned} (T^{-1} \circ (T - T^\Phi)) f &\leq M \times T^{-1} \left(\int_{\mathcal{X}} K_T(Y, X) f(X) dX \right) , \\ &\leq M \times f \end{aligned} \quad (\text{III.18})$$

and so

$$|||Id_{\mathcal{F}_1} - T^{-1} \circ T^\Phi||| \leq M^2 < 1 , \quad (\text{III.19})$$

which ensures the convergence. Assuming the convergence of the algorithm, we have to prove that the solution is the original function. At convergence, we have :

$$f^{n+1} - f^n = T^{-1} (T^\Phi (f - f^n)) = 0 . \quad (\text{III.20})$$

The injectivity of operators implies the unicity of the solution :

$$T^{-1} (T^\Phi (f^{n+1} - f^n)) = 0 \implies T^\Phi (f - f^n) = 0 \implies f^n = f . \quad (\text{III.21})$$

□

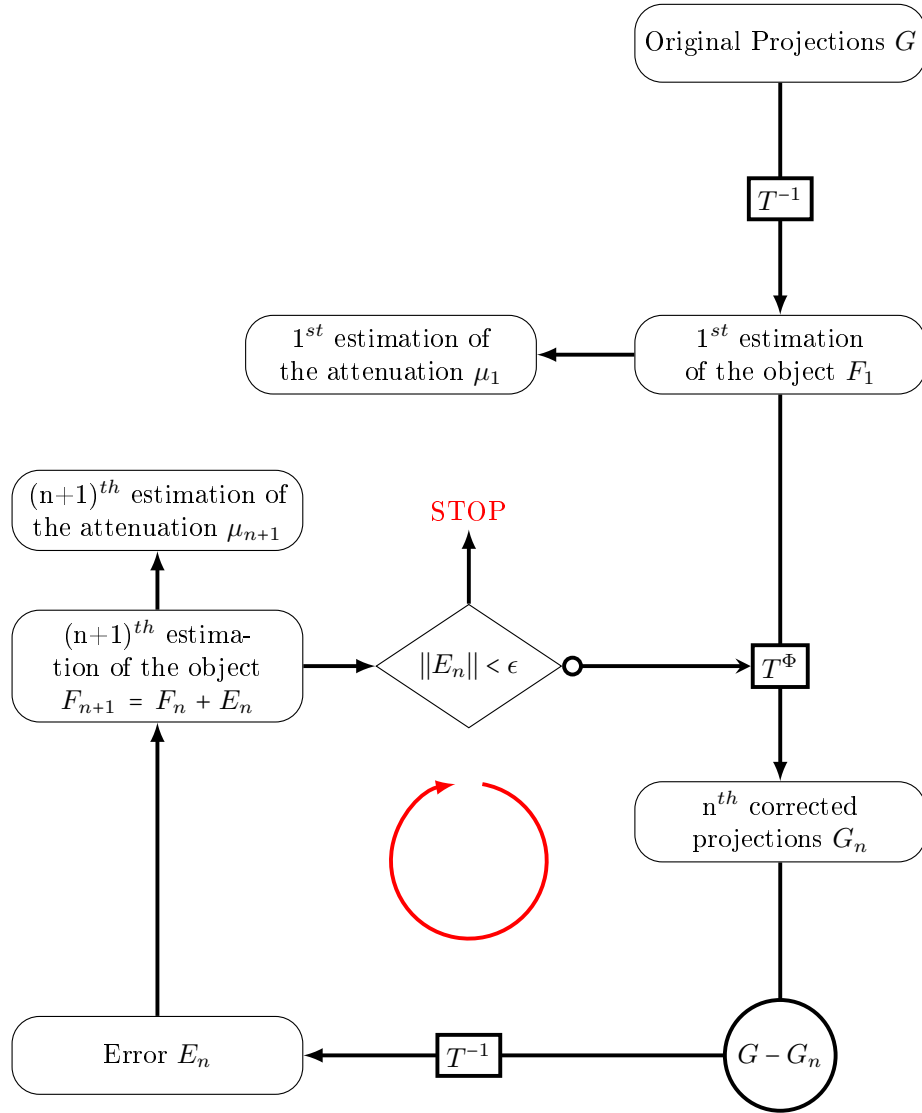


Figure III.1: Algorithm GIPC

Remark III.2.3. *The proof remains true if we consider the following corrected distorted operator*

$$T_c^\Phi : f(X) \longrightarrow g(Y) = \frac{T^\Phi f(Y)}{C(Y)} = D_m \frac{T^\Phi f(Y)}{\max_{X \in \mathcal{X}} \{D(Y, X)\}} . \quad (\text{III.22})$$

instead of T^Φ .

In a general context, it is difficult to have all these assumptions fulfilled. But if we consider the problem of attenuation correction in our generalized Radon transforms, the function to reconstruct is positive, the kernel operators are positive and the distortion function verifies $\forall (X, Y) \in \mathcal{X} \times \mathcal{Y}$, $0 < D(Y, X) \leq 1$.

Of course in a numerical approach, the reconstruction results could have some negative artifacts. To ensure the convergence and the unicity of the algorithm, we have so to erase this negative artifacts at each step.

Remark III.2.4. *In the state-of-the-art [38], we take*

$$C(Y) = \frac{1}{\Omega_{\mathcal{X}}} \int_{X \in \mathcal{X}} D(Y, X) dX . \quad (\text{III.23})$$

Of course this case can be considered only in compact spaces to have a finite space volume, $\Omega_{\mathcal{X}}$. In this case the absolute convergence is difficult to prove. Nevertheless this choice can be explained by convergence in probability. If we consider the following event,

$$\left(1 - \frac{D(Y, X)}{C(Y)}\right)^2 < 1 , \quad (\text{III.24})$$

thus the inequality of Markov gives us the interval of the probability of this event

$$1 \geq \mathcal{P} \left(\left(1 - \frac{D(Y, X)}{C(Y)}\right)^2 < 1 \right) \geq 1 - \frac{1}{\Omega_{\mathcal{X}}} \int_{X \in \mathcal{X}} \left(1 - \frac{D(Y, X)}{C(Y)}\right)^2 dX . \quad (\text{III.25})$$

The upper bound of the right term of this inequality is obtained, in the meaning of the least squares, for

$$C(Y) = \frac{1}{\Omega_{\mathcal{X}}} \int_{X \in \mathcal{X}} D(Y, X) dX . \quad (\text{III.26})$$

III.2.2 Application for inverting the attenuated CART_2

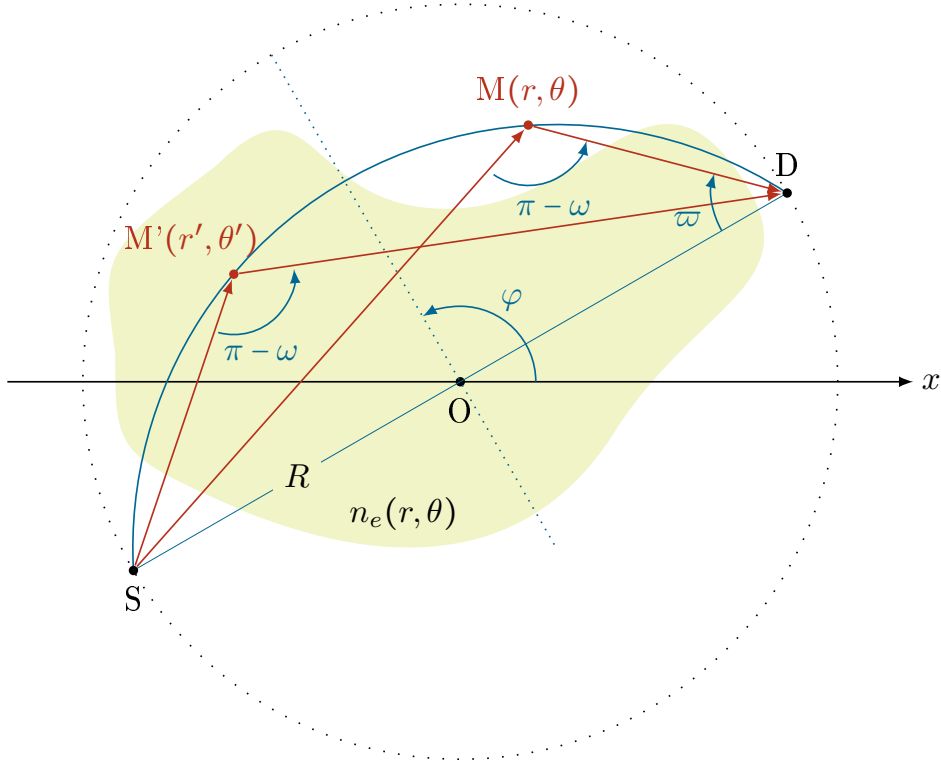


Figure III.2: Flight of detected photons in the CART_2

III.2.2.a Mathematical expression of the attenuated CART_2

We want now to add the attenuation factor in the modeling of our transform. Then taking into account physical phenomenon implies to change the forward CART . We can notice 2 steps :

- a photon is emitted by the source \mathbf{S} and travels to a scattering site \mathbf{M} , then it is subjected to an attenuation factor $\mu_0 = \mu(E_0)$,
- this scattered photon travels to the detecting point, \mathbf{D} , and then it is subjected to an attenuation factor $\mu_\tau = \mu(E_k)$ with E_k , the scattered energy.

Thus radiation is affected by medium attenuation and by dispersion due to photometric propagation effects. These phenomena can be taken into account by multiplying the integrand of the circular-arc Radon transform of eq. (II.69) by the following factor

$$\frac{e^{-\int_{\overline{\mathbf{SM}}} \mu_0(r, \theta) dl}}{\overline{\mathbf{SM}}^2} \frac{e^{-\int_{\overline{\mathbf{MD}}} \mu_\tau(r, \theta) dl}}{\overline{\mathbf{MD}}^2} ,$$

where μ_0 (resp. μ_τ) is the linear attenuation map at the energy of the primary radiation (resp. at the energy of the scattered radiation), \mathbf{S} is the emitting point, \mathbf{M} is the scattering point and \mathbf{D} is the detected point. Moreover the Compton effect is described by the Klein-Nishina differential cross section which gives the probability for a photon to be scattered and has to be taken into account.

We have

$$\overline{\mathbf{SM}}^2 \overline{\mathbf{MD}}^2 = (R^2 - r^2)^2 (1 + p^2) ,$$

therefore \mathcal{C}^2 takes the physical form $\mathcal{C}^{2\Phi}$, defined as

$$\mathcal{C}^{2\Phi} n_e(p, \varphi) = \frac{\beta P (\tan^{-1}(p))}{(1 + p^2)} \int_{\varphi - \frac{\pi}{2}}^{\varphi + \frac{\pi}{2}} \int_0^{R - \epsilon} f(r, \theta) \mathbf{A}(\varphi, p|r, \theta) \mathcal{K}_{\mathcal{C}^2}(\varphi, p|r, \theta) \frac{r}{(R^2 - r^2)^2} dr d\theta , \quad (\text{III.27})$$

where ϵ is a prescription to avoid divergence when $r \rightarrow R$, β represents physical constants and

$$\mathbf{A}(\varphi, p|r, \theta) = \exp\left(-\int_0^{t_1} \mu_0(\mathbf{x}_S + t\mathbf{d}_1) dt\right) \cdot \exp\left(-\int_0^{t_2} \mu_\tau(\mathbf{x}_M + t\mathbf{d}_2) dt\right) ,$$

with

$$\left\{ \begin{array}{l} \mathbf{x}_S = -\mathbf{x}_D = (-R \sin \varphi, R \cos \varphi) \\ \mathbf{x}_M = (r \cos \theta, r \sin \theta) \\ \mathbf{d}_1 = (\cos(\omega - \varpi + \varphi - \pi/2), \sin(\omega - \varpi + \varphi - \pi/2)) \\ \mathbf{d}_2 = (\cos(\varphi - \varpi - \pi/2), \sin(\varphi - \varpi - \pi/2)) \\ t_1 = (r \sin \theta - R \cos \varphi) / \sin(\omega - \varpi + \varphi - \pi/2) \\ t_2 = -(R \cos \varphi + r \sin \theta) / \sin(\varphi - \varpi - \pi/2) \\ \varpi = \frac{\pi - \theta + \varphi}{2} + \arctan\left(\frac{r - R}{r + R} \cot\left(\frac{\theta - \varphi}{2}\right)\right) . \end{array} \right.$$

Without $\mathbf{A}(\varphi, p|r, \theta)$, the physical forward transform is still invertible since we can pass from eq. (III.27) to eq. (II.69) by the following change of function,

$$\mathcal{C}^2 f(p, \varphi) = \frac{1 + p^2}{\beta P (\tan^{-1}(p))} \mathcal{C}^{2\Phi} n_e(p, \varphi) \quad \text{and} \quad f(r, \theta) = \frac{n_e(r, \theta)}{(R^2 - r^2)^2} .$$

The studies of \mathcal{C}^2 and $\mathcal{C}^{2\Phi}$ are so equivalent. But if we consider the attenuation factor $\mathbf{A}(\varphi, p|r, \theta)$ we do not know for the moment how to invert $\mathcal{C}^{2\Phi}$. Therefore an attenuation correction has to be applied. Thus we propose to use the GIPC algorithm derived above to perform such a correction.

III.2.2.b Simulation results

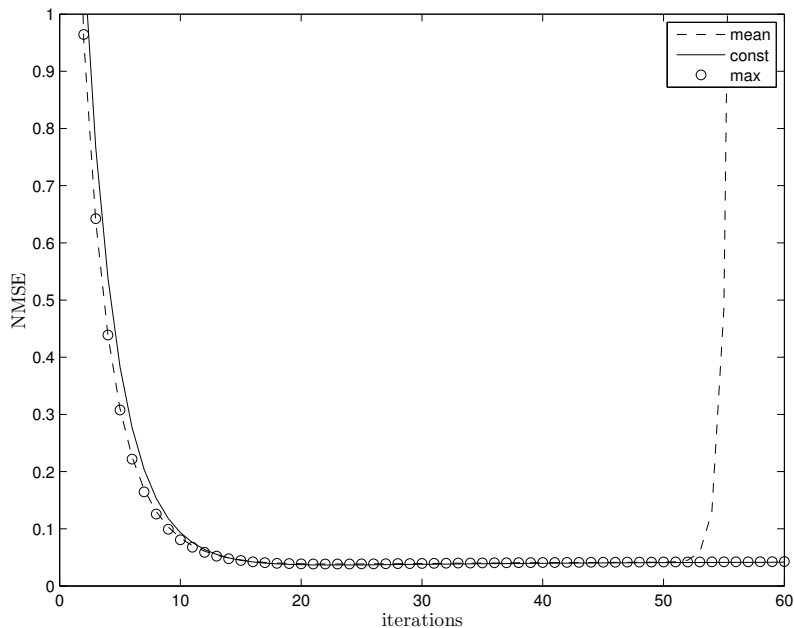


Figure III.3: Normalized mean square error in three cases vs iterations.

We have performed numerical simulations on the Zubal phantom [77] which represents the thorax. The iterations are stopped when the Normalized Mean Square Error (NMSE) is small enough. The attenuation map is assumed known.

The scattering medium is discretized with 128×128 pixels. We consider the number of detector positions N_φ and the number of energy levels N_ω . In order to have a "well-conditioned" problem, the number of projections ($N_\varphi \times N_\omega$) must be larger than or equal to the number of image pixels (N^2). This is why we take $N_\omega = N_\varphi = 4N$. Moreover let $p = N$ and $\min\{w\} = d\omega$.

Reconstruction (Figure III.4(a)) is obtained in the case of $C = \max_{(X,Y) \in \mathcal{X} \times \mathcal{Y}} \{D(Y, X)\}$, and its image quality and the accuracy of the small structure appear sufficient for medical diagnosis.

Figure III.3 shows the normalized mean square error in terms of iterations in three cases :

1. $C = \max_{(X,Y) \in \mathcal{X} \times \mathcal{Y}} \{D(Y, X)\}$,
2. $C(Y) = \max_{X \in \mathcal{X}} \{D(Y, X)\}$,
3. $C(Y) = \frac{1}{\Omega_{\mathcal{X}}} \int_{X \in \mathcal{X}} D(Y, X) dX$.

For these three correction functions, the behaviour of the convergence is typically the same. But if we iterate the algorithm longer, the algorithms will diverge because of numerical approximations. In particular because numerically, $T^{-1} \circ T \neq Id$. Especially the mean is the one that diverges the soonest and so which is the most unstable. To avoid the divergence, relaxation parameters have to be added in the algorithm.

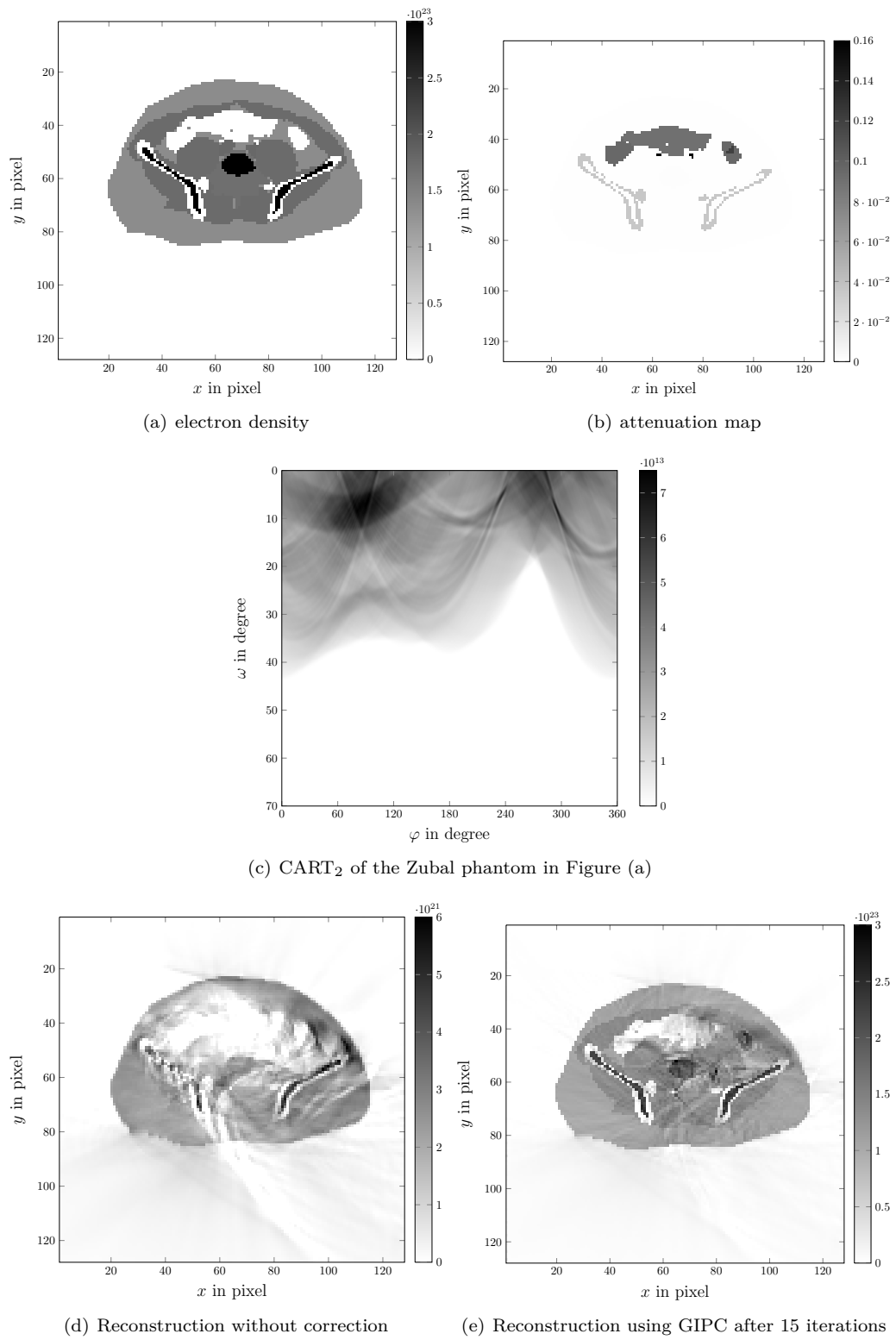


Figure III.4: Reconstruction of the Zubal phantom from CART_2 data

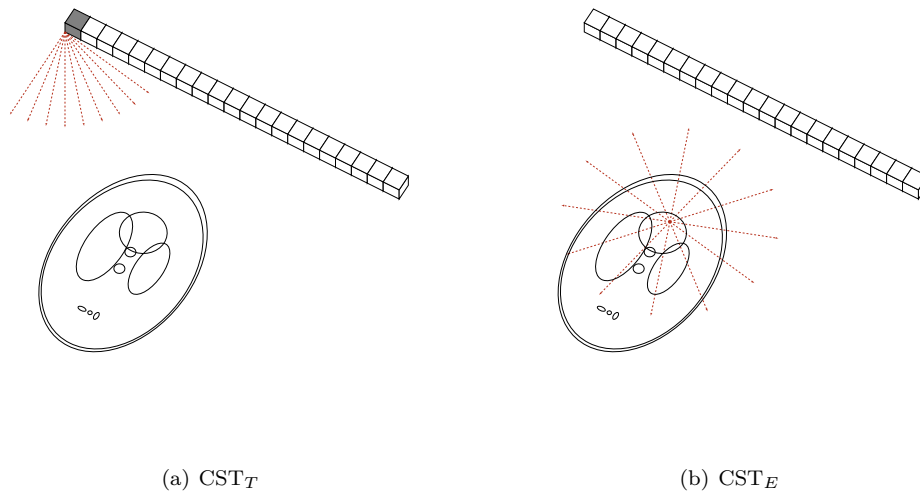


Figure III.5: Representation of both modalities on CST for a same slice.

III.3 A novel bimodal system based on scattered radiation

III.3.1 A new concept

In this part, we propose a new concept of bimodality imaging based on Compton scattering tomography modalities similar to the PET/CT system in the sense that it combines transmission and emission modalities. In our novel imaging system, we consider two CST modalities. The first one works in transmission (CST_T), the modeling of its image formation is based on a circular-arc Radon transform ($CART_1$). The second one works in emission (CST_E), it is based on a compounded V-line Radon transform (CVRT).

The concept is depicted in Fig. III.5. Considering a slice, measurements are divided in two steps :

- **First CST_T** : By transmission a source illuminates the slice and detectors located at a rail collect scattered photons in terms of energy.
- **Then CST_E** : The radioactive area inside the object emits photons which are scattered and detected with respect to their scattering energy.

Hence a patient is submitted to two examinations in order to recover three information maps : the electron density, the attenuation map and the activity (tracer), see Fig. III.6.

Image quality in functional imaging is still a major issue in the medical research domain [34, 59]. In this context, the proposed system aims to increase image quality in emission tomography through the use of the single scattered radiation (which represents 80% of the emitted radiation) and suited correction algorithm. Another interest of this combination is that both modalities allow a two-dimensional image reconstruction from any scattered radiation collected by a one-dimensional collimated non-moving camera. This involves a new concept of detector with high energy resolution able to collect the scattered radiation.

The physics of the Compton effect allows the reconstruction of the electron density which is linked to the attenuation map and thus contributes to the modelling of emission CST. This shows the complementarity of the two CST modalities.

The electron density n_e of a studied object is non constant, and this has a huge impact on emission CST to such an extent that it is impossible to reconstruct a coherent activity map. Fortunately the reconstruction of the electron density map is provided by the transmission CST,

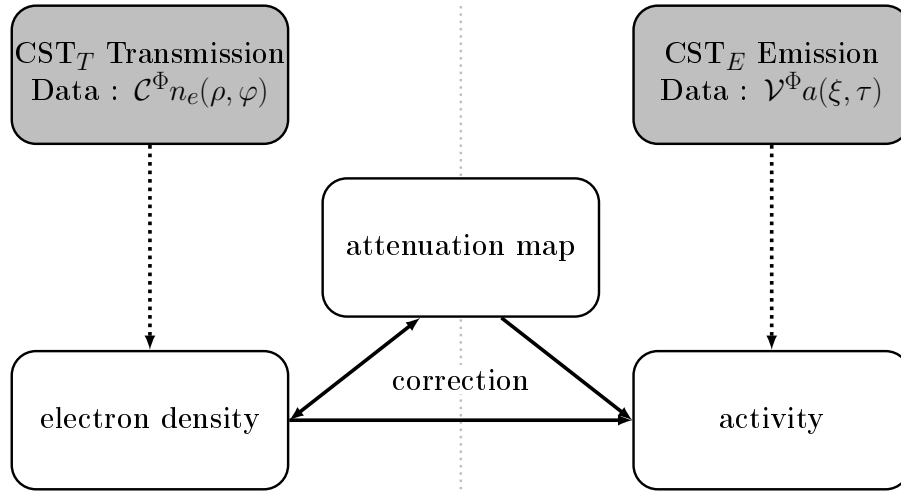


Figure III.6: Concept of a novel bimodal system

therefore we use it as a prior information for the correction of the second CST reconstruction. Moreover, one create the rough attenuation map linked to the electron density and use it in an attenuation correction iterative algorithm. The main idea of this algorithm is the creation of an attenuation map to correct the electron density, which will create a new attenuation map and iterate this algorithm until the convergence of the algorithm is reached. Also we use the final attenuation map to correct the map of the emission CST. In order to perform attenuation correction in both modalities, we use the GIPC algorithm presented above.

The section is organized as follows. First we deal with the theory of our Compton scattering tomography bimodality through the transmission one as proposed by Norton in 1994 [49] and the emission one as proposed by Nguyen and Truong in 2011 [68]. Image formation is also introduced. Then we present the inversion of the original data, their attenuation and electron density correction through a suited correction algorithm, in which we take into account physical phenomena such as attenuation factor. Finally, we present new numerical results of the emerging CST system on a slice of the Zubal phantom [77].

III.3.2 Theory

III.3.2.a Compton scattering tomography modality based on Circular-Arc Radon transform (CART₁)

The working principle of Norton's modality [49] is given by Fig. III.7. In an idealized context (without attenuation and radiation spreading effects), in order to convey the basic idea, a point-like source **S** emits primary radiation towards an object, of which **M** is a scattering site (running point). Also a point-like detector **D** moves along an *Ox*-axis and collects, at given energy E_ω , scattered radiation from the object. The physics of Compton scattering requires that the registered radiation flux density $g(\mathbf{D})$ at site **D** is due to the scattering contribution of all scattering sites **M** lying on an arc of circle from **S** to **D** subtending an angle $(\pi - \omega)$, where ω is the scattering angle corresponding to the outgoing energy E_ω .

In the absence of attenuation Norton wrote down the expression of the received radiation flux density at **D** in \mathbb{R}^2 . As we want to take into account the attenuation factor in the modeling of the CART₁, we have to rewrite the projections $g(\mathbf{D})$ as

$$\mathcal{C}^\Phi n_e(\rho, \varphi) = \int_0^\pi \int_0^\infty n_e(r, \theta) \mathcal{K}_{\mathcal{C}^\Phi}(\varphi, \rho | r, \theta) w_{att}(\rho, \varphi, r, \theta) r dr d\theta \quad (\text{III.28})$$

with

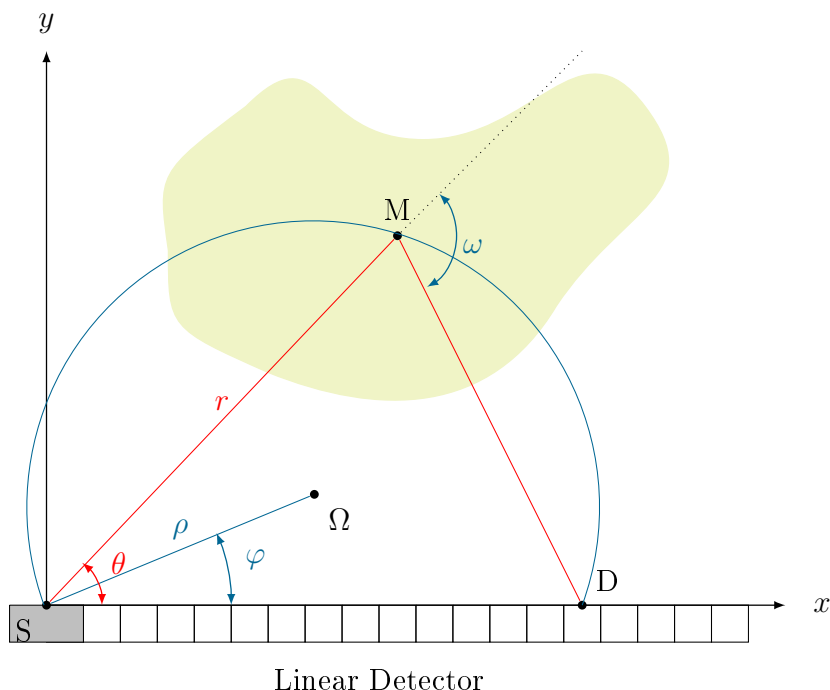


Figure III.7: Principle of Norton's modality of Compton scattering tomography

$$\mathcal{K}_{C^\Phi}(\varphi, \rho | r, \theta) = \frac{r^2 s(\theta) \sigma^c(\omega)}{4\pi (2\rho)^3 \sin^2 \theta} \delta[r - 2\rho \cos(\theta - \varphi)]$$

where $s(\theta)$ expresses any angular dependence of the gamma-ray source distribution, and $\sigma^c(\omega)$ is the Klein-Nishina differential cross section and

$$w_{att}(\rho, \varphi, r, \theta) = e^{-\int_0^r \mu_0(t \cos \theta, t \sin \theta) dt - \int_0^{r_1} \mu_\omega(r \cos \theta + t \cos(\omega - \theta), r \sin \theta + t \sin(\omega - \theta)) dt}, \quad (\text{III.29})$$

with $r_1 = \frac{r \sin \theta}{\sin(\theta - \omega)}$. Mathematically, $\mathcal{C}^\Phi n_e(\rho, \varphi)$ is essentially the Radon transform of the object electron density $n_e(r, \theta)$ on arcs of circle passing through a fixed point \mathbf{S} of equation $r = 2\rho \cos(\theta - \varphi)$.

The factor w_{att} cannot be separated in a product $w_1(r, \theta) \cdot w_2(\rho, \varphi)$ this is why the Cormack inversion procedure cannot be applied [12, 13]. For the moment, we do not know how to invert analytically the attenuated CART_1 . For this we propose an attenuation correction algorithm in order to compensate the attenuation factor.

III.3.2.b Compton scattering tomography modality by emission based on compounded \mathcal{V} -line Radon transform (CVRT)

The working principle of the CVRT [68] is given by Fig. III.8. In order to convey the basic idea, a 2D-object containing a non-uniform radioactivity source distribution emits primary radiation. Also a collimated linear static detector collects, at given energy E_ω , scattered radiation from the object with a direction parallel to that of the collimator holes. The physics of Compton scattering requires that the registered radiation flux density $g(\mathbf{D})$ at site \mathbf{D} is due to the sum of the contribution of all emitting object point sources located on two half-lines starting at a site \mathbf{M} and making an angle ω with the collimator axis direction, for all possible \mathbf{M} along the axis of the collimator at \mathbf{D} .

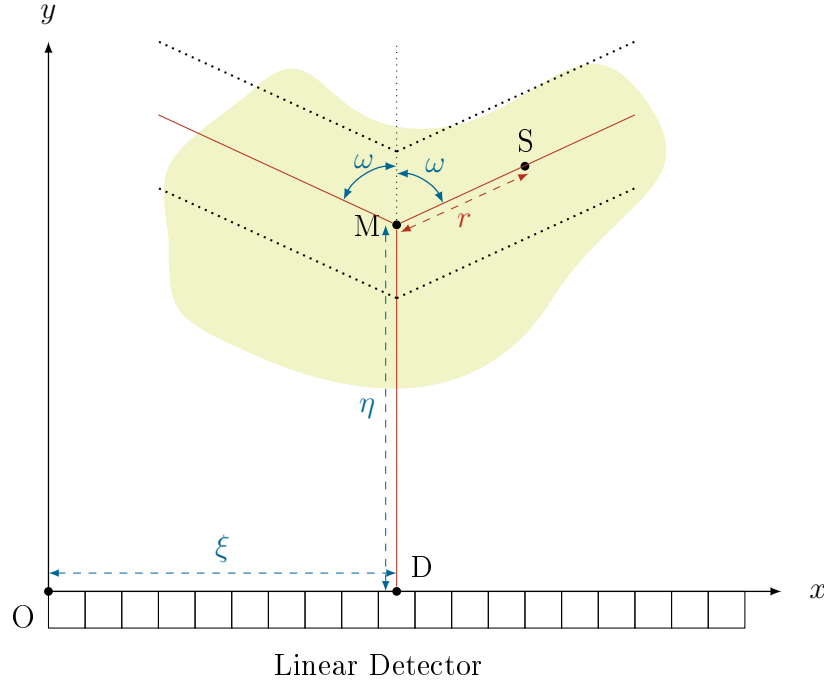


Figure III.8: Principle of compounded \mathcal{V} -line Radon transform and parameters setup

Let $a(x, y)$ be an activity density function. We consider the physical phenomena i.e. :

1. The photon flux is submitted to an attenuation map μ_0 between each internal source to the scattering points.
2. The probability of diffusion being proportional in the electronic density, it is necessary to take care of the non-homogeneous $n_e(\mathbf{M})$.
3. The spreading photon flux propagates up to the detector with a new scattering energy (see Compton formula) and so is attenuated by μ_ω .

With all these considerations, the measured photon flux density at \mathbf{D} under a scattering angle ω can be written as

$$\mathcal{V}^\Phi a(\xi, \tau) = P(\tau) \int_{\mathbb{R}^2} dx dy \mathcal{K}_\mathcal{V}(x, y|\xi, \tau) w_v^\phi(\xi, \eta, r) a(x, y), \quad (\text{III.30})$$

with $\tau = \tan(\omega)$,

$$\mathcal{K}_\mathcal{V}(x, y|\xi, \tau) = \frac{1}{4\pi^2} \frac{Y(y - |x - \xi|\tau)}{|x - \xi| y - |x - \xi|\tau}, \quad (\text{III.31})$$

and

$$w_v^\phi(\xi, \eta) = n_e(\xi, \eta) e^{-\int_0^\eta \mu_\omega(\xi, \eta') d\eta'} e^{-\int_0^r \mu_0(\xi + r' \sin \omega, \eta + r' \cos \omega) dr'} e^{-\int_0^r \mu_0(\xi - r' \sin \omega, \eta + r' \cos \omega) dr'}. \quad (\text{III.32})$$

Equation (III.30) stands for image formation but this form does not permit the inversion procedure without correcting the additional physical factors w_v^ϕ through a correction algorithm. Without this factor, we can use the inversion proposed in [68]. Nevertheless to avoid singularities, we consider that the object of interest is placed at a minimal distance from the detector. The global inversion algorithm will be present in the next section.

III.3.2.c Suited attenuation/electron density correction algorithm for both Radon transforms

Numerous methods for correcting the attenuation factor were proposed : for example the Generalized Chang Correction (GCC) which corrects the reconstructed function or the Iterative Pre Correction (IPC) which corrects data, see [38]. Nevertheless these algorithms need the attenuation map. Here we cannot have this information since we want to recover the attenuation map from the electron density. To avoid such assumption we propose an alternative IPC algorithm in which the attenuation map is obtained iteratively from the electron density making the assumption that we know the kind of the medium and so the corresponding total cross section. Thus an approximated attenuation map is deduced from the approximated electron density and is used to correct the data. We iterate until convergence of the algorithm is reached.

In this part we denote by T the operator \mathcal{C}^1 (resp. \mathcal{V}) and by $(\mathcal{X}, \mathcal{Y})$, the measurable space $(\mathbb{R}^+ \times [0, \pi], \mathbb{R}^+ \times [0, 2\pi])$ (resp. $(\mathbb{R}^+ \times \mathbb{R}^+, \mathbb{R}^+ \times [0, \pi])$). Then the algorithm we proposed ensures that the following recurrence relation converges towards f

$$f^{n+1} = f^n + T^{-1} \circ T^\Phi (f - f^n) \quad \text{with} \quad f^0 = 0. \quad (\text{III.33})$$

In the case of the \mathcal{C}^1 , the injectivity was proved by the establishment of its singular value decomposition Corollary II.2.2. And for the \mathcal{V} the proof of its injectivity was given in [68]. This algorithm requires an analytical inversion of the mathematical modeling of our modalities. We give these inversion formulas below.

III.3.2.d CART_1 : Inversion formula via circular harmonic decomposition

Norton worked out an inverse formula [49] which can be interpreted as a back-projection procedure on arcs of circle and not on straight lines as in the case of classical Radon transform. Norton produced also numerical simulations to validate his modality first without attenuation effects. In a next step he also developed related numerical algorithms in which he took approximately into account the attenuation in matter for a point object [49]. His results have appeared as quite convincing.

In our study, we will use a different reconstruction. Based on Cormack's works [12, 13], it produces a consistent reconstructed image in the circular harmonic components domain. To invert this transform, we cannot take into account the attenuation factor.

We start from equation (III.28). Let :

$$\begin{cases} \mathcal{C}f(p, \varphi) &= \mathcal{C}^\Phi n_e\left(\frac{p}{2}, \varphi\right) \frac{p^4}{P(\varphi + \pi/2)} \\ f(r, \theta) &= n_e(r, \theta) \frac{bs(\theta)r}{8\pi \sin^2 \theta}. \end{cases} \quad (\text{III.34})$$

Substituting equation (III.34) in (III.28) we obtain:

$$\mathcal{C}f(p, \varphi) = \int_0^\pi d\theta \int_0^{+\infty} dr p f(r, \theta) \delta\{r - p \cos(\theta - \varphi)\}.$$

This equation gives the integral of a function $f(r, \theta)$ on a class of circles having a fixed common point of equation $r = p \cos(\theta - \varphi)$ and defined by the integral kernel support in (r, θ) -space. This equation belongs to the β -curve ($\beta = 1$) family of [12] and so is suitable for circular harmonic decomposition. This is why the inverse transform can be worked out using the Fourier angular components of f and $\mathcal{C}f$.

$$f_l(r) = \frac{1}{\pi r} \int_0^r \frac{e^{-|l| \cosh^{-1}(r/p)}}{\sqrt{\left(\frac{r}{p}\right)^2 - 1}} (\mathcal{C}f_l)'(p) dp - \frac{1}{\pi r} \int_r^{+\infty} U_{|l|-1}(r/p) (\mathcal{C}f_l)'(p) dp \quad (\text{III.35})$$

where $U_{l-1}(\cos x) = \sin lx / \sin x$ is the Tchebychev polynomial of second kind. Finally $f(r, \theta)$ is reconstructed through its Fourier expansion with the circular harmonic components $f_l(r)$. Thus by a change of functions (eq (III.34)), we can study the modelling of the Norton's CST as the inversion of the transform \mathcal{C} in the (p, φ) -space.

III.3.2.e CVRT : Inversion formula

The proposed algorithm needs the analytical inversion of the modelling of the CST_E without attenuation then the Klein-Nishina scattering probability in Compton effect is discarded. Let us define

$$h(x, y) = \int_0^{+\infty} \frac{d\eta}{2\pi\eta} a(x, \eta + y) .$$

The inversion of the CVRT has been established in [68] and the inversion formula is :

$$a(x, y) = \int_{-\infty}^{+\infty} \int_{-\infty}^{+\infty} \frac{e^{2i\pi q(y-z)} h(x, z)}{\gamma + i\frac{\pi}{2} \text{sgn}(q) - \ln(2\pi|q|)} dz dq \quad (\text{III.36})$$

with

$$h(x, z) = \frac{z}{\pi} \int_0^{\frac{\pi}{2}} p.v. \left(\int_{\mathbb{R}} \frac{\mathcal{V}\tilde{a}(u, \omega)}{u - x \cos \omega \pm z \sin \omega} du \right) \frac{d\omega}{\cos \omega} + \frac{z}{\pi} \int_0^{\infty} p.v. \left(\int_{\mathbb{R}} \frac{\mathcal{V}a(\xi, -\tau)}{\xi - x \pm z\tau} d\xi \right) d\tau , \quad (\text{III.37})$$

putting $\omega = \arctan \tau$, $u = \xi \cos \omega$ and $\mathcal{V}\tilde{a}(u, \omega) = \mathcal{V}a(\xi, \tau)$. As this expression can be rewritten as a simple backprojection over corresponding broken lines convolved with a filter, it does not need a computational regularisation.

III.3.3 Correction algorithm description

For a realistic image (activity) reconstruction based on the inverse CVRT (eq. (III.36)), the emission data acquired in VEI needs to be corrected by inhomogeneous electron density and attenuation. The principle is then to reconstruct the electron density through a correction of the attenuation factor in the Norton's CST. In the context of medical applications, we can use a prior information about the studied image. Thus we assume that the studied organ (in terms of attenuation) is composed of known substances. As we do not know the attenuation map, we approximate it from the electron density at each step. Thus thanks to the following relation

$$\mu_E(\mathbf{M}) = \sigma_E(\mathbf{M}) \cdot n_e(\mathbf{M}), \quad (\text{III.38})$$

with $\mu_E(\mathbf{M})$, the linear attenuation factor for a radiation of energy E at \mathbf{M} , $\sigma_E(\mathbf{M})$ the total cross-section of the matter at \mathbf{M} for a radiation of energy E and $n_e(\mathbf{M})$ the electron density at \mathbf{M} , we can process to a K-means clustering to deduce an approximation of the attenuation map from the electron density. We can then update the distortion kernel which defines the operator \mathcal{C}^ϕ and apply a correction of the attenuation factor, see Algorithm 1.

When the electron density and the non uniform attenuation map are established, eq. (III.30) gives the real emission data, *i.e.* the image formation of the activity density of the object. However such an attenuated V-line Radon transform does not possess an inverse at hand. It is necessary to correct the non constant electron density and the non uniform attenuation in the emission data before recovering the activity map by eq. (III.36). This procedure is iteratively carried out until convergence is reached. (see Algorithm 2). The parameter ϵ is an object-dependent threshold.

In both algorithms, N^n, S^n, M^n, A^n are the corresponding matrices of $n_e(\cdot)$, $\sigma_E(\cdot)$, $\mu_0(\cdot)$, $a(\cdot)$ at iteration n and G is respectively the original data for CART_1 and CVRT.

At last we obtain an approximated reconstruction of three informations of the studied medium : the electron density, the attenuation map and the activity, through a novel bimodal system based on scattered radiation. In the next section, we present simulation results.

Algorithm 1 μ_0 correction algorithm for CART₁

```

Input  $G$  (Norton's CST data),  $d$  and  $T^{-1}$ 
 $G \leftarrow G/d$ 
 $N^1 \leftarrow T^{-1}(G)$ 
 $S^1 \leftarrow$  K-mean algorithm on  $N^1$  %% total cross-section
 $M^1 \leftarrow S^1 \times N^1$ 
 $T^\phi$  is updated
while  $e^{n-1} - e^n > \epsilon$  do
   $G^n \leftarrow T^\phi(N^n)$ 
   $N^{n+1} \leftarrow N^n + d^{-1}T^{-1}(G^n - G)$ 
   $S^n \leftarrow$  K-mean algorithm on  $N^n$ 
   $M^n \leftarrow S^n \times N^n$ 
   $T^\phi$  is updated
   $n \leftarrow n + 1$ 
end while
return  $N^n, M^n$  %%  $n_e$  and  $\mu_0$ 

```

Algorithm 2 n_e and μ_0 correction algorithm for CVRT

```

Input  $G$  (VEI data),  $d, T^\phi$  and  $T^{-1}$ 
 $G \leftarrow G/d$ 
 $A^1 \leftarrow T^{-1}(G)$ 
while  $e^{n-1} - e^n > \epsilon$  do
   $G^n \leftarrow T^\phi(A^n)$ 
   $A^{n+1} \leftarrow A^n + d^{-1}T^{-1}(G^n - G)$ 
   $n \leftarrow n + 1$ 
end while
return  $A^n$  %%  $(a)$ 

```

III.3.4 Simulation studies

We propose to test our approach on a slice of the Zubal phantom [77] which represents the thorax Fig. III.9. The aim of this experiment is to detect a cardiac biodistribution. We use the Hounsfield scale to deduce from water the electron density and the attenuation coefficient of a given matter at a given energy. Moreover we try to detect tumorous lesions by introducing a tracer into the body. The activity is equal to 13MBq and the value HU (Hounsfield unit) is equal to 50.

We just consider 7 kind of substances : air, water, lung, bone (for organ categories 5 and 11), muscle (for organ categories 6 and 8), blood and tissue (for organ categories 2 and 9).

The scattering medium is discretized with 128×128 pixels. We consider the number of detector positions (N_x, N_φ) and the number of energy levels N_ω . In order to have a "well-conditioned" problem, the number of projections $(N_x \times N_\omega, N_\varphi \times N_\omega)$ must be larger than the number of image pixels (128×128). As the measurement space is very large (because the system does not work with rotation around the body), we have to take a very large number of projections, this is why we choose $N_x = N_\varphi = N_\omega = 512$. This leads to the choice of scattering angular sampling step $\Delta\omega = 0.53^\circ$, which means, by differentiating the Compton energy formula and averaging over the scattering angle, an energy resolution of $\Delta E = 1.5eV$ for the most commonly used radionuclide (^{99m}Tc) having an energy $E_0 = 140keV$ (or $\Delta E = 10eV$ for $E_0 = 511keV$). If $N_\omega < 512$, the required energy resolution may be larger, but the resulting image resolution is reduced.

It should be noted that no desampling is applied in the following numerical results. The high order of the resolution $(N_x, N_\varphi, N_\omega)$ is due to non-compact data space. As such, we had to increase the sampling to guarantee a solution for the studied inverse problem.

Fig. III.10(a) shows the computation of the forward modeling of the measurement obtained for the studied medical phantom (Fig. III.9). These data follows the shape of the point spread



Figure III.9: Slice of the Zubal phantom

function given by the integral kernel, $\mathcal{K}_{\mathcal{C}^*}(\varphi, \rho|r, \theta)$.

We present now the results of numerical data set simulation (see Fig. III.10(b)) for our experiment protocol. We note the characteristic shape of the V-lines Radon transform, i.e. a form of "V" slightly curvilinear for high values of scattering angle with an intensity leveling off when the angle increases which is coherent with the PSF function.

Before to apply the correction algorithm, we give the reconstructions of the electron density (Fig. III.10(c)) and of the activity (Fig. III.10(d)) of the thorax phantom obtained without correction. Since photon emission process follows Poisson's law, this phenomenon is one of the main cause of degradation of the quality of image reconstruction in Compton scattering tomography. Thus the projections become in both cases $\tilde{g}(\mathbf{t}) \sim \mathcal{P}(Tf(\mathbf{t}))$ where \mathcal{P} stands for the Poisson law.

Here we study the robustness of our algorithms taking into account this phenomenon. The denoising is performed for the results presented below using the suited Poisson noise algorithm shown in [67].

III.3.5 Results

We follow the scheme presented in Fig. III.6. So we first reconstruct the electron density, then the attenuation map is deduced from the first approximation of n_e and we iterate the proposed correction algorithm (eq. (III.33)) to obtain final n_e and attenuation map. Once the first algorithm performed (representing the CST_T), we reconstruct the activity and we correct it by using the proposed correction algorithm, the attenuation map and n_e .

To assess the quality of the reconstructions, we use the NMSE which represents a good criterion for convergence of our iterative algorithm. Thus we stop the iterations when the difference of NMSE between two iterations is smaller than 0.1%.

For our simulations, we considered noise with a SNR of 20-30 dB. Indeed, to keep the inversion problem feasible multiple scattering was ignored. This phenomenon will act as additional noise in our simulations. The choice of 20 or 30 dB is realistic in tomographic imaging applications but further investigations should focus on evaluating the impact of various magnitudes of noise.

Fig. III.13 shows the reconstructions of the thorax phantom shown in Fig. III.9. We use the measurements shown in Fig. III.10(a) for CART_1 and in Fig. III.10(b) for CVRT but with different SNR. Reconstructions in Fig. III.13 show a good quality for the electron density and the activity. Fig. III.12 gives the NMSE in terms of iterations. We can see the interest of our method in terms of quality of reconstruction but in terms of magnitude too. In the case of the CVRT, the initial error is very important (because of the electron density that we do not take into account).

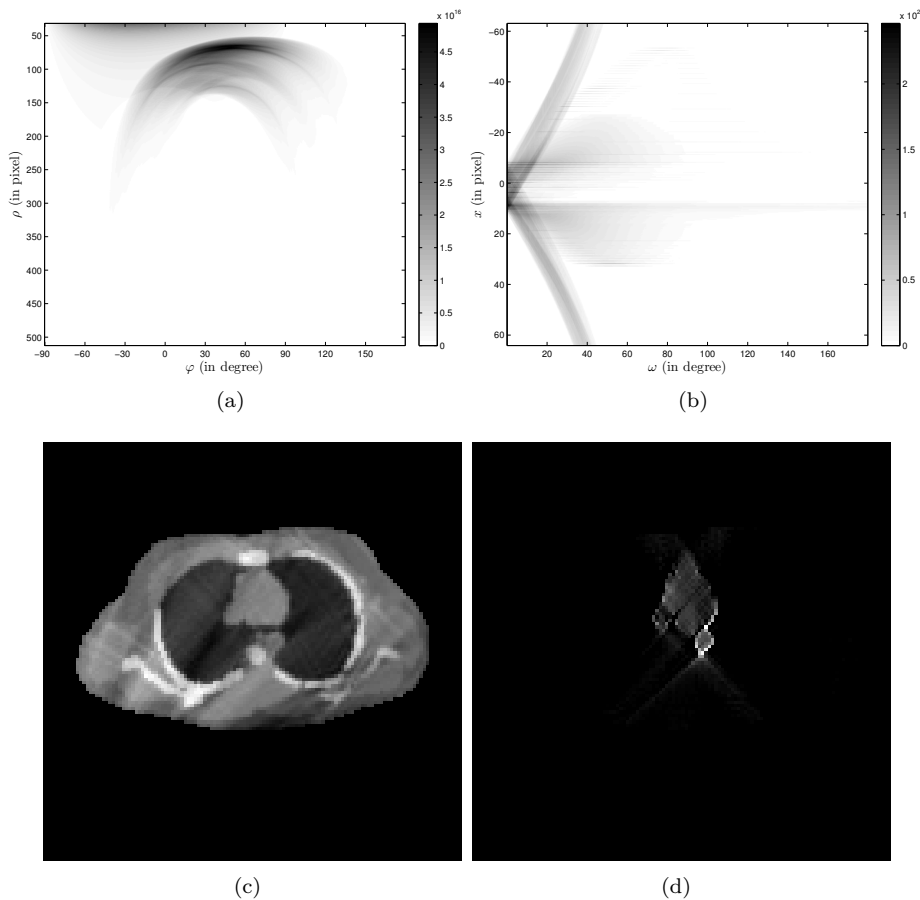


Figure III.10: $CART_1$ (a) and CVRT (b) of the phantom shown in figure III.9. Reconstruction of the electron density (c) and activity distribution (d) using equations (III.35) and eq (III.36), respectively, without noise and correction

Nevertheless the correction algorithm permits to decrease drastically the NMSE, even for a noise of 20 dB. In the case of the $CART_1$, the initial error is less important (only the attenuation is not taken into account) and the algorithm permits to obtain good NMSE.

The proposed algorithm makes use of the original algorithm to invert the projection data without considering attenuation. Both algorithms have been compared on the same datasets to demonstrate the benefit of the novel algorithm (see NMSE curves). Mathematically, the derivation presented in appendix A shows that the proposed algorithm applied on attenuated data tends towards the reconstruction obtained using the original algorithm on unattenuated data. Thus, we can compare them with those obtained without attenuation (see Figs. III.11(c) and III.11(d)). One can notice the good agreement between the results, which proves numerically the good convergence of our algorithm.

In this work, only single scattering was considering assuming that higher order scattering occurs with much smaller probability going as the power of the Klein-Nishina probability [74]. As such the effects of higher order scattering may be assimilated to noise fluctuations. As mentioned earlier, the spatial and energy resolutions required for implementation of this approach are not yet achievable with current imaging devices. However, it is anticipated that future advances in detector technology will enable the design and fabrication of systems having the required performance characteristics.

These experiments prove the theoretical feasibility and the interest of this approach in medical applications.

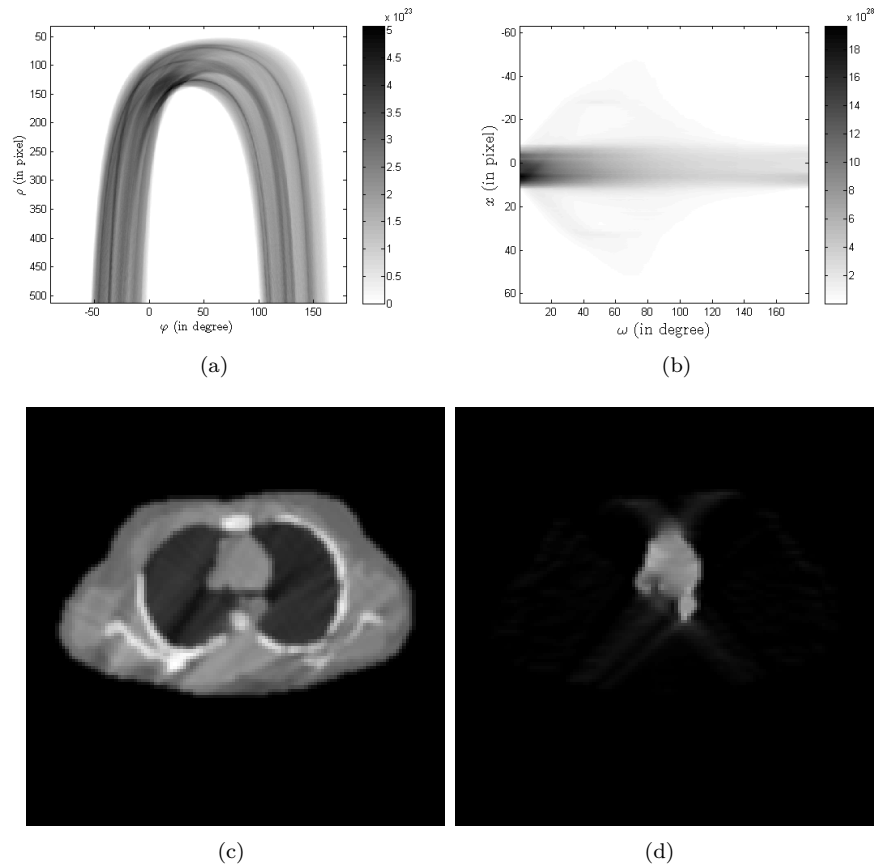


Figure III.11: $CART_1$ (a) and CVRT (b) of the phantom shown in figure III.9 without attenuation. Reconstruction of the electron density (c) and activity distribution (d) with the analytical inversion formulae.

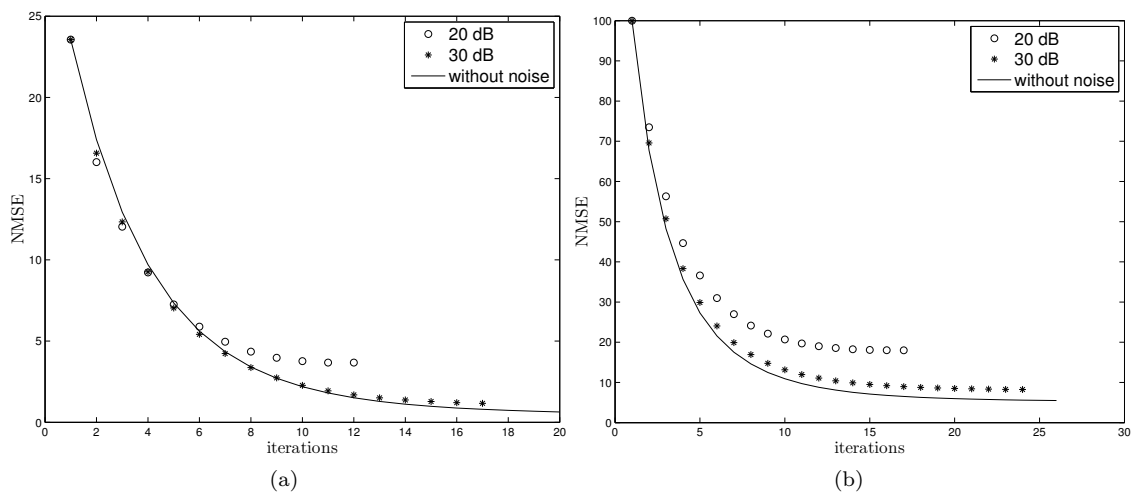


Figure III.12: NMSE (in %) in terms of iterations for the correction of the electron density (a) and of the activity map (b) for different SNR.

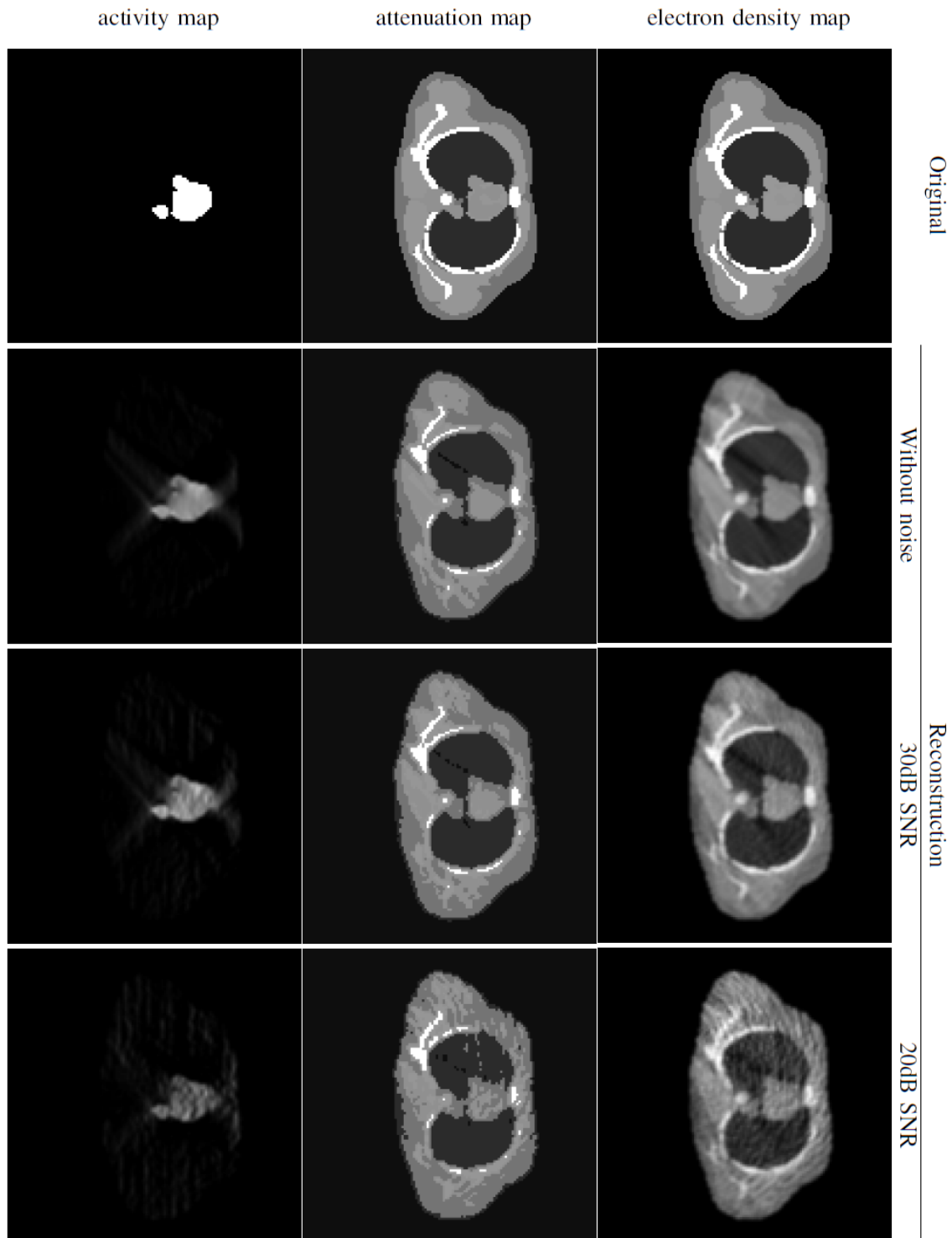


Figure III.13: Different reconstructions of the electron density map, attenuation map for different SNR. Reconstructions are obtained using the proposed correction algorithm and a Poisson noise correction process. We start these algorithms with data in Figs. III.10(a) and III.10(b).

III.4 Conclusion

The new CST approach proposes an alternative to current tomographic imaging techniques by keeping almost the same quality of reconstructions. In this paper, we have shown that a transmission Compton tomography modality can be combined with emission Compton tomography to form a new bimodal imaging system based on scattered radiation. The first CST modality characterizes the studied material directly by its electron density (scattering sites) and permits reconstructing an approximative attenuation map. In addition, the latter enables to reconstruct the activity map of the studied region of the human body. As such, the reconstruction of the electron density and of the attenuation map enables us to obtain a reasonable reconstruction of the activity through a suited correction algorithm. The latter is shown to be efficient for the correction of non-linear factors in the context of generalized Radon transforms, and as such, is particularly suited for the targeted application.

Both imaging modalities seem to be feasible and complementary as demonstrated by simulation studies and appear as an alternative to current tomographic imaging techniques by keeping a good quality of reconstructions without rotational motion around the studied object.

Conclusion and Perspectives

The aim of this thesis was to study the Radon transform defined over generalised curves. We investigated the modeling, the invertibility and the range condition. We derived then inversion formulae in order to study image formation and reconstruction in three modalities in Compton scattering tomography.

These contributions bring answers for some questions about the theory, modeling and algorithmic aspects.

- We have established the inversion formulae of Radon transforms defined on a Cormack-type family of curves, called here C_α , characterized by a non-linear-first-order differential equation. These inverse transforms are expressed in terms of circular harmonic components of data and original function
- Then we took an interest in the particular case C_1 for which we established
 - the singular value decomposition,
 - the Chebyshev/Zernike expansion,
 - the "filtered back-projection",
 - and a new stable form in the circular harmonic domain

Applications are numerous since this subclass leads to characterize a set of curves for which each associated Radon transform models a particular modality in Compton scattering tomography.

- In Chapter II, we made use of previous results shown in Chapter I to solve image formation and reconstruction problems for three modalities in CST associated to three Radon transforms, $CART_{1,2,3}$. Furthermore numerical approaches were required for the implementation of such transforms and so to prove the feasibility of such techniques. This survey permitted to compare different reconstruction method and to testify of the robustness of each methods by adding Poisson and Gaussian noise.
- In the first part of Chapter III we have proposed to generalize the concept of the IPC algorithm to a larger manifolds of transforms. In a general context, a correction taking account of the attenuation is required. We applied the proposed iterative algorithm, GIPC, to deal with the attenuation issue in modalities on CST studied in Chapter II.
- Finally we developed a new concept of bimodality imaging based on Compton scattering tomography modalities similar to the PET/CT system in a sense that it combines transmission and emission modalities. Both imaging modalities seem to be feasible and complementary as demonstrated by simulation studies and appear as an alternative to current tomographic imaging techniques by keeping a good quality of reconstructions without rotational motion around the studied object.

As interesting issues for further investigations, four lines of research emerge.

- **About the analysis :** it could be relevant to study the approximate inverse of the Radon transform defined on C_α . This kind of reconstruction way is based on the calculus of a reconstruction kernel associated to a mollifier through the inversion of the adjoint operator. However a better knowledge of the kernel is required. Such a technique could permit to perform reconstruction features.
- **About attenuation issue :** We have established a generalized algorithm to correct the attenuation factor, the GIPC, however establishing inversion formulae of the attenuated $CART_{1,2,3}$ could represent an even more powerful tool. One can be inspired by the work of Novikov in the attenuated Radon transform case, but the integral support to compute the attenuation factor involved by the geometry of scattering is very different from the classical circular support. Thus one must investigate on new properties of these attenuated circular-arc Radon transforms.
- **About advances in technology :** Our novel imaging system allows a two-dimensional image reconstruction from any scattered radiation collected by a one-dimensional collimated non-moving camera. This involves a new concept of detector with high energy resolution able to collect the scattered radiation.
- **From 2D to 3D :** A generalization in n-dimensional of the Radon transform over the corresponding n-dimensional curves of C_α could enable the development of a new concept of imaging system in 3D based on the scattered radiation.

Bibliography

- [1] M. L. Agranovsky and E. T. Quinto, *Injectivity sets for the Radon transform over circles and complete systems of radial functions*, J. Funct. Anal. **139** (1996), 383–413.
- [2] G. Ambartsoumian, R. Gouia-Zarrad, and M. A. Lewis, *Inversion of the circular Radon transform on an annulus*, Inverse Problems (2013).
- [3] H. H. Barrett and W. Swindell, *Radiological imaging: The theory of image formation, detection, and processing*, San-Diego Boston New-York, Academic press (1981), Appendix C.
- [4] S. Bellini, M. Piacentini, C. Cafforio, and F. Rocca, *Compensation of tissue absorption in emission tomography*, IEEE Trans Acoustics, Speech and Signal Processing **27(3)** (1979), 213–218.
- [5] T. Beyer et al., *A combined pet/ct scanner for clinical oncology*, J. Nucl. Med. **41** (2000), 1369–1379.
- [6] L. R. Bissonnette, *Imaging through fog and rain*, Optical Engineering **31** (1992), no. 5, 1045–1052.
- [7] L.-T. Chang, *A method for attenuation correction in radionuclide computed tomography*, IEEE Transactions on Nuclear Science **25** (1978), 638–643.
- [8] C. H. Chapman and P. W. Cary, *The circular harmonic Radon transform*, Inverse Problems **2** (1986), 23–49.
- [9] C.W. Clenshaw, *A note on the summation of chebyshev series*, Mathematical Tables and other Aids to Computatio **51** (1955), no. 9, 118–110.
- [10] A. H. Compton, *A quantum theory of the scattering of x-rays by light elements*, Phys. Rev. **21** (1923), no. 5.
- [11] A. M. Cormack, *Representation of a function by its line integrals with some radiological application*, J. Appl. Physics **34** (1963), 2722–2727.
- [12] ———, *The Radon transform on a family of curves in the plane*, Proceedings of the American Mathematical Society **83** (1981), no. 2, 325–330.
- [13] ———, *Radon's problem - old and new*, SIAM-AMS Proceedings **14** (1984), 33–39.
- [14] J. Darcourt, P.M. Koulibaly, and O. Migneco, *Méthodes itératives de reconstruction*, Revue de l'ACOMEN **4** (1998), no. 2, 100–107.
- [15] C. M. Davidson, *Alpha-, beta- and gamma-ray spectroscopy*, K. Siegbahn **1** (1968), 33–39.
- [16] D. Finch, S. K. Patch, and Rakesh, *Determining a function from its mean values over a family of spheres*, SIAM J. Math. Anal. **35** (2004), no. 5, 1213–10.
- [17] R. Gordon, *A tutorial on art (algebraic reconstruction techniques)*, IEEE Transactions on Nuclear Science (1974), NS-21:78–93.

-
- [18] P. Grangeat, *Analyse d'un système d'imagerie 3D par reconstruction à partir de radiographies X en géométrie conique*, Ph.D. thesis, École Nationale Supérieure des Télécommunications, 1987.
- [19] P.J. Green, *Bayesian reconstruction from emission tomography data using a modified em algorithm*, IEEE Transactions on Medical Imaging (1990), 9:84–93.
- [20] G. T. Gullberg, J. A. Malko, and R. L. Eisner, *Boundary determination methods for attenuation correction in SPECT*, Esser P, ed. Emission computed tomography **8** (1983), 33–45.
- [21] B. Hasegawa and H. Zaidi, *Dual-modality imaging: more than the sum of its components*, Quantitative analysis in nuclear medicine imaging, Springer (2006), 35–81.
- [22] S. Helgason, *The Radon transform on euclidean spaces, compact two-point homogeneous spaces and grassmann manifolds*, Acta Math. **113** (1965), 153–180.
- [23] ———, *The Radon Transform*, Second Edition, Birkhäuser, Boston (1999).
- [24] O. Klein and T. Nishina, *Über die streuung von strahlung durch freie elektronen nach der neuen relativistischen quantendynamik von dirac*, Z. F. Phys. **52** (1929), 11–12.
- [25] D.E. Kuhl and R.Q. Edwards, *Image separation raioisotope scanning*, Radiology **80** (1963), 653–62.
- [26] A. Kurusa, *The invertibility of the Radon transform on abstract totational manifold of real type*, Math. Scan. **70** (1992), 112–6.
- [27] ———, *Support curves of invertible Radon transforms*, Arch. Math. **61** (1993), 448–58.
- [28] K. Lange and R. Carson, *Em reconstruction algorithms for emission and transmission tomography*, Journal of Computer Assisted Tomography (1984), 8:306–316.
- [29] M. Ljungberg et al., *Attenuation correction in SPECT based on transmission studies and Monte-Carlo simulation build-up functions*, J. Nucl. Med. **31** (1990), 493–500.
- [30] A. K. Louis, *Ghosts in tomography - the null space of the Radon transform*, Mathematical Methods in the Applied Sciences **3** (1981), no. 1, 1–10.
- [31] ———, *Orthogonal function series expansions and the null space of the Radon transform*, SIAM J. Math. Anal. **15** (1984), no. 3, 621–633.
- [32] ———, *Approximate inverse for linear and some nonlinear problems*, Inverse Problems **12** (1996), 175–190.
- [33] ———, *Development of Algorithms in CT*, The Radon Transform and Applications to Inverse Problems (Providence, RI, USA) (Gestur Olafsson and Eric Todd Quinto, eds.), AMS Proceedings of Symposia in Applied Mathematics, American Mathematical Society (2006).
- [34] M. Dahlbom, D. C. Yu, S. R. Cherry, A. Chatziioannou, and E. J. Hoffman, *Methods for improving image quality in whole body PET scanning*, Nuclear Science Symposium and Medical Imaging Conference **3** (1991), 1587 – 1591.
- [35] P. Maass, *Singular value decompositions for the Radon transform*, Lecture Notes in Mathematics **1497** (1991), 6–14.
- [36] D. J. Macey, G. L. DeNardo, and S.J. DeNardo, *Comparison of three boundary detection methods for spect using compton scattered photons*, Journal of Nuclear Medicine (1988), no. 29, 203–207.
- [37] R.B. Marr, *On the reconstruction of a function on a circular domain from a sampling of its line integrals*, Journal of mathematical Analysis and Applications **45** (1974), 357–74.

-
- [38] A. Maze, J. L. Cloirec, R. Collorec, Y. Bizais, P. Briandet, and P. Bourguet, *Iterative reconstruction methods for nonuniform attenuation distribution in SPECT*, J Nucl Med **34** (1993), 1204–1209.
- [39] M.I. Miller, D.L. Snyder, and T.R. Miller, *Maximum-likelihood reconstruction for single photon emission computed tomography*, IEEE Transactions on Nuclear Science (1985), NS-32:69–778.
- [40] S. Moore et al., *Quantitative multi-detector emission computerized tomography using iterative attenuation compensation*, J. Nucl. Med. **23** (1989), 706–714.
- [41] T. Morozumi, M. Nakajima, K. Ogawa, and S. Yuta, *Attenuation correction methods using the information of attenuation distribution for single photon emission CT*, Med Imag Tech **2** (1984), 20–28.
- [42] M. Morvidone, M. K. Nguyen, T. T. Truong, and H. Zaidi, *On the V-line Radon transform and its imaging applications*, Journal of Biomedical Imaging: Special Issue on Mathematical methods for Images and Surfaces (2010), ID 208179, 6p.
- [43] K. Murase et al., *A comparative study of attenuation correction algorithms in single photon emission computed tomography (SPECT)*, European Journal of Nuclear Medicine **13** (1987), 55–62.
- [44] F. Natterer, *The mathematics of computerized tomography*, Classics in Mathematics, Society for Industrial and Applied Mathematics, New York (2001).
- [45] ———, *Inversion of the attenuated Radon transform*, Inverse Problems **17** (2002), 113–119.
- [46] F. Natterer and F. Wübbeling, *Mathematical Methods in image Reconstruction*, Monographs on Mathematical Modeling and Computation, Society for Industrial and Applied Mathematics, New York (2001).
- [47] M. K. Nguyen and T. T. Truong, *Inversion of a new circular-arc Radon transform for compton tomography*, Inverse Problems **26** (2010), no. 065005, (13pp).
- [48] M.K. Nguyen and T.T. Truong, *On an integral transform and its inverse in nuclear imaging*, Inverse Problems (2002), no. 8, 265–277.
- [49] S. J. Norton, *Compton scattering tomography*, Jour. Appl. Phys. **76** (1994), 2007–2015.
- [50] R. Novikov, *An inversion formula for the attenuated X-ray transformation*, Ark. Mat. **40** (2002), 14567.
- [51] J. Pergale et al., *Comparison between attenuation correction methods in transaxial single photon emission tomography*, Philips J. Res. **39** (1984), 24–50.
- [52] M.R. Perry, *On reconstructing a function on the exterior of a disk from its Radon transform*, Journal of mathematical Analysis and Applications **59** (1977), 324–41.
- [53] T. H. Prettyman, *Composition and density imaging of industrial samples by a combination of photon transmission tomography and projective compton scatterometry*, Ph.D. thesis, Dept. Nuclear Engineering, North Carolina State University, 1991.
- [54] E.T. Quinto, *Singular value decompositions and inversion methods for the exterior Radon transform and a spherical transform*, Journal of mathematical Analysis and Applications **95** (1983), 437–48.
- [55] J. Radon, *Über die Bestimmung von Funktionen durch ihre Integralwerte langs gewisser Mannigfaltigkeiten*, Ber.Verh.Sachs.Akad.Wiss.Leipzig-Math.Natur.Kl. **69** (1917), 262–277.

-
- [56] G. N. Ramachandran and A. V. Lakshminarayanan, *Three dimensional reconstruction from radiographs and electron micrographs: applications of convolutions instead of fourier transforms*, Proc. Natl. Acad. **68** (1971), 262–277.
- [57] N. J. Redding and G. N. Newsam, *Inverting the circular Radon transform*, DSTO Electronics and Surveillance Research Laboratory Report **DSTO-RR-0211** (2001), Edinburgh, Australia.
- [58] E. A. Ryan, M. J. Farquharson, and D. M. Flinton, *The use of compton scattering to differentiate between classifications of normal and diseased breast tissue*, Physics in Medicine and Biology (2005), no. 50, 3337–3348.
- [59] S. Surti, R. D. Badawi, C. H. Holdsworth, G. El Fakhri, P. E. Kinahan, and J. S. Karp, *A Multi-Scanner Evaluation of PET Image Quality Using Phantom Studies*, Nuclear Science Symposium Conference Record **4** (2003), 2425 – 2427.
- [60] L. Shepp and Y. Vardi, *Maximum likelihood reconstruction for emission tomography*, IEEE Transactions on Medical Imaging **1** (1982), 113–122.
- [61] M. Singh, *An electronically collimated gamma camera for single photon emission computed tomography - part 1: theoretical considerations and design criteria*, Medical Physics **10** (1983), no. 4, 421–427.
- [62] R. Sloboda, *Vector implementation of Chang’s attenuation correction method for single photon emission computed tomography*, Med. Phys. **14** (1987), 1045–1047.
- [63] J. A. Sorenson, *Quantitative measurement of radioactivity in vivo by whole-body counting*, Instrumentation in nuclear medicine **2** (1974), 311–348.
- [64] S. E. Sysoev, *Unique recovery of a function integrable in a strip from its integral over circles centered on a fixed line*, Communications of the Moscow Mathematical Societ (1997), 846–7.
- [65] M.M. Ter-Pogossian, M.E. Phelps, E.J. Hoffman, and N.A. Mullani, *A positron-emission transaxial tomograph for nuclear imaging (pett)*, Radiology **114** (1975), no. 1, 89–98.
- [66] O. Tretiak and C. Metz, *The exponential Radon transform*, SIAM J. Appl. Math. **39** (2002), no. 2, 341–354.
- [67] L. Triet, R. Chartrand, and T. J. Asaki, *A Variational Approach to Reconstructing Images Corrupted by Poisson Noise*, J Math Imaging Vis (2007), doi: 10.1007/s10851–007–0652–y.
- [68] T. T. Truong and M. K. Nguyen, *On new v-line Radon transforms in \mathbb{R}^2 and their inversion*, J. Phys. A: Math. Theor. **44** (2011), no. 075206, 13pp.
- [69] ———, *Radon transforms on generalized cormack’s curves and a new compton scatter tomography modality*, Inverse Problems (2012).
- [70] B. M. W. Tsui, X. Zhao, E. C. Frey, and W. H. McCartney, *Quantitative SPECT: basics and clinical considerations*, Seminar in nuclear medicine **XXIV(1)** (1994), 38–65.
- [71] J. W. Wallis, T. R. Miller, and P. Koppel, *Attenuation correction in cardiac SPECT without a transmission measurement*, Journal of Nuclear Medicin (1995), no. 36, 506–512.
- [72] T. E. Walters, W. Simon, D. A. Chesler, and J. A. Correia, *Attenuation correction in gamma emission computed tomography*, Comput Assist Tomogr **5** (1981), 89–94.
- [73] R. Ben Younes, J. Mas, and R. Bidet, *A fully automated contour detection algorithm the preliminary step for scatter and attenuation compensation in spect*, European Journal of Nuclear Medicine and Molecular Imaging **14** (1988), 586–589.

-
- [74] H. Zaidi, *Relevance of accurate Monte Carlo modeling in nuclear medical imaging*, Med. Phys. **26(4)** (1999), 574–608.
- [75] H. Zaidi, M.-L. Montandon, and D. O. Slosman, *Magnetic resonance imaging-guided attenuation and scatter corrections in three-dimensional brain positron emission tomography*, Med. Phys. **30** (2003), 937–948.
- [76] ———, *Attenuation compensation in cerebral 3D PET effect of the attenuation map on absolute and relative quantitation*, Eur J Nucl Med Mol Imaging **31** (2004), 52–63.
- [77] I. G. Zubal, C. R. Harrell, E. O. Smith, and A. L. Smith, *Two dedicated software, voxel-based, anthropomorphic (torso and head) phantoms*, Proceedings of the International Workshop, National Radiological Protection Board (Chilton, UK), July 1995.